UNIVERSITA' DEGLI STUDI DI PADOVA

Sede Amministrativa: Università degli Studi di Padova

Dipartimento di Scienze Chimiche

DOTTORATO DI RICERCA IN : Scienza dei Materiali

CICLO XIX

Carbon nanotubes grown by chemical vapour deposition: a catalyst activation study

Coordinatore : Ch.mo Prof. Gaetano Granozzi

Supervisore : Ch.mo Prof. Gaetano Granozzi
Correlatore : Dott. Cinzia Cepek

Dottoranda : Cecilia Mattevi

DATA CONSEGNA TESI
31 gennaio 2008

Abstract

Nowadays the main challenge to fully exploit carbon nanotubes (CNTs) for potential applications consists of achieving complete control over their synthesis.

Synthesis control means to be able to selectively obtain isolated CNTs as well as bundles, different types of CNTs (SWNT/MWNT/CNF), different chiralities and diameters, their location and orientation. Other aims are decreasing defect and impurity concentrations, and increasing yields.

These goals can be reached only by a complete understanding of the role of the catalyst during its interaction with the environment (substrate and feed stock).

In this thesis, we have investigated the effects of the substrate-catalyst interaction on the growth and the chemical decomposition of the carbon precursor gas on the catalyst clusters and the consequent formation of carbon structures during the growth process itself.

We have mainly concentrated on studying the growth by surface bound chemical vapour deposition method using Fe and/or Ni as catalysts, Al_2O_3 and SiO_2 as the support substrate, and C_2H_2 as the precursor gas. We have identified how different catalyst-substrate interactions between Fe-Al_2O_3 and Fe-SiO_2, determine the difference in density, direction and type of carbon nanotubes obtained by using the same pretreatment and growth conditions. Different experimental conditions and apparatus were employed to study the catalyst-substrate interactions effects. We monitored the chemical state of the catalyst and the substrate *in situ* by X-ray photoemission spectroscopy and, in parallel, the morphology of the surface at each intermediate state of the catalyst preparation (by *ex situ* atomic force microscopy (AFM)). Further we confirmed the results by post-growth characterization by transmission electron microscope (TEM).

Studying the catalyst-hydrocarbon interaction *in situ* via both environmental TEM (ETEM) and XPS techniques has allowed us to make progress towards an atomistic model of CNT growth. By *in situ* time-resolved ETEM we have found that structural selectivity is determined by the dynamic interplay between carbon network formation and catalyst crystalline particle deformation. Our *in situ* time-resolved XPS study shows the selective acetylene chemisorption on metallic Fe catalyst, which is rapidly followed by the formation of a carbon-rich phase (iron carbide), to finally the formation of a sp^2 carbon network

characteristic of graphite. Carbidic carbon has also been detected, even if gradually attenuated from the graphitic peak, up to the intensity saturation of the sp^2 C peak.

Summarizing, we have observed selective acetylene chemisorption at the nucleation stage and we have demonstrated that the formation of a carbon-rich (sub)surface layer on crystalline transition metal nanoparticles is an integral part of catalyst dynamics during CNT growth.

Sommario

Oggi la principale sfida per arrivare all' applicazione dei nanotubi di carbonio (CNT)e così sfruttarne le proprietà, consiste nel raggiungimento del pieno controllo della loro crescita. Questo significherebbe essere in grado di crescere in modo selettivo CNT isolati oppure sotto forma di bundels, diversi tipi di nanotubi (se a parete singola,o con più pareti o fibre),di poter controllare la loro posizione e orientazione e le chiralità e diametro. Inoltre si dovrebbe essere in grado di diminuire la concentrazione di difetti e impurezze ed aumentare la resa di crescita.

In questo lavoro di tesi è stata studiata l'interazione tra il catalizzatore e il substrato ai fini di comprenderne le conseguenze sulla crescita dei CNT. In secondo luogo è stata studiata la decomposizione chimica gas precursore per la crescita dei nanotubi con il catalizzatore durante lo stesso processo di crescita, e la successiva formazione di strutture di carbonio.

Noi ci siamo concentrati principalmente sulla crescita via surface-bound chemical vapor deposition, usando come catalizzatori il Fe e il Ni, come substrati Al_2O_3 e SiO_2 , e come gas precursore C_2H_2 . Abbiamo individuato come una diversa interazione catalizzatore – substrato nei casi Fe-Al_2O_3 and Fe-SiO_2 possa determinare la crescita di nanotubi diversamente orientati, di diverso tipo e in diversa densità , a parità di condizioni di pretrattamento e crescita dei nanotubi. Abbiamo utilizzato diverse condizioni sperimentali e diversi apparati per studiare gli effetti sulla crescita di questa interazione. Abbiamo monitorato lo stato chimico del catalizzatore e del substrato *in situ* dopo ogni step del processo CVD via X-Ray Photoemission Spectroscopy (XPS) e la morofologia *ex situ* via Atomic Force Microscopy (AFM). I risultati ottenuti sono stati confermati da misure mediante Transmission Electron Microscope (TEM) effettuate alla fine della crescita.

In secondo luogo abbiamo contribuito alla costruzione di un modello atomistico sulla crescita dei nanotubi, studiando *in situ* in tempo reale l'interazione catalizzatore-precursore mediante Environmental TEM (ETEM) and XPS.

Dalle misure ETEM effettuate *in situ* durante la crescita, abbiamo visto che la conformazione finale della struttura di carbonio si va generando attraverso una continua

dinamica di cambiamento di forma sia degli strati di carbonio esagonale legati alle particelle di catalizzatore cristalline che della particelle stessa .

Le misure *in situ* XPS risolte in tempo, mostrano che inizialmente il precursore interagisce con il catalizzatore generando un chemisorbimento del carbonio sulla particella metallica, successivamente, contemporaneamente alla scomparsa del carbonio chemisorbito, avviene la formazione di un carburo di ferro.Questo persiste per pochi secondi, per poi far seguire la crescita del carbonio sp^2 tipico del legame grafitico. Il segnale del carbonio legato al ferro persiste, anche se attenuato, fino alla fine del processo di crescita.

Riassumendo, abbiamo osservato la formazione del carbonio chemisorbito come fase iniziale di interazione precursore-catallizatore e successivamente la formazione di strati di carbonio grafitico superficiali e/o sotto superficiali alla nanoparticella cristallina di catalizzatore, che portano ad una interazione dinamica attraverso la quale si sviluppa il nanotubo.

.. e osservar gli effetti della natura che, quantunque appariscano minimi e di nessun conto, non devono mai dal filosofo disprezzarsi, ché le operazioni di natura son tutte in pari grado degne di maraviglia; e perché anco da cose comuni, direi in certo modo vili, si posson trarre notizie molto curiose e nuove, e bene spesso remote da ogni immaginazione.

***

Galileo

Acknowledgements

I would like to thank my supervisor, Prof Gaetano Granozzi, for the opportunity he has given me to work on this subject. A special gratitude goes to Dott. Cinzia Cepek , for sharing her wide scientific knowledge with me .

My gratitude goes also to people from "Microstrutture e Nanostrutture di carbonio" Lab & Badelph beamline: Andrea Goldoni, Carla C.Cudia, Sheema Dolafi , Paolo Vilmercati for their support and all the useful discussions had during these years. Special thanks also Stephan Hofmann, who contributed to introduce me bit by bit to the magic world of nanotubes. Extreme gratitude goes to all people in TASC who shared useful discussions during these years.

Thanks to my family for the continuous support throughout these years, and for having always been a reference point whenever I needed.

I would like to thank all my friends, here and everywhere in the world, for having been sharing with me hours unforgettable. A special thanks for the nearest-neighbours lab friends: Yenny, Mattia, Adriano, Simone, , Fauzia, Sasha.

Thanks to Rajesh B. S. for having been close to me in the bad and good time and for having let me know the meaning of "The Truth Always Wins".

TABLE OF CONTENTS

List of Abbreviations

AFM	**Atomic Force Microscope**
CMOS	**Complementary Metal Oxide Semiconductor**
CNF	**Carbon Nanofibers**
CNT	**Carbon Nanotubes**
CVD	**Chemical Vapour Deposition**
ETEM	**Environmental transmission Electron Microscopy**
FET	**Field Effect Transistor**
HiPCO	**High Pressure CO (disproportionation)**
HOPG	**Highly Oriented Pyrolitic Graphite**
HRTEM	**High Resolution Transmission Electron Microscopy**
MWNT	**Multi Wall Carbon Nanotubes**
NPs	**Nanoparticles**
PMMA	**Polimetilmetacrilate**
TEM	**Transmission Electron Microscopy**
SEM	**Scanning Electron Microscopy**
SWNT	**Single Wall Carbon Nanotubes**
STM	**Scanning Tunnelling Microscopy**
XPS	**X-Ray Photoemission Spectroscopy**

Introduction and thesis structure

All the grow techniques for CNTs can be categorized in three different groups: laser ablation, arc discharge, and chemical vapour deposition (CVD). Among them, CVD is more appealing because it allows controlled, selective growth of CNTs directly on a patterned substrate as well as bulk production. This is because the low temperatures involved permit direct deposition onto a electronic device [1,2]. Moreover CVD, needing lower temperature and pressure that the other techniques, enables direct, real-time observation of the catalytic nucleation process at the atomic scale, helping to understand the mechanisms governing the CNT formation.

The CVD process, which will be widely used in this thesis, briefly consist of: deposition and eventually pretreatment of a catalyst (typically a transition metal) on an appropriate substrate, heating of the system to the growing temperature, and finally the exposure to a mixture of gases, including, in most cases, a hydrocarbon. The resulting carbon structure depends strongly on all the above parameters. Generally, high temperatures (>700ºC) are needed for SWNT nucleation, whereby the metal catalyst is assumed to liquefy and supersaturate the growing carbon structure [3-5]. This was the commonly accepted growth theory [3-5] based on a vapour-liquid-solid model [6].

On the contrary, by using the appropriate CVD growth conditions, SWNT nucleation at temperatures as low as 350°C [7] has been recently observed. This low temperature synthesis challenges the commonly accepted growth model [3-5]. Based on *ab-initio* calculations, Hofmann et al. [8] suggested that surface effects, rather than bulk catalyst effects, dominate CNT growth kinetics. Other recent experimental [9] and theoretical [10] data support this model, however, more detailed experimental data describing catalyst-substrate interactions [11] and catalyst-hydrocarbon interactions, are required to deeply understand the CNT growth.

So far little attention has been paid to the influence of the substrate on the CNT growth via CVD and thus to the substrate-catalyst interaction. Actually the key role of the substrate has became evident just a short time ago, when a forest of vertically aligned SWNTs 2 mm long, with a growth rate of a few micrometers per second has been obtained. The resulting SWNTs had a high degree of purity, without amorphous carbon, CNFs and MWNTs [12,13]. This was obtained by employing etching compounds for amorphous carbon (like adding water) on Fe/Al_2O_3 and Fe/Al_2Ox substrates. Only a low density of horizontal SWNTs has been grown on Fe/SiO_2 by employing the same growth conditions. These results demonstrate the essential role of the Al_2O_3 and Al_2Ox support as an enhancer of the nanotube growth rate, however so far it is not clear how it can favour the growth.

Here we briefly present the question to which this thesis aims to answer . The first point we study is : why are the growth results different on Fe/Al_2O_x and on Fe/SiO_2 systems when using the same pretreatment and growth conditions? The second point we address is the interaction mechanism between the catalyst and the precursor gas during the CVD growth. So far, the growth process has been empirically optimized because the catalyst interaction with the carbon precursors is not yet completely understood. Consequently the other issues we investigate are: Is the interaction between the catalyst nanoparticles and the carbon atoms mainly a surface or a bulk phenomenon? Which are the intermediate chemical states that the carbon atoms have to pass from the precursor to the sp^2 graphitic form?

To achieve these goals, we have developed several CVD processes in different experimental apparatus, spanning a variety of growth parameters. The growths have been done in conventional CVD reactors, and in different ultra high vacuum (UHV) apparatus (base pressure: $<1x10^{-10}$mbar). In the latter case it is possible to control the chemical state of the catalyst (before, after and during the growth) and to monitor precisely all the CVD parameters, such as: precursor gas purity, pressure and its gradient, sample temperature, gas fluxes, etc. Moreover all the steps of the CVD process and of the catalyst film preparation have been done in sequence, without any contamination due to air exposure. We have used unconventional, very low precursor pressures (up to $2x10^{-7}$ mbar), which enable us to follow *in situ* the evolution of the carbon chemical state via time-resolved X-ray photoemission spectroscopy (XPS). In addition, we have followed the crystallinity and dynamical shape of the catalyst nanoparticles during the CNT nucleation-growth via *real-time* environmental transmission electron microscopy (ETEM) measurements**.**

The layout of the present thesis implies the following chapters. At the beginning of each chapter short summary about the contents of each section is reported.

Chapter 1 collocates the CNT in the context of the technology nowadays. It is illustrated the structure of the CNT and their properties with the related possible, or under investigation, application.

Chapter 2 is an overview of the current CNT growth techniques. The advantages of surface-bound CVD (the growth technique adopted in this work) in terms of control of CNT growth are pointed out.

Chapter 3 presents at the beginning a short overview of the early CNT growth model reported in the literature and then the effects of the CVD conditions on the CNT growth . The final discussion is dedicated to the presentation of the current debated models of the CNT nucleation and growth mechanism.

Chapter 4 illustrates the different morphologies of Fe thin layers, as deposited and after thermal treatments, generated on different substrates (SiO_2, Al_2O_3, graphite HOPG).The different Fe layer morphologies have been connected to different chemical interaction, found by XPS characterizations, of Fe with the topmost layer of these substrates.

Chapter 5 shows the growth results on SiO_2 and on Al_2O_3 and the explanation of the different substrate effects on CNT growth in terms of different substrate-catalyst interactions.

Chapter 6 is dedicated to the presentation of the results of the real time ETEM and XPS measurements collected during CNT growth, and to the interpretation of these results obtained by these techniques. Finally relevance of these results in context with current debate concerning the CNT nucleation and growth mechanism is discussed.

Chapter 7 presents the summary and the conclusion of this work and it hints the future projects to continue on these research subjects.

Appendix A presents all the experiment procedures adopted and the description of all the experimental apparatus used.

Bibliography

[1] Dai H., *Acc. Chem. Res*. 35, 1035 (2002).

[2] Vajtai R., Wei B. Q., and Ajayan P. M., *Philos. Trans. R. Soc. London A* 362, 2143, (2004).

[3] Baker R.T.K.,. Barber M.A, Harris P.S., Feates F.S., Waite R.J., *J.Catal.* 26, 51 (1972).

[4] Kanzow H., Ding A., *Phys. Rev. B* 60, 11180 (1999).

[5] Gavillet J., Loiseau A., Journet C., Willaime F., Ducastelle F., Charlier J.C., *Phys. Rev. Lett.* 87, 275504, (2001).

[6]Wagner R.S, Ellis W.C., *Appl. Phys. Lett* 4, 89 (1964).

[7] Cantoro M., Hofmann S., Pisana S., Scardaci V., Parvez A., Ducati C., Ferrari A. C., Blackburn A. M., Wang K. Y., and Robertson J., *Nano Lett*. 6, 1107 (2006).

[8] Hofmann S., Csányi G., Ferrari A. C., Payne M. C., Robertson J., *Phys. Rev. Lett*. 95, 36101 (2005).

[9] Sharma R., Rez P., Treacy M. M. J., Stuart S. J., *J. Elec. Micros*. 54, 231 (2005**).**

[10] Raty J.Y., Gygi F., Galli G., *Phys. Rev. Lett.* 95, 96103 (2005).

[11] de los Arcos T., Garnier M. G., Seo J. W., Oelhafen P., Thommen V., Mathys D., *J. Phys. Chem. B* 108, 7728 (2004).

[12] Hata K., Futaba D. N., Mizuno K., Namai T., Yumura M., and Iijima S., *Science* 306,1362 (2004).

[13] Noda S., Hasegawa K., Sugime H., Kakhei K., Zhang Z., Maruyama S., and Yamaguchi Y., *Jpn. J. Appl. Phys*. 46, 399 (2007).

Chapter 1

CNT: structure and properties

Writing in English is the most ingenious torture ever devised for sins committed in previous lives.

James Joyce

In this chapter we present at the beginning the nanotechonological importance of the carbon nanotubes (section 1.1). In the section 1.2 we illustrate the carbon nanotube structures and then we dedicate all the section 1.3 to the description of their properties.

1.1 Nanotechnology and carbon nanotubes.

The first discussion about the possibility to develop the technology at nanoscale have been suggested by R. Feynmann [1]. In a visionary talk, titled "There is plenty of room at the bottom", he told: "The principles of physics, as far as I can see, do not speak against the possibility of maneuvering things atom by atom". This can be considered as the basis of the definition of nanotechnology, which is coming into reality, when materials and tools necessary for mankind will be built atom-by-atom and molecule-by-molecule.

Some decades ago, G. Moore, one of the founders of Intel Company, realized that the capacity of memory chips can be extended mainly by decreasing the feature sizes of conventional Si-based field-effect transistor (FET) integrated circuits to ever-smaller, according to a firm tendency [2] denoted as Moore's law, shown in Figure 1.1. This figure 1.1 shows how the feature size changed in the last decades, in logarithmic scale and how the size will change in the future 10 years . The feature size is presently 65 nm and the gate length of FETs at this node is 32 nm, which is well within the 'nano' range, and the future size of 10 nm should be achieved about 2015-2019 [3].

Previously mentioned Moore's law is based on the concept that, the main innovation lies in continuous device miniaturization, without the need to alter the basic production cycle. Naturally, such a development has its limits: physical, when tunneling through the ever-thinner gate insulator becomes significant and the layers begin to conduct, or economical, when the lithography costs exceed the improvement rate of the other processes. Therefore, the microelectronics industry must prepare alternatives for this eventuality, that allows the rate of productivity increase to be maintained. This can be achieved through the inclusion of new materials into the current successful production process flow . However since the transistor scaling will reach its limit, as Moore's law predicts the end will be approximately 2020; the things must change if we want to continue the Moore's law. Therefore it will be necessary to lead a new trend without transistors. This trend might be given by self assembling of new type of molecular electronics on a complementary Metal Oxide Semiconductor(CMOS) platform [4,5].

A short term scaling approach maintains the field effect transistor principle as well as the general current circuit architecture, but replaces the Si channel of the FET by one – dimensional nanostructure with superior electrical transport properties. In addition to the efforts to develop new electronic devices, direct band gap one-dimensional nanostructures are attracting attention because of the desire to base both electronic and optoelectronic technologies, on the same material. Among the different one dimensional material, SWNTs have many highly deliverable and distinctive device properties. Semiconducting SWNTs are required for transistor applications, whereas MWNT can be used for conducting connectors.

The first CNT transistor was fabricated back in 1998[6]. The CNT FETs are particularly interesting because they might provide much better on/off current and device speed [7][8]. In the current road map for semiconductor devices, CNT (and nanowires) based Field Effect Transistors (FETs) are expected to be of relevance in about five years (from 2012 onwards).

Hence, the actual challenge consists in reaching complete control in their synthesis to selectively obtain isolated CNT as well as bundles, to control their location and orientation, and to synthesize complex and organized networks of arrays of CNT directly on large substrates suitable for applications. Moreover, progress in the synthesis process is required to narrow the diameter and chirality range of the CNT, to decrease defects and impurities and to increase their production yield. This is a general task of nanoscience, i.e. to increase our ability to synthesize, organize and tailor-make materials at the nanometer scale. Further goals are to arrange the single nanostructures (building blocks) in assemblies with the desired properties (including biologically-inspired systems), to explore and establish novel architectures to connect nanoscience to molecular electronics and biology, and to improve our tools for the characterization of nanostructures.

Many relevant innovative properties critically depending on their structure (see section 1.2), are presented by CNT (see section 1.3) and for these properties they are in the focus of multi-disciplinary studies for a wide range of applications [9].

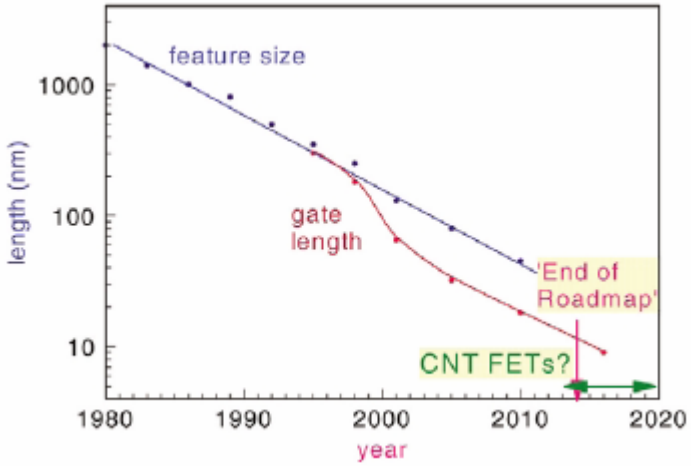

Figure 1.1 *Moore 's law shows the feature size of the integrated circuits vs. years [2,3]. It is predicted that around 2012 CNT-FETs might become relevance as they fulfill the technological requirements. It is reported also the gate length trend, which is the distance in the near-surface region of Si substrate between edges of the drain and source regions in the FETs.*

1.2 Carbon nanotube structure

From the perspective of the humankind, carbon is the most important element of the Periodic Table and its great ability to form bonds with other elements is at the basis of the organic and biochemistry.

From an inorganic perspective, solid state carbon is known from ancient times in two allotropic forms: diamond and graphite (Figure 1.2). In the last part of the past century, several other nano-allotropes of carbon have been discovered (see Figure 1.3).

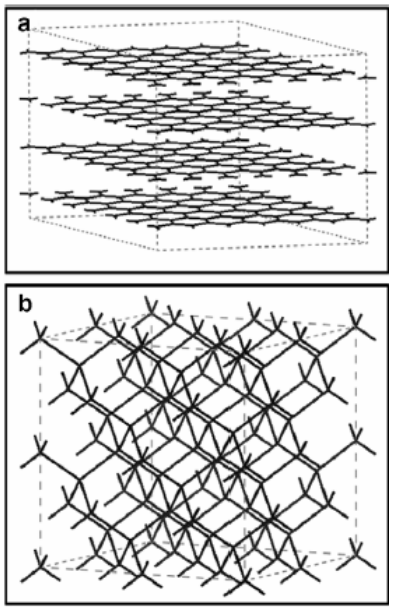

Figure 1.2 *The two allotropes of bulk carbon: a) graphite, b) diamond.*

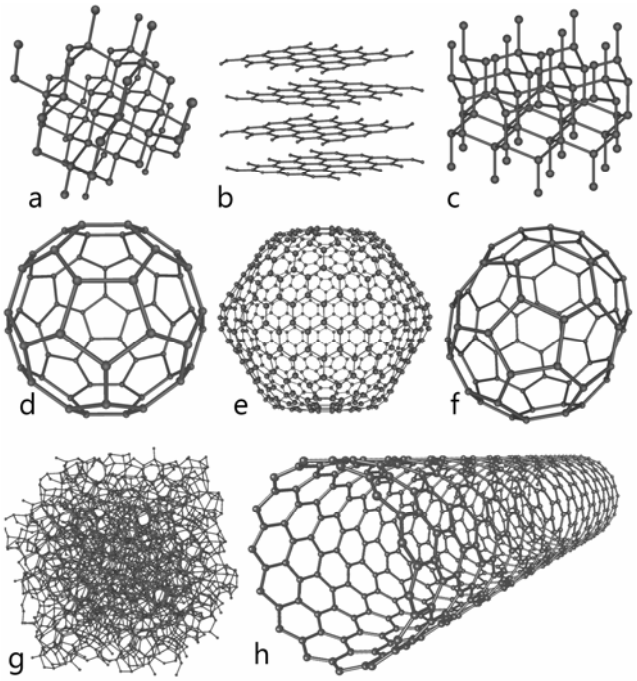

Figure 1.3 *The nanoworld of carbon: a) Diamond, b) Graphite, c) Lonsdaleite, d) C_{60} (Buckminsterfullerene or buckyball), e) C_{540}, f) C_{70}, g) Amorphous carbon, and h) single-walled carbon nanotube.*

A convenient way to classify the C allotropes is in terms of their dimensionality: diamond and graphite form 3D macroscopic structures, a single sheet of graphite (called graphene) form a 2D nanostructure, CNTs are examples of 1D nanostructures, while fullerene and all their parents (e.g. onions, et cet) are finally 0D nanosystems. The three nano-allotropes which are object of high interest in the nanotechnology world are (in order of discovery time): graphene, obtained about 30 years ago [10][11], but only very recently (since 2004) it started to attract the attention, C_{60} (buckminster-fullerene), found by Kroto et al. [12] in 1985, and CNTs, discovered by Ijima et al[13] in 1991.

Another way to classify the carbon allotropes is in terms of their prevalent 2sp orbital hybridization. Carbon possesses four electrons in its outer valence shell; the ground state configuration is $2s^2 2p^2$, and it forms covalent bonds with the other C atoms. In diamond, carbon atoms exhibit sp^3 hybridization, where four bonds are directed towards the corners of a regular tetrahedron. The resulting 3-D network is extremely rigid and stable. The bond length between sp^3 carbon atoms in diamond is 1.56 Å. For graphite, sp^2 hybridization is present, with three carbon bonds, distributed in the xy-plane (120°), and the fourth σ bond is a weak π-bond perpendicular to the plane. The C-C σ sp^2 bond length is 1.42 Å. A graphene sheet

consists of sp^2 hybridized carbon σ atoms forming a hexagonal (honeycomb) lattice. The π bond between graphene layers is weak and the consequent spacing, in graphite, is 3.35 Å.

The cage-like carbon molecules are generally known as fullerenes. The most popular one is C_{60} where the 60 carbon atoms are arranged as a truncated icosahedron. In C_{60} the structure is curved by the introduction of pentagonal rings and consequently the sp^2 carbon hybridization gains some sp^3 character. The number of pentagons present in a fullerene, is fixed by a strict mathematical rule: as Eulero demonstrated in his theorem, a polyhedron with n-vertex and composed only by hexagons and pentagons there are 12 pentagons and [(n/2)-10] hexagons. The existence of pentagons allows to form a closed molecule but at the same time they induce a local tension since the sp^2 hybridization would drive to a planar structure. As a consequence, only selected isomers have been isolated, where the number of pentagons minimizes the tension associated with the bend, e.g. C_{60} and C_{70}.

Passing now to the CNT, we can distinguish between single wall carbon nanotubes (SWNTs) and multi wall NT (MWNT). A MWNT consists of concentric different size SWNTs bonded by Van der Waals interactions and it stay to the SWNT as the onion stay to the single cage-like fullerene (see Figure 1.3). Theoretically, it is possible to obtain a SWNT by rolling up a graphene sheet. There are several ways [9] to roll up the single graphene sheet: the resulting conformations, where the C-C bonds lie at an angle to the tube axis, are known as different helical structures (Figure 1.4). Only two ways to roll up are "non-chiral", so that the honeycomb lattices located at the top and bottom of the tube are always parallel each other. These configurations are known as "armchair" and "zigzag". In the armchair structure, two C—C bonds on opposite sides of each hexagon are perpendicular to the tube axis, whereas, in the zigzag arrangement, these bonds are parallel to the tube axis (figure 1.4). The tube chirality is defined in terms of a chiral vector $\mathbf{C_n} = n\mathbf{a_1} + m\mathbf{a_2}$ here a_1 and a_2 are the unit vectors of the graphene lattice, which can determine the tube diameter d (Figure 1.4). This vector determines the direction of rolling a graphene sheet, in which a lattice point (m, n) is superimposed with an origin defined as (0, 0) (figure 1.4). Thus, the diameter can be expressed as $d=(a/\pi)(m^2+mn+n^2)^{1/2}$ where $a = 1.42\sqrt{3}$ Å corresponds to the lattice constant in the graphene sheet. Note that the C—C distance is 1.42 Å. The chiral angle (angle between $\mathbf{C_n}$ and the zigzag direction) is defined as $\Theta=\arctan(-\sqrt{3}a/(2m+n))$.

For zigzag tubes, $\Theta = 0$ and $(m; n) = (p; 0)$, ($p \in N$) conditions have to be fulfilled for the chiral angle Θ and the tube chirality $(m; n)$, while $\Theta = \pm 30°$ and $(m; n) = (2p;-p)$ or $(m; n) = (p; p)$, ($p \in N$) hold for armchair tubes.

Theoretical calculations indicate that all armchair SWNT are metallic, as well as zigzag SWNT exhibiting values of m - n multiple of 3. The metallic conductivity condition can be written as 2m + n = 3k (k ЄN), whereas in all other cases where 2m + n is different from 3k (k Є N), SWNT show semiconducting properties. Thus, for a uniform distribution of n,m values, there is a one-over-three chance of a SWNT being a metal, and a two-over-three chances of being a semiconductor.

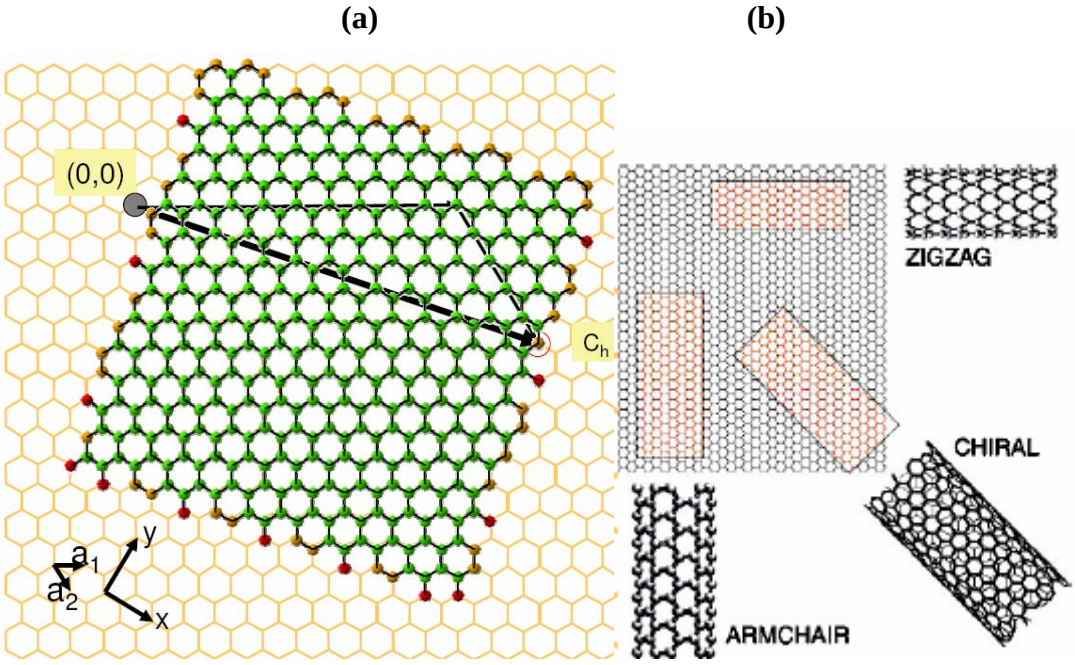

Figure 1.4 *(a) This vector convention is used to define each point on lattice since there are several ways to roll a graphene sheet over. Unitary vectors a_1 and a_2 are necessary to determine rolling direction expressed by vector C_n.*
(b) : From the rolling of a graphene sheet can be generated three possible nanotube structures: zigzag, armchair and chiral [9]. All armchair tubes are metallic, whereas the zig zag can be either semiconducting or metallic.

Hence the electronic properties of nanotubes are due to the quantum confinement of electrons normal to the nanotube axis. In the radial direction, electrons are confined by the monolayer thickness of the graphene sheet. Because of the quantum confinement, electrons can propagate only along the nanotube axis, and so their wave vectors point in this direction. From probability considerations, MWNTs will be metallic, except if they have very few walls. The interlayer spacings between the different walls is 3.4 Å, a value that is slightly greater

than that of graphite (3.35 Å). Iijima et al.[13] attributed this difference to a combination of the tubule curvature and van der Waals interactions between the successive cylinders.

Finally, the distinction between CNT and carbon nanofibers (CNF) is not clearly drawn in literature. The term CNF is often used for tubular structures with walls not parallel to the tube axis and lower degree of crystallinity, or also exhibiting bamboo-like intersects.

1.3 Carbon nanotube properties and applications

In this section we present the main properties of carbon nanotubes and their applications. As it will be explained, some of these properties, and consequently the applications, have not fulfilled the expectations, while others are still object of intensive exploration. The main reasons of the delay with respect to the road map are to be searched in the scarce stock of CNTs in the market. This, in turn, is related to the scarce level of control in the CNT growth.

1.3.1 Electronic properties

During the last few years, physicists have been attracted by the extraordinary electronic properties of CNTs. Let us start from the band structure of a graphene sheet: the valence and conduction bands meet precisely at the Fermi energy at the edge of the Brillouin zone [14]. When a graphene sheet rolls up into a SWNT, confinement of electrons around the circumference is observed. The unique electrical properties of SWNT arise from such confinement of the electrons, which can move in a several micrometer scale only along two directions [14,15] at room temperature. Here the transport is ballistic hence the terminal conductance (G) of a one dimensional system is given by Landauer equation 1.1 [14].

$$G = \frac{2e^2}{h}\sum_{1}^{n} T_i \qquad 1.1$$

where $2e^2/h$ is the quantum of conductance and T_i is the transmission coefficient of each contributing subband (conduction channel) produced by the confinement of electrons

along the circumference of the CNT. In absence of the electron scattering, the resistance of metallic SWNT was calculated to be 6.5 kΩ using equation 1.1. The resistance is due to the quantum mechanical coupling of the two conducting subbands in the nanotubes with the connecting leads. This is unavoidable, and every interconnect made with perfect CNT would have at least similar resistance [16]. It has been shown [16] that the major contribution in conductance of carbon nanostructure comes from the π electrons and only a very small part from the σ electrons. The contribution of σ and the coupling of σ - π electrons were found to be significant only in the case of bent CNT [17].

The electronic transport properties of CNT can change depending on: the degree of graphitization, chirality, diameter, the microstructure of the tube, extent of functionalization [18] and doping [19,20]. The remarkable peculiarity of CNT [21,22] is the possibility of band gap engineering by control of their microstructure. As mentioned before, a nanotube is metallic at room temperature if (n- m) = 3i is an integer. Otherwise, it is semiconductor with band gap Eg ≈(0.9/d) eV, where d is the diameter of the CNT in nm. It is worth mentioning that the band gap of semiconducting CNT is inversely proportional to the tube diameter. The diameter of a CNT can be expressed as $d=(a/\pi)(m^2+mn+n^2)^{1/2}$ where a is the C—C bond length.

An introduction of small defect, like single carbon vacancy, could affect the conductivity [16] and band gap modulation of semiconducting CNT [23] . It has been proposed that the response of the p_z-orbital state (mostly due to the carbon atoms nearest to the vacancy site) towards the different applied directions of an external field was the main reason for the difference of the band gap variations in CNT with vacancy defects [23]. With large electric fields, the band gap in defective CNT becomes similar to the perfect one. In addition, since in general the CNT band gap is dependent on the direction and the strength of the transverse electric field, the resulting tunability can provide a suitable band gap for a specific application.

1.3.1.1 Microelectronic applications

Two main applications, exploiting the electron transfer properties of CNT, have been so far proposed in integrated circuits: either as interconnects between transistors, or as channel in field effect transistor (FET) [4][14][15]. Other applications are for the micro electromechanical systems (MEMS)-type memory devices [25], for displays in vacuum microelectronics [3,24] and as sensors [26] (this point will be further discussed later).

In this section we will only briefly report on the FET applications. In an integrated circuit each FET is connected by interconnects. As the dimensions decrease, the current density carried by each interconnect increases, so it is necessary to have a suitable material capable to sustain the needed current for area unit. For the normal metals, the maximum current density they can sustain is limited by electro-migration which is a sort of self-electrolysis of the metal atoms, which leads to failure of metals at their grain boundaries. Recently the Al interconnects have been replaced by Cu which has a maximum current capacity of the order of 10^6 A/cm^2. CNT can carry a current density higher than Cu, of the order of 10^9A/cm^2. This arises from the nature of the bonds between carbon atoms, covalent bonds which are stronger and more directional than metal bonds. This allows a single SWNT to carry ca. 20 μA [27]. Interconnects clearly require metallic CNT, and thus the simplest arrangement is to use MWNTs. There are two types of interconnects, horizontal and vertical interconnects (figure 1.5). Horizontal interconnects join FETs together in different parts of the integrated circuit. There can be many (7-8) layers of these horizontal interconnects or ' layers of metal'. Each layer is then separated by an inter-level dielectric, made up of SiO_2 doped with C,H to lower its dielectric constant. This is thermally unstable above 450°C and rather weak mechanically. Vertical interconnects are called *vias* and they pass through holes in the dielectric to join horizontal interconnects to the source, drain, or gate electrodes of a FET (Figure 1.5).

Passing now to the CNT-based FETs, a SWNT transistor with gold-electrodes could be gated by applying a potential to a gate electrode structure below the CNT. As reported by Wind et al [28], the ballistic transport and large current-carrying capacity of a CNT should take to the highest performance figure of merit of any FET so far obtained. A FET clearly requires a semiconducting CNT, so this must be a SWNT. The properties of SWNT FETs have been covered in detail by Avouris et al., Graham et al., and Javey et al.[5][15][29]. Nowadays the key unsolved issues of CNT-based FETs concern their performance, manufacturability, and cost advantage [5][29][30].

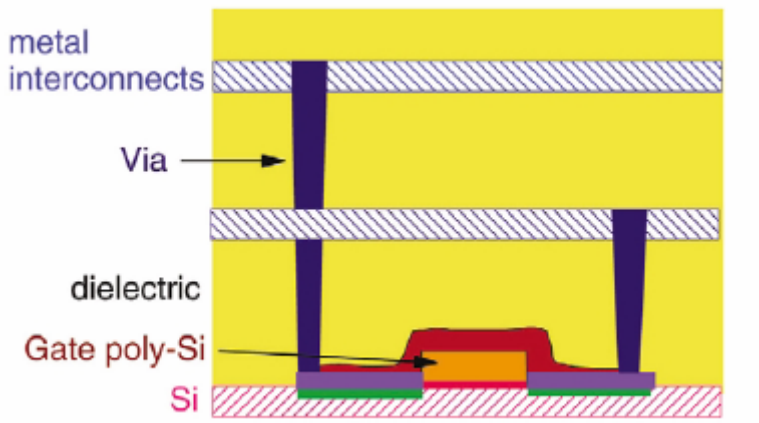

Figure 1.5 *Vertical interconnects (vias) pass through holes in the dielectric to join horizontal interconnects to the source, drain, or gate electrodes of CNT-based FETs.*

However, the higher performance of SWNT-FETs is not the only factor ruling the possibility to replace existing Si technology. Since the success of microelectronics depends also on the simultaneous production of a large number of devices on a silicon wafer, miniaturisation capability is still the main driving force to orient Research and development towards Si technology.

SWNT-FETs occupy a large wafer area compared to their diameter because of its connections, so their “economic" figure of merit is poor. In 2005 Infneon [4] proposed a solution to the packing problem with the vertical CNT-FET concept (Figure 1.6). This process offers several advantages when translated onto a larger technical scale: the vertical CNTFET has a minimum footprint that is only just larger than the nanotube diameter. The gate electrode surrounds the nanotube in a ring form and enables the most optimal gate-field penetration. The separation between the gate and electrodes and the gate length are no longer defined by the lithographic scale, but rather determined by the choice of thickness for each of the layers. Finally, any number of such modules can be grouped into larger units, as shown schematically in Figure 1.6 (b). In addition, through the free choice of their position, they are no longer confined to a particular layer and can, contrary to Si technology, lie on many layers on top of each other to build three-dimensional structures. This very promising concept has yet not been completely realized, because of SWNT semiconducting is required with a diameter of about 1 nm (so that the bandgap lies in the technologically interesting range of approximately 1 eV) and the reproducible production of nanoholes with such small diameters is extremely difficult.

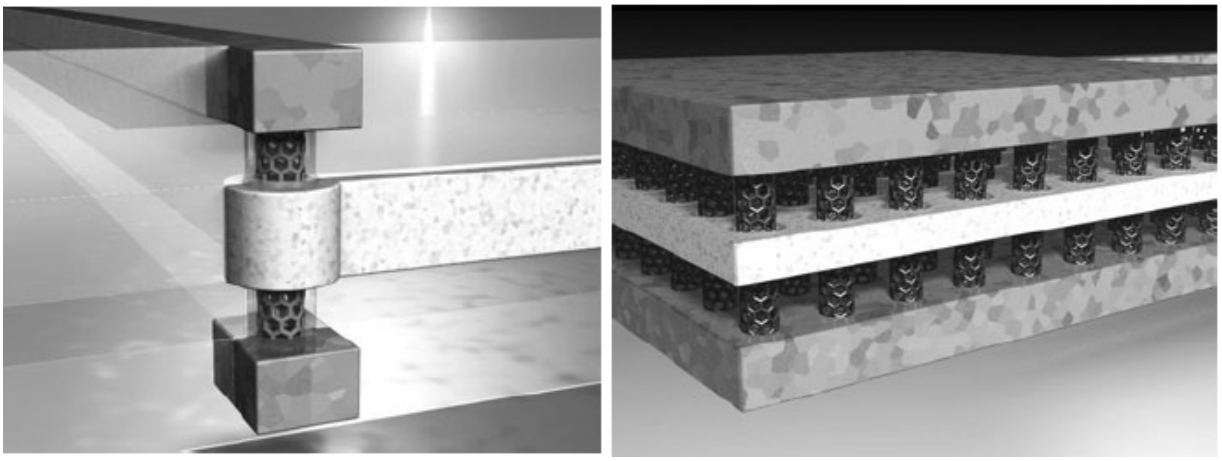

Figure 1.6 *(a) The vertical CNT-FET concept (V-CNT-FET)* [4]. *The source and drain electrodes, the nanotube, and the ring-shaped gate electrode that is insulated with a dielectric are embedded in a dielectric layer. This device has a footprint of only a few* nm^2 *for an optimum gate geometry. The position and length of the gate is not lithographically defined but rather through the much more precisely defined thickness of the individual layers. Apart from the growth of the nanotube this concept uses processes that are already used in microelectronics.(b) The V-CNT-FET concept enables two-dimensional structures comprising many transistors that can be adjusted to the desired output power.*

1.3.1.2 Field emission

In 1995, field emission property of CNT was discovered by de Heer et al. [31] by showing that an electric current could be drawn from a surface covered with CNTs. Films of both MWNT and SWNT are excellent field emitters although the necessary field emission parameters may vary in a large range. According to Fowler-Nordheim equation (Eq. 1.2), the field emission current (I) of a metal tip is related to local field strength (F) at the tip through the following equation:

$$I = \frac{K(F)^2}{\phi e^{\frac{-B\phi^{3/2}}{F}}} \qquad 1.2$$

where $B = 6.8\ 10^9\ eV^{-3/2}$, φ is the work function of CNT, and K is a constant.

The field emission current density value for a CNT is 1 mA/cm^2 with an applied electric field of 3 V/m. According to a recent study, doped CNT present improved emission properties. A review on emission properties of doped CNT has been reported [32].

CNTs have an advantage over Si or W tips, being physically inert to sputtering, chemically inert to poisoning, and do not suffer electro migration up to 10^9-10^{10} A/cm^2 [33]. MWNTs are preferred to SWNTs because of their greater mechanical stiffness. Even if a single SWNT could give an electron source with higher brightness (> 30x) and smaller energy spread (down to only 0.25 eV) compared with existing emitters, they are destined to occupy a niche market, where cost is not a problem, as electron guns for next-generation SEMs and TEMs [34]. They also show high performances as microwave amplifiers [35], where an array of equally spaced, vertically aligned nanotubes, rather than a single emitter, would constitute the active part of the device.

Another possible application is as element to build field emission displays (FEDs). The advantages of using CNTs as FEDs over active matrix liquid crystal displays (AMLCDs), commonly used nowadays, are a higher power efficiency, wider operating temperature range and a higher video rate. However, the nanotube-based FEDs market has been almost abandoned [36] because of cost reasons.

1.3.1.3 Optoelectronic properties

Not long time ago (2002) photo-luminescence (PL) from SWNTs has been observed in processed and purified CNTs coated by soap micelles in solution [37], as previously theoretically predicted. The sharp PL peak obtained at room temperature (from 1.0 to 1.6 μm and most probably beyond), suggests that SWNTs can be used in optoelectronics. As a consequence, polymer–CNT composite materials have been studied for electro-optics applications.

Loading layers of organic light emitting diodes (OLEDs) with low concentration of CNTs effectively increased the lifetime of the devices, by preventing the build-up of local hot-spots through the high thermal conductivity that can be achieved in a CNT percolation [38]. Recently, considerable research on macro-optoelectronics has focused on optimizing the performance of OLEDs by incorporating CNTs into polymer matrixes as a dopant material. It is found that the combination of CNT with polymers [38] offers an attractive route not only for reinforcing but also for introducing new properties based on morphological modification or electronic interaction between the two components.

A few years ago a new class of CNT-based transparent conducting materials that can replace indium-tin oxide (ITO) for certain applications, including OLEDs and organic

photovoltaic (OPV) devices, has been put forward. CNT-polymer films are superior to ITO in terms of the flexibility because the former can be bent without fracture.

Recently, enhanced electroluminescence (EL) and photovoltaic (PV) response was observed in single-layer LED when SWNT were introduced in conjugated polymers [19]. The detailed EL and PV studies indicated that low SWNT doping improved the bipolar charge injection leading to enhanced reverse and forward EL with reduced threshold voltages. As the concentration of SWNT increased, the interfacial exciton dissociation dominated giving rise to an increased PV response (Figure 1.7)[19].

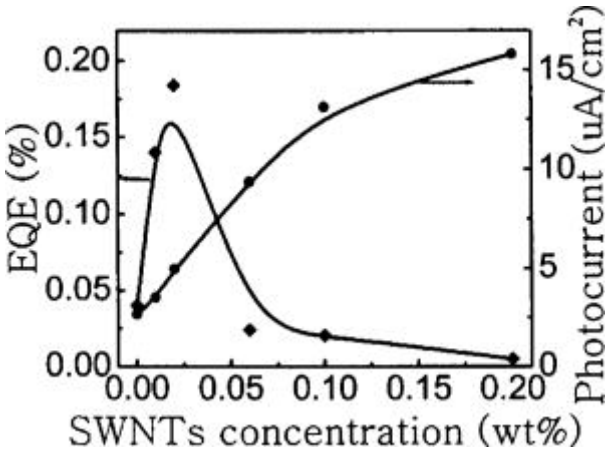

Figure 1.7 *Enhanced electroluminescence (EL) and photocurrent are shown as a function of the SWNT concentration in SWNT/polymer(2-methoxy-5-(2'-ethylhexyloxy)-1, 4-phenylenevinylene) MEHPPV based on single-layer light-emitting diodes [19] (LEDs). The external quantum efficiencies (EQE) of EL were measured at the current density of 10mA/cm^2 while the photocurrent was recorded at 0.5 V reverse bias and 0.2 mW/cm^2 illumination of 450 nm. The photocurrent density is defined as the difference between the currents measured with and without the photoillumination.*

1.3.2 Electrochemical properties

CNTs are ideal candidates for electrochemical applications because they are characterized by a large surface area and low resistivity; moreover, as already exploited by graphite, they are stable material as they are not reduced or oxidized over a wide range of applied voltages. The capacitance of the electrochemical double layer (ECDL) capacitor established between electrode and electrolyte has to be high to increase the overall efficiency of the electrochemical device. Since the capacitance is equal to C = A/d , materials with high

surface area A give an obvious advantage, also yielding high power densities (directly proportional to C). In addition, nanotubes provide better performance also than activated carbons by which it has been fabricated the first super capacitors [39], possessing the largest surface area of any other carbon and lower resistance, that leads to higher power density.
At the moment CNTs/nanofibers are used to improve the conductivity and surface area of electrodes in Li-ion batteries [40], and fuel cells. Still open issues are contacting the CNTs to the backing electrode, by a low temperatures and low cost process.

1.3.3 Mechanical properties

CNTs possess unique mechanical properties such as high stiffness, tensile strength and resilience [41-43]. A variety of experimental and theoretical methods have been used to investigate the mechanical properties of CNTs. In 1996 Treacy et al.[41] have obtained an average value of 1.8 TPa for the Young's modulus through careful TEM observations of a number of CNTs, by using the amplitude of their intrinsic thermal vibration (even if there was a remarkable scatter in the data, from 0.4 to 4.15 TPa for individual tubes). According to theoretical methods, different estimates of the Young's modulus of an individual SWNT of about 1 nm diameter have been obtained (800GPa [44], 5 TPa, [43], 0.9-1 TPa, [45] and 1.2 TPa [46]). Different calculation methods as well as choice of different SWNT wall thickness [42] are responsible for the reported values. Recently, a draw/spin method to produce a fiber directly from a CVD reactor has been developed [33][47][48]. The resulting fiber can then be post-impregnated with epoxy to make a composite or also as yearns (Figure 1.8)

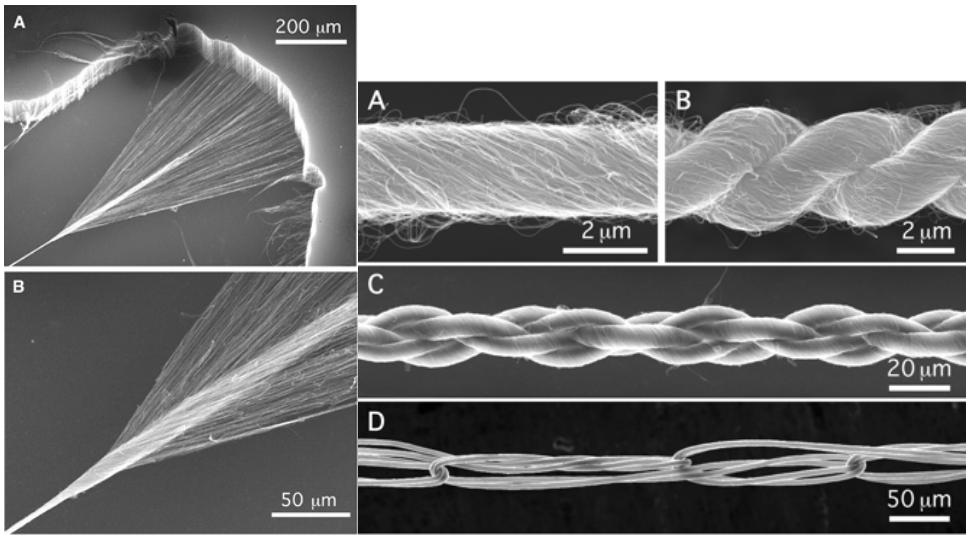

Figure 1.8 *Left: SEM images of a carbon nanotube yarn in the process of being simultaneously drawn and twisted during spinning from a nanotube forest (thick CVD nanotube film).*
Right: SEM images of (A) singles, (B) two-ply, and (C) four-ply MWNT yarns, as well as (D) knitted and (E) knotted MWNT yarns[48] with diameter of 3.2 m in diameter. They have been obtained by drawing and twisting during spinning from a nanotube forest outside the SEM. The starting MWNTs, 10 nm in diameter with length 10000 times their width, form small bundles of a few nanotubes each in the forest where the process of spinning started to obtain the yearn. During the spinning the individual nanotubes were moving in and out of different bundles.

These exceptional mechanical properties of SWNTs, together with their high aspect ratio and low density coupled with electrical peculiarities, make them ideal candidates for developing functional and structural polymer/SWNT composites [49]. In fact considering that the shear modulus of large diameter SWNT ropes is relatively low [50] (for 20 nm diameter ropes is about 1GPa and for 4 nm diameter ropes is about 6 GPa), the SWNT exfoliation becomes also important in processing composites where the aim is to improve the mechanical properties. To achieve an effective reinforcing ability, SWNTs must be well dispersed, single and not forming ropes and exhibit good interfacial bonding to achieve load transfer across the NT-matrix interface. Petroleum pitch [51], PMMA [52] and polypropylene [53] are examples of matrix systems where SWNTs have been dispersed successfully, and the oriented composite fibers with improved mechanical properties have been processed.

However, till now CNTs have not yet fulfilled the expectations, especially from the point of view of Young's modulus. Actually the Young's moduli up to now measured on composites are much lower than the theoretical values because the CNTs tend to bundle and it

is difficult to achieve a uniform CNT dispersion in the matrix. Moreover, the CNT/host interface lacks sufficient bonding to ensure a good force load transfer. An alternative approach to fabricate a structural composite, by exploiting the tendencies of tubes to bundle, is to draw a fiber made up of aligned nanotubes [54], to increase their mechanical properties by collective effects. Among the first fibers produced in this way were CNT/polyvinyl alcohol composite [55].

1.3.4 Thermal properties

The thermal properties of carbon nanotubes are of fundamental interest and also play a critical role in controlling the performance and stability of nanotube devices [56]. They present the highest axial thermal conductivity of any solid the lattice thermal conductivity λ of a (10, 10) SWNT reaches the maximum value of about 37 500 W/m K at $T \sim 100$ K, and decreases to about 6000 W/m K at $T = 300$ K. The decrease is due to anharmonic interactions that produce phonon-phonon Umklapp scattering [57,58]. This property makes them appealing for several applications ranging from thermoelectric power generation, where low thermal conductivity is desirable, to heat dissipation, requiring high thermal conductivity. Thermal expansion of MWNTs with different diameter at high temperature (1373 K in argon atmosphere) were studied [59]. In general, CNTs are progressively graphitized with high temperature [59] and graphitizability of a thin CNT is lower than a thick one because of difference in degree of curvature present in CNTs. Wu et al. [59] reported, the thermal coefficients became higher and appear to be a singular value for MWNTs with a diameter of 50 nm. In the case of SWNTs, CNTs could coalesce and transform into MWNTs at high temperature heating (2473 K at vacuum for 4 h) [59]. When MWNTs were heated at such high temperature, the CNTs collapsed into graphitic nanoribbons (GNR) driven by non-compensated van der Waal forces due to tube–tube interaction within a bundle. Many reported the irradiation of MWNTs under electron beam, during TEM analysis, results in the collapse of an isolated CNT . However, such structural transformation is a very anisotropic and a non-equilibrium process [59].

1.3.5 Hydrogen storage

Hydrogen storage in CNT has been a subject of intense research because of the large interest toward the clean energy technology. Physisorption and chemisorption phenomena on CNT are at the basis of their use as an hydrogen storage material. Theoretical calculation shows that the interaction could vary between 0.11 eV for the physisorbed hydrogen molecule to ca. 2.5 eV for the chemisorbed hydrogen atom [60]. The physisorption mechanism should involve the condensation of hydrogen molecules inside or on the external walls of the CNT. The chemisorption mechanism should occur through dissociation of hydrogen molecules on a catalyst followed by reaction with the unsaturated carbon-carbon bonds to form carbon-hydrogen bonds [61].

However, so far conflicting results have been published concerning the reversible storage of hydrogen in nanotubes [62]. Such a large variation in experimental values on storage of hydrogen could be partially attributed [60] to different types of impurities, such as amorphous carbon, water, hydrocarbon, and to rather different sizes of the investigated CNTs. The controversy about the hydrogen storage capability is mostly caused by insufficient characterization of the used samples. At the beginning the studies suggested a storage capacity of 60 % wt, but subsequently more realistic estimates reported a 8-10 % wt value. Anyway, it turned out that the hydrogen storage capacity of nanotubes is less than 1% [63], which is not enough to define CNTs as a material useful for realistic devices for hydrogen storage.

1.3.6 Gas chemical sensor

In the last few years, it has become evident that the measured electronic properties of CNT and electrical contacts are greatly affected by the ambient they are exposed to. In particular, they exhibit a high sensitivity at room temperature to oxygen, nitric oxide, carbon monoxide, carbon dioxide and ammonia, as demonstrated by several works [64][65] where either SWNTs or MWNTs have been deposited on interdigitated electrodes. It has been also demonstrated that the electronic properties of CNT are extremely sensitive to the presence of molecular oxygen because of the formation of charge transfer complexes.

1.3.7 CNTs in nanobiotechnology

1.3.7.1 Biosensor electrodes

Nanoscience has extended its influence into biotechnological and biomedical applications. Drug delivery, tissue engineering, scaffold synthesis, biosensors, bioseparation, biocatalysis and enzyme immobilization are a few example of the potential applications of the one dimensional nanostructures. Among the nanostructures useful for bio-applications, CNTs can play an important role. In the past several years, there has been a steady increase in activities that incorporate CNTs into biological systems, including proteins, DNA, and living cells [66]. Their importance is associated to the enhancing induced by CNT of the electrochemical activity of important biomolecules [67] [68] by promoting electron transfer reactions. As a consequence, CNT functionalized biosystems have been exploited in a wide range of electrochemical biosensors.

1.3.7.2 Drug delivery

Nanotechnology had a relevant impact also on drug delivery, influencing several routes of delivery from oral to injectable. In order to make an efficient drug delivery, the carrier should be able to cross the cell membranes. It has been shown that properly functionalized CNT can cross the cell membranes effectively even if the mechanism of this uptake is not clear if it could be toxic [69] [70]. So far CNTs have been used as vessels for delivering peptides, nucleic acids and drugs. There are two basic approaches to CNT functionalization for applications in drug delivery: either a covalent addition or adsorption to the tips and sidewalls of CNT or oxidization to generate carboxylic groups, both increasing the CNT solubility in aqueous solutions [54].

Bibliography

[1] Feynmann R., *Engineering and Science*, page 22, Caltech, (1960).

[2] MooreG., IEEE, International Electron Devices Meeting (1975).

[3] Robertson J., *Materials Today* 10,69 (2007).

[4] Andrew P. G.,. Duesberg G. S., Seidel R.V., Liebau M., Unger E.,

Pamler W., Kreupl F., and Hoenlein W., S*mall* 1, 382 (2005).

[5] Lundstrom M., *Science* 299, 210 (2003).

[6] Tans S.J. et al. *Nature* 386, 475 (1998).

[7] Javey A., Kim H., Brink M., Wang Q., Ural A., Guo J., McIntyre P., McEuen P., Lundstrom M., Dai H., *Nature Mater*. 1, 241 (2002).

[8] Guo J.et al., IEDM Tech. Digest (IEEE, Piscataway, NJ,2002), pp. 711–714.

[9] Saito R., Dresselhaus G.,Dresselhaus M. D., *Physical Properties of Carbon Nanotubes*, Imperial College Press, London, (1998).

[10] Nagashima A., Tejima N., Oshima C., *Phys. Rev. B* 50,17489 (1995).

[11] Rosei R., Modesti S., Sette F., Quaresima C., Savoia A., Perfetti P., *Phys. Rev. B* , 29, 3416 (1984).

[12] Kroto H. W., Heath J. R., O'Brien S. C., Curl R. F. and Smalley R. E, *Nature* 318, 162 (1985).

[13] Iijima S., *Nature*, 354, 56 (1991).

[14] Avouris P. et al,*Tech. Digest IEDM* , 525 (2004).

[15] Avouris P. and Chen J., *Materials Today* 10, 46 (2006).

[16] Hansson A., Paulsson M., Stafstrom S., *Phys. Rev. B* 62, 7639 (2000).

[17] Rochefort A., Avouris P., Lesage F., Salahub D.R., *Phys. Rev. B* 60, 13824 (1999).

[18] Plank N.O.V., Forrest G.A., Cheung R., Alexander A.J. , *J. Phys. Chem. B* 109, 22096 (2005).

[19] Xu Z.H., Wu Y., Hu B., Ivanov I.N., Geohegan D.B., *Appl. Phys. Lett*. 87, 263118 (2005).

[20] Lee R.S., Kim H.J., Fischer J.E., Thess A., Smalley R.E. , *Nature* 388, 255 (1997).

[21] Tans S.J.V., Verschueren A.R.M., Dekker C., *Nature* 393, 49 (1998).

[22] Collins P.G.Z., Zehl A., Bando H., Thess A., Smalley R.E., *Science* 278, 100 (1997).

[23] Tien L.G., Tsai C.H, Li F.Y., Lee M.H., *Phys. Rev .B* (Condensed Mat Mater Phys), 72, 245417 (2005).

[24] Milne W. I., et al., *J. Mater. Chem*.14, 933 (2004).

[25] Rueckes T., et al., *Science* 289, 94 (2000).

[26] Collins P.G.Z., Zehl A., Bando H., Thess A., Smalley R.E., *Science* 278, 100 (1997).

[27] Yao Z., Kane C. L., and Dekker C., *Phys. Rev. Lett*. 84, 2941 (2000).

[29] Javey A., et al., *Nature. Mater*.1, 24121 (2002).

[28] Wind S. J., et al., *Appl. Phys. Lett*. 80, 3817 (2002).

[30] Javey A., et al., *Nano Lett*. 4, 1319 (2004).

[31] De heer W.A., Chatelain A., Ugarte D., *Science* 270, 1179 (1995).

[32] Zhou G., Duan W. J., *Nanosci. Nanotechnol*. 5, 1421 (2005).

[33] Li J., Ye Q., Cassell A., Ng H. T., Stevens R.,Han J., Meyyappan M., *Appl. Phys. Lett*. 82, 2491 (2003).

[34] De Jong K. P. and Geus J. W., *Catal. Rev*. 42, 481 (2000).

[35] Yue G. Z., Qiu Q., Gao B., Cheng Y., Zhang J., Shimoda H. S. C., Lu J. P., Zhou O., *Appl. Phys. Lett*. 81, 355 (2002).

[36] Choi W. B., et al, *Appl. Phys. Lett*. 75, 3129 (1999).

[37] Bachilo S.M., Strano M. S., Kittrel C., Hauge R. H., Smalley R. E., and Weisman B.R., *Science* 298, 2361 (2002).

[38] Baxendale M., *J Mater Sci: Mater Electron* 14, 657 (2003).

[39] Emmenegger C., Mauron, P. Sudan, P. Wenger, P. Hermann, V. Gallay, R. Zuttel, A.

J. Power Sources 124, 321 (2003).

[40] Endo M., Kim Y. A., Hayashi T., Nishimura, Matusita K. T., Miyashita K. and Dresselhaus M. S., *Carbon* 39, 1287 (2001).

[41] Treacy M. M. J., Ebbesen T. W., Gibson J. M., *Nature* 381, 678 (1996) .

[42] Wong E.W., Sheehan P. E. and Lieber C. M., *Science* 277, 1971 (1997).

[43] Yakobson B. I., Brabec C. J., Bernholc J. , *Phys. Rev. Lett*. 76, 2511 (1996).

[44] Cornwell C. F. , Wille L. T., *Solid State Commun*. 101, 555 (1997).

[45] Lu J. P. , *Phys. Rev. Lett*. 79, 1297 (1997).

[46] Hernandez E., Goze C. , Bernier P., Rubio A., *Phys. Rev. Lett* . 80, 4502 (1998).

[47] Zhang M., Fang S., Zakhidov A. A., Lee S.B., Aliev A. E., Williams C. D., Atkinson K. R., Baughman R. H., *Science* 309, 1215 (2005).

[48] Zhang M., Atkinson K. R., Baughman R.H., *Science* 306, 1359 (2006).

[49] Baughman R. , *Science* 297, 787 (2002).

[50] Salvetat J. P., Bonard J. M., Thomson N. H., Kulik A. J., Forro L. Benoit W., Zuppiroli L., *Appl. Phys. A,* 69 255 (1999).

[51] Andrews R., Jacques D., Rao A. M., Rantell T., Derbyshire F., Chen Y., Chen J., Haddon R.C., *Appl. Phys. Lett.* 75, 1329 (1999).

[52] Haggenmueller R., Gommans H. H., Rinzler A. G., Fischer J. E., Winey K. I.,*Chem. Phys. Lett*. 330, 219 (2000).

[53] Kearns J. C., Shambaugh R. L. J., *Appl. Polym. Sci*. 86, 2079 (2002).

[54] Liu T. and Kumar S., *Nano Lett*. 3, 647 (2003).

[55] Dalton A. B., Collins S., Munoz E., Razal J. M., Ebron V. H., Ferraris J. P., Coleman J. N., Kim B. G., Baughman R. H., *Nature* 423, 703 (2003) .

[56] M. S. Dresselhaus, G. Dresselhaus, and P. C. Eklund, *Science of Fullerenes and Carbon Nanotubes* (Academic, San Diego, 1996).

[57] P. Kim et al*., Phys. Rev. Lett.* 87, 215502 (2001).

[58] J. Hone et al., *Phys. Rev. B* 59, R2514 (1999).

[59] Kim U.J., Gutierrez H.R., Kim J.P., Eklund P.C., *J. Phys. Chem. B* 109, 23358 (2005).

[60] Nikitin A. et al., *Phys. Rev. Lett* .95, 225507 (2005).

[61] Yoo E. et al., *J. Phys. Chem.* B 108, 18903 (2004).

[62] Schlapbach L. and Zuttel A., *Nature* 414, 353 (2001).

[63] Kajiura H., Tsutsui S., Kadono K., Kakuta M., Ata M., *Appl. Phys. Lett*. 82, 1105 (2003).

[64] Baxendale M., *J. Mater Sci: Mater Electron* 14, 657 (2003).

[65] Kong J. et al., *Science* 287, 622 (2000).

[66] Lin Y., Taylor S., Li H. P., Fernando K. A. S., Qu L. W., Wang W., Gu L. R., Zhou B. , Sun Y. P., *J. Mater. Chem*. 14, 527 (2004).

[67] Zhao Q., Gan Z.H., Zhuang Q.K., *Electroanalysis* 14, 1609 (2002).

[68] Musameh M., Wang J., Merkoci A., Lin Y.H., *Electrochem. Commun.* 4, 743 (2002).

[69] Pantarotto D., Briand J.P., Prato M., Bianco A., *Chem. Commun*. 1,16 (2004).

[70] Miyawaki J., Yudasaka M., Azami T, Kubo Y., Iijima S., in press *ACS NAno*

Chapter 2

Synthesis techniques

In this chapter we describe the synthesis technique used to synthesize SWNT and MWNT. In the first section 2.1 we present the early CNT, and then the second section 2.2 is divided in different subsections, where each one describes a different growth techniques. The 2.3 section present with more details the growth technique used in this work (surface-bound CVD) and some of the last achievement in the growth. Finally the 2.4 section underlines the useful of the surface bound CVD also to study the mechanism of growth of CVD.

2.1 Before carbon nanotubes

The history of carbon science is started more than 100 years ago and it continues to advance rapidly. Carbon fibers and filaments have been studied by Hughes and Chambers [1] in 1889 and 1890: they generated carbon filaments by flowing cyanogen over porcelain at ´cherry red´ heat. In the early 1950s, Radushkevich and Lukyanovich [2] published a report on hollow carbon fibers (Figure 2.1). Some years later, in 1953, Davis et al. [3]. described thread-like structures obtained by the interaction of carbon monoxide and iron oxide in the so-called iron-spots in the brick. It was one of the earliest reports of carbon nanofibers (CNFs) growth in the past century. The structures were described as layered threads, varying in thickness from 10 to 200 nm. The thicker strands appeared to be composed of many finer threads twisted into helical structures. At that time the demand by the space and aerospace industry for stronger, lightweight materials with improved mechanical properties has lead to substantial progress in the production and characterization of carbon filaments and hollow carbon fibers. It was soon realized that generating highly crystalline carbon fibers resistant to crack propagation would

have required further developments of growth methods such as chemical vapor deposition (CVD).

In that context (1970s-1980s), two opposing issues motivated researchers to investigate the mechanisms of carbon filament growth: the inhibition and the optimization of the growth process. The inhibition was studied because carbon formation is detrimental in systems such as nuclear reactors.

Figure 2.1 L*ow-resolution transmission electron micrograph depicting three hollow carbon fibers at MAG 20 000. These fibers were first reported by Radushkevich and Lukyanovich in 1950[2]* .

During those years, Baker et al. [4,5] contributed enormously to the field, widely studying the pyrolysis of hydrocarbons and of CO over transition metal catalysts yielding graphite filaments, CNFs and CNTs.

In the 1970s, Endo et al. [6] showed a high-resolution transmission electron microscopy (HRTEM) picture (Figure 2.2) of what is now called a single - or double walled CNT (SWNT or DWNT). At that time, although electron microscopes were powerful enough to study the structure of the carbon filaments in detail, the images did not reveal the number of walls clearly so it was not possible to determine whether the CNT consisted of one or two concentric graphene cylinders [6,7]. The carbon fiber community was familiar with filament-like structures and did not pay further attention to nanoscale objects like the CNTs observed by Endo et al. [6] [Figure 2.1 (a),(b)].

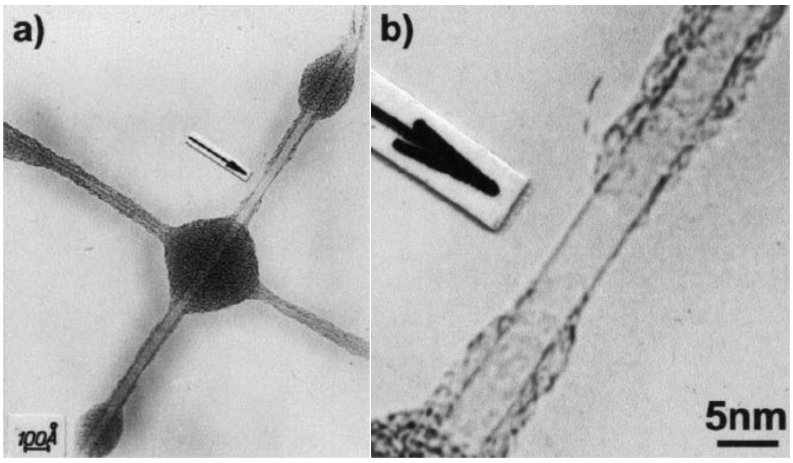

Figure 2.2 *HRTEM image of two crossing (a) CNTs produced by catalytic processes reported by Endo et al. in 1976 [6]. The diameter of tube is ~ 4 nm (b) and magnification of one of the two crossing tubes.*

Whereas the research was focused on generating carbon fibers from polymer-based precursors, graphitic nanofibers were considered unwanted products causing poisoning [8] of metal catalyst particles or damage to reactor walls in furnaces [9]. This process was also known as metal dusting or corrosion [8-10].

Only the paper entitled " Helical microtubules of graphitic carbon " published by Iijima in 1991 [11] caused an unexpected change in carbon science. Iijima [11] was fascinated by the Krätschmer-Huffman paper on the lab-scale production of C_{60} [12] and he examined soot produced by the Krätschmer-Huffman method provided by Endo [13] using HRTEM and the he published the well known images of CNTs .

2.2 Growth methods

CNTs (single or multiwalled) can be produced using several methods. Each technique offers advantages and disadvantages. In the following section, the main methods are presented summarizing the processes and their main advantages and drawbacks.

2.2.1 Arc discharge

Highly crystalline MWNTs, first identified by Iijima [11], were produced in bulk by varying the parameters of the dc arc discharge apparatus (voltage, current, and helium pressure, Figure 2.3) employed for fullerene production.

The optimal conditions for nanotube generation involve passage of a direct current (80–100 A) through two high purity graphite (6–10 mm o.d.) electrodes (separation about 1–2 mm) in a helium atmosphere (500 torr), a schematic representation of the experimental apparatus is shown in Figure 2.3. During arcing, a deposit forms at a rate of 1 mm min^{-1} on the cathode (negative electrode), while the anode (positive electrode) is consumed. This deposit exhibits a cigar-like structure (Figure 2.4), in which a grey hard shell is deposited on the periphery. The inner core, which is dark and soft, contains carbon nanotubes and nested polyhedral graphene particles. Scanning electron microscopy (SEM) images of the cathode deposit indicate that the grey outer shell consists of curved graphene layers. However, the dark and soft inner core deposits are composed of bundle-like structures, exhibiting randomly arranged nanotubes and graphitic particles (Figure 2.5).

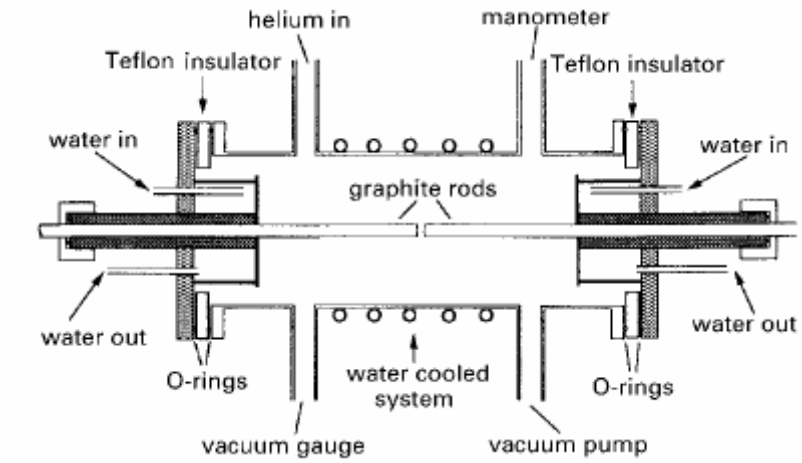

Figure 2.3 *Schematic diagram of arc discharge apparatus employed for fullerene and nanotube production*

Figure 2.4 *Different views of typical cathode deposit obtained after arcing two graphite electrodes in He atmosphere: a low resolution of bundle consisting of smaller aligned a cross-section of deposit exhibiting cigar-like structure, with inner core (in black) and hard outer shell (in grey); b side view of same deposit showing only grey outer hard shell.*

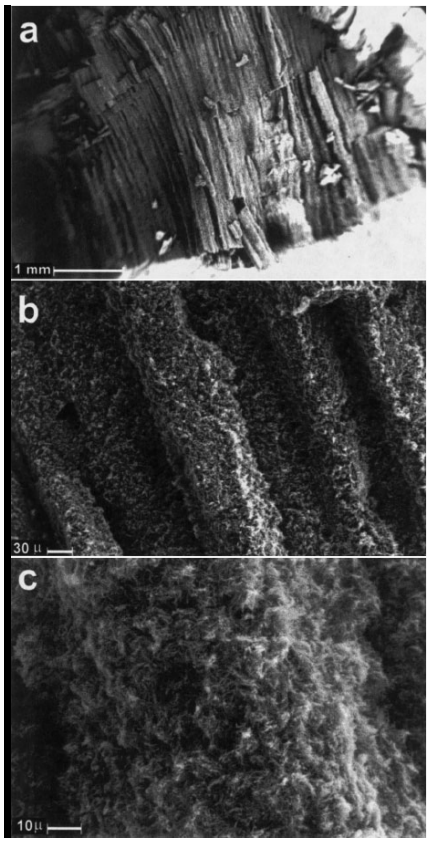

Figure 2.5 *SEM images obtained from inner core C deposit showing bundled structures: a low resolution of bundle consisting of smaller aligned bundles; b higher magnification of aligned bundles; c individual bundle exhibiting nanotubes randomly oriented*

Single-walled nanotubes can also be produced using the arc discharge method, but they require mixed metal catalysts, such as Gd, Co-Pt, Co-Ru, Co, Ni-Y, Rh-Pt, Co-Ni-Fe-Ce, Fe-Co, and Ni-Y [14-16],that are inserted into the anode . Journet et al. [14] found that high yields up to 90 % of SWNTs [1.4 nm average diameter, Figure 2.6(b)] could be obtained by using Ni-Y. This Ni-Y mixture is now used worldwide for production of SWNTs in high yield. After arcing, SWNTs are found distributed in the chamber as a fluffy web-like material. The arc discharge routes are now able to generate bundles of SWNTs in gram quantities per day. However ,it is important to note that the nanotube yield is also very dependent on the chamber geometry and cooling system. Recently, alternative arc discharge plasma jet methods using metal-doped graphite electrodes have also been developed in order to produce larger quantities of SWNTs (e.g. 1.2 g min^{-1}).

MWNTs obtained by the arc-discharge are highly crystalline, have few defects, and are straight, whereas MWNTs obtained by CVD (see section 2.2.4) are longer, exhibit larger diameters, are highly defective, and are not straight. Defects influence not only the electronic structure but also the mechanical properties [17]. This may help to understand why the Young's modulus of MWNTs obtained by CVD is orders of magnitude smaller than the Young's modulus of those obtained by the arc-discharge method. SWNTs produced by the same method appear as bundles [14]. Their diameter ranges from 1-2 nm. It remains difficult to measure the SWNT length accurately because of the entanglement of the SWNT bundles. The SWNTs in the bundles exhibit a collection of different chiralities. Arc-discharge MWNT and SWNT samples commonly contain substantial amounts of byproducts, such as amorphous carbon and polyhedral carbon.In SWNT samples, encapsulated metal catalyst particles are also present.

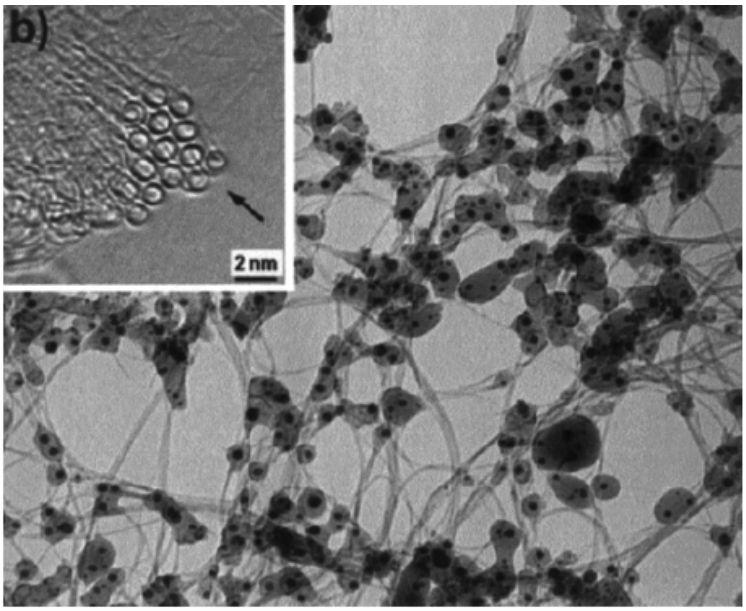

Figure2.6 *SEM images (Journet et al.[14])obtained from inner core C deposit showing bundled structures : TEM image of SWNT bundles produced in arc discharge using graphite–Ni–Y electrodes in presence of He: main image shows dark contrast areas caused by Ni and Y metals and ropes consisting of SWNTs and inset shows cross-section of individual rope, which is composed of 14–15 SWNTs of diameter ~1. 4 nm.*

The resulting carbon reaction products are collected from the reactor and dispersed in a suitable solvent. The amorphous C remains are eliminated using various cleaning processes. Subsequently for applications in microelectronics, a separation of the semiconducting and metallic tubes is possible in this ex situ methods [18] .

2.2.2 **Laser-vaporization or laser-ablation technique**

The laser- vaporization technique operates at similar conditions to arc discharge. During fullerene production experiments using a laser vaporization apparatus with an ablated graphite sample positioned in an oven, it was found that closed-ended MWCNTs were produced in the gas phase through homogeneous carbon-vapour condensation in a hot argon atmosphere.

Both methods arc discharge and laser ablation use the condensation of carbon atoms generated from the vaporization of graphite targets. The laser ablation SWNTs are formed when graphite targets, containing catalysts, such as Ni, Co, and Pt [19,20], are vaporized by a laser. Here, the graphite target is placed in a quartz tube surrounded by a furnace (at ca. 1200

°C). A constant gas flow (Ar or He) is passed through the tube in order to transfer the soot generated to a water-cooled Cu collector (Figure 2.7). Evaporation of a carbon-metal composite target with laser light pulses, either separate or frequently repeated, and with continuous illumination by laser and solar light, can bring about SWCNT formation. This technique favours the growth of SWNTs (Figure 2.8); MWNTs are rarely produced and relatively short, approximately 300 nm, although the number of layers, ranging between 4 and 24, and the inner diameter, varying 1.5–3.5 nm. By products such as amorphous carbon or encapsulated metal catalyst particles are also present.

The quality, length, diameter, and chirality distribution of the material are believed to be comparable with those of SWNTs grown by arc discharge [21]. The SWNTs usually condense as ropes or bundles consisting of several individual SWNTs whose average diameter is about 1.3 nm [22]. More recently, Eklund and co-workers [23] reported that ultrafast (subpicosecond) laser pulses are able to produce large amounts of SWNTs. The authors demonstrated that it is possible to produce nanotube material at a rate of up to 1.5 g h^{-1}.

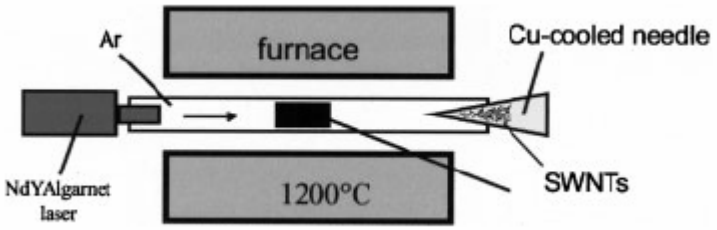

Figure 2.7 *Experimental set-up for production of SWNTs and MWNTs using laser technique: high power laser is focused on composite graphite target (in Ar atmosphere) located inside furnace at 1200°C – tubes are collected from Cu-cooled water trap.*

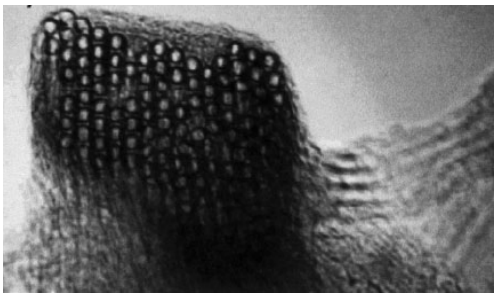

Figure 2.8 *TEM image of cross-section of SWNT bundle showing various tubes of same diameter (images from Richard Smalley's web page)*

Also for this *ex situ* technique, the resulting carbon reaction products needs to be purified and they are collected from the reactor and dispersed in a suitable solvent.
We mention also that the laser technique [24] is not economically advantageous because the process involves high purity graphite rods, the laser powers required are high (in some cases two lasers need to be used), and the amount of nanotubes that can be produced per day is not as high as for arch discharge.

2.2.3 Electrolysis

Electrolysis is a less common method for CNT production. To date, it is the only condensed phase method for generating CNT, and was developed by Hsu et al. in 1995 [25,26]. MWNTs are formed when a current is passed through two graphite electrodes immersed in molten ionic salts, such as LiCl at 600°C. After electrolysis, the carbonaceous material is extracted by dissolving the ionic salt in distilled water and separating the dispersion by filtration. The material produced containsMWNTs, carbon-encapsulated metal particles from the salt ions, amorphous carbon, and carbon filaments [25]. Adding less than 1 wt.% of other salts, such as $SnCl_2$ or $PbCl_2$, results in the formation of metal nanowires coated with amorphous carbon [25,27,28]. So far, only the generation of MWNTs has been reported, while the formation of SWNTs via electrolysis has not been observed. MWNTs possess diameters of 10-20 nm, consist of only a few walls, e.g. 10-15, and are estimated to be >500 nm long. MWNTs occur predominantly in entangled bundles also containing amorphous carbon, spheroidal carbon particles, and metal-encapsulated particles.

For the no possibility to obtain SWNTs and because it is quite difficult to control the nanotube yield and dimensions (diameter and length), the electrolytic method has not been widely used. However, further studies need to be carried out, because this route may be of advantage due to the low cost involved.

2.2.4 Chemical vapour deposition (CVD)

Chemical vapour deposition or CVD is a generic name for a group of processes that involve the deposition of solid material by chemical reactions between a gaseous precursor

and a substrate; this process is commonly used in the semiconductor industry for the deposition of thin films of various materials.

Generally, in a CVD process [29], the substrate is maintained at high temperature and is exposed to the volatile precursor/s usually carried by an inert carrier gas (like Ar) which flow over in contact with the substrate; the high temperature is usually required to react and/or decompose the precursors forming the desired solid phase which is eventually deposited onto the substrate (Figure 2.9 illustrate a typical fournace) . In the case of CNT growth, the CVD process consists in thermolysis or pyrolysis of hydrocarbons (e.g. methane, benzene, acetylene, naphthalene, ethylene, etc.) catalyzed by metals (e.g. Co, Ni, Fe, Pt and Pd) deposited on the substrates (such as silicon, SiO_x, MgO, Al_2O_3,ect).

The gas precursor is often diluted with hydrogen, ammonia, or water to be slightly etching, so that no soot or amorphous carbon grows in catalyst free regions. It is important that co-deposition of amorphous carbon is avoided. To increase the precursor gas decomposition during the growth, the CVD process may be assisted by a plasma, and in this case the technique is referred as plasma-enhanced PE-CVD. This method differs from CVD in that the precursor gas molecules are activated by a plasma generated by applying a DC current between two conductive electrodes crossing the space filled with a low pressure (generally between few mTorr to a fews Torr) of the precursor gas [30]. In the plasma the electrons are so light compared to atoms and molecules that energy exchange between the electrons and neutral gas is very inefficient. Therefore, the electrons can be maintained at very high equivalent temperatures, tens of thousands of K, equivalent to several eV average energy, while the neutral atoms remain at the ambient temperature (cold plasma). These energetic electrons can induce many processes that would otherwise be very improbable at low temperatures, such as dissociation of precursor molecules and the creation of large quantities of free radicals. Another benefit of deposition within a discharge arises from the fact that electrons are more mobile than ions. As a consequence, the plasma is normally more positive than any object it is in contact with, as otherwise a large flux of electrons would flow from the plasma to the object. The voltage between the plasma and the objects is normally dropped across a thin sheath region. Ionized atoms or molecules that diffuse to the edge of the sheath region feel an electrostatic potential and are accelerated towards the neighboring surface. Thus all surfaces exposed to a plasma receive energetic ion bombardment. The potential across the sheath surrounding an electrically-isolated object (the floating potential) is typically only 10-20 V, but much higher sheath potentials are achievable by optimization of reactor geometry and configuration.

The application of this technique to grow CNT provides two advantages with respect to the thermal CVD method: a lower substrate temperature (this is often a critical parameter in the manufacture of semiconductors) and the a preferential vertical alignment of nanotubes due to the interaction with the electric field [31-34].During the last ~15 years several plasma sources have been designed to be employed for the deposition of dielectric thin films for semiconductor circuits (and carbon-based thin films).These variety of PE source have been started to be apply also to grow of CNTs . The simplest case of PE source is a DC diode-type reactor; other examples are the DC-current PECVD [31,35], hot-filament (HF-PECVD) [33,34], magnetron-type [36] and microwave (MW-PECVD) [37,38].

Recently, to scale up the CNT production, many efforts have been directed to decrease the growth temperature. Several reports of CNT growth by PECVD at temperatures as low as room temperature (never obtained by simple thermal CVD) appeared in the literature [39,40]. In other words, by inducing on a pre-dissociation of the carbon precursor gas the energy barrier is lowered and it is possible to grow SWNT at low temperature. One drawback of the reduction of nanotube growth temperature (below 400 °C), is the decrease of the crystalline quality and the rise of the number of defects. Therefore, to obtain CNTs with high crystalline quality, others routes are to be pursued. Recently it has been reported [41] that a careful monitoring of the pre-growth treatments and of the thermal CVD growth conditions leads to the synthesis of CNFs at temperatures as low as 200 °C and SWNTs at about 400 °C.

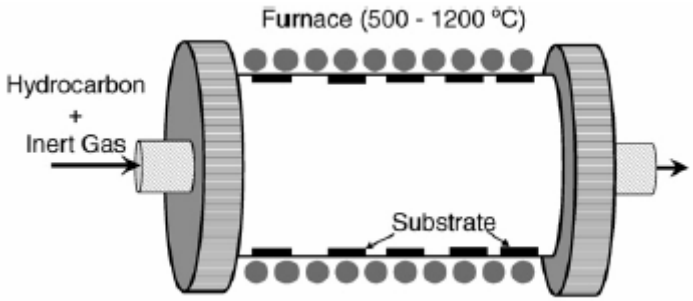

Figure 2.9 *Schematic illustration of the CVD fournace [29].*

2.2.5 **Gas-phase catalytic growth from carbon monoxide : high pressure CO disproportionation (HiPCO)**

Many groups have investigated gas-phase continuous-flow production of carbon fibers since a continuous-flow synthetic method, in which SWNTs are grown and separated in a flowing gaseous feedstock mixture, could produce SWNTs in large quantities. Such schemes would involve introducing into the feedstock flow stream nanometer-size catalyst particles on which the individual tubes nucleate and grow. The catalyst particles could be either pre-made or produced in situ by the introduction of metal-containing species into the flow and their subsequent condensation into appropriately sized clusters. The latter technique is especially convenient, because metal can be introduced in the form of volatile organometallic molecules. These studies typically involve passing a mixture of carbon source gas and organometallic catalyst precursor molecules through a heated furnace. The organometallics decompose and react, forming clusters on which carbon fibers nucleate and grow. Tibbets et al. [42] have reported gas-phase synthesis of carbon fibers in heated flowing mixtures of methane or hexane with organometallics such as iron pentacarbonyl ($Fe(CO)_5$) and ferrocene[dicyclopentadienyl iron-($Fe(Cp)_2$)][43].

C.N.Rao and co-workers [44,45] have investigated the catalytic growth of carbon nanotubes in gas phase, both by direct pyrolysis of ferrocene and other metallocenes and by catalytic decomposition of hydrocarbons or carbon monoxide in the presence of metal-locenes or $Fe(CO)_5$. In two of these studies, it is reported the production of SWNTs from mixtures of $Fe(CO)_5$ with acetylene and benzene. However, hydrocarbons pyrolize readily on most surfaces heated above 600-700°C (temperatures required for growth of SWNTs), forming graphitic deposits or amorphous carbon. Nanotubes grown in heated flows of gaseous hydrocarbons often show substantial amorphous carbon overcoating, which would need to be removed in subsequent processing steps. One may anticipate that such effects would complicate efforts to scale up production methods using hydrocarbon feedstocks.

Another method for the catalytic production of SWNTs in a continuous-flow gas-phase process, uses CO as the carbon feedstock and $Fe(CO)_5$ as the iron containing catalyst precursor. This method permits to limit the amorphous carbon overcoating and to obtain SWNTs with diameters mostly in the range 0.8-1.5 nm [46] , especially it is possible to obtain d= 0.7 nm, which are expected to be the smallest achievable chemically stable SWNTs. The diameters distribution depends on the conditions and flow-cell geometry used. The average

diameter of HiPco SWNTs is approximately 1.1nm, which is typically smaller than SWNTs produced by the laser-oven process, where the average diameter is about 1.3 nm [22] .A typical procedure [47] consists of flowing CO mixed with a small amount of $Fe(CO)_5$ through a heated reactor (Figure 2.10). The products of $Fe(CO)_5$ thermal decomposition(probably Fe(CO)n , *n*=0–4) react to produce iron clusters in gas phase.

These clusters act as nuclei upon which SWNTs nucleate and grow: solid carbon is produced by CO disproportionation (the Boudouard reaction):

$$CO + CO \rightarrow C(s) + CO_2$$

which occurs catalytically on the surface of the iron particles. These particles also promote the formation of the tube's characteristic graphitic carbon lattice. The flow cell apparatus consists of a thick-walled quartz flow tube contained within a tube furnace, through which reactant gases are flowed (pressure up to 10 atm). The tube section inside the furnace is maintained between 800 and 1200°C, while the tube entrance and exit were maintained at room temperature.

The amount and quality of SWNTs produced depends on the rate at which the reactant gases were heated. In some experiments the CO and $Fe(CO)_5$ are introduced through a water-cooled injector positioned inside the quartz tube, which maintained the gases at low temperature until they were injected into the furnace, resulting in rapid heating. The gas mixture many times consists of CO (1–10 atm, flowing at 1–2 standard liters per minute) dosed with a small amount (0–25 mTorr) of gaseous $Fe(CO)_5$. Around the exit of this injector could be positioned a circle of narrow-gauge needles through which preheated CO was passed at high flow rate to mix with the cool flow emerging from the injector, further increasing the heating rate of the injected gas. The CO sprayed from this 'showerhead' mixer is preheated by passing through a spiral heat exchanger positioned within the furnace. Flow of $CO/Fe(CO)_5$ mixtures through the heated reactor results in black deposits on the walls of the quartz tube outside the furnace. These deposits consisted of SWNTs and iron particles apparently overcoated with carbon.

Concluding , this method present two advantages over other SWNT production methods. The first one is the possibility to produce SWCNTa as small as 0.7 nm in diameter , and the size and diameter distribution of the nanotubes produced can be roughly selected by controlling the pressure of CO in which the reaction occurs. The second one it is a continuous-flow process rather than a batch process, and should be able to be scaled up to

produce SWNTs in much larger quantities (many potential applications of SWNTs require kilogram to ton quantities instead of few grams current available).

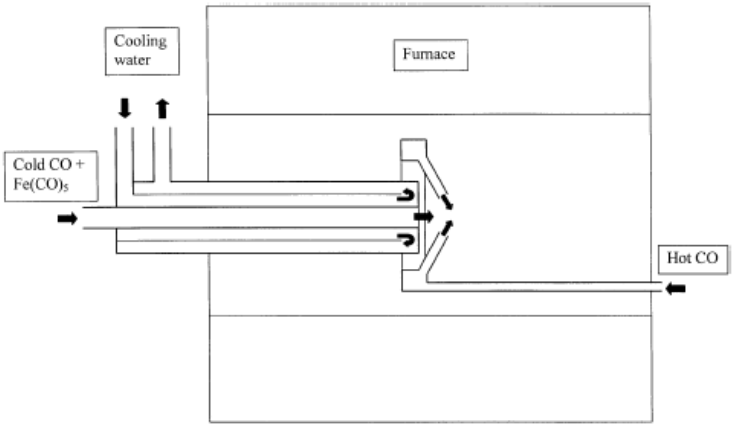

Figure 2.10 *Layout of CO flow-tube reactor, showing water-cooled injector and 'showerhead' mixer.*

2.3 Surface- bound CVD process and recent advances

Arc-discharge, laser vaporization and electrochemical growth techniques failed in front of the requirements of purity, crystallinity, single SWNT (not bundled) growth and especially the possibility to grow *in situ* aligned CNT on a wide range of substrates, needed for application in electronic and sensors field. At the moment these techniques are only used to produce small quantities (grams) of CNTs, purified from impurities, such as non-CNT carbon and catalyst materials, significantly increasing the CNT production costs.

The only techniques suitable for scaling up the CNT production for electronic and sensor applications is CVD, which presents all the qualities, mentioned above, required for application in electronic and sensors field. This because it permits to have a site-selective synthesis, to directly deposit CNTs onto a chip, and it permits low temperatures and low cost growth. The growth temperatures in CVD can be lower than 450 °C which is the limiting temperature for processing FETs. In addition CNTs only grow where there is a catalyst, typically Fe, Co or Ni; this allows to have a selection of the places where obtaining the growth. Also for FE display production, the growth temperature must be lower than the melting temperature of soda lime glass substrates (500°C) [48]. For sensors and electronic

application (FETs) it is desired to have control not only on the CNT location but also to their orientation [49].

Concerning vertical alignment, the literature reports that it can be only reached by CVD (supported by particular substrates) or by using PECVD (as mentioned in the previous section).The vertical dense alignment of the CNTs is due to a steric effect which develops Van der Waals interactions between the CNTs [50]. As mentioned above, a goal for scaling up of CNT production is the decreasing of the temperature growth. By CVD the lowest temperature reported in the literature so far is 350°C for SWNT and 200°C for CNFs [41] while by PECVD room temperature was reached . Concerning the temperature of growth and the role of the catalyst recent outcomings appeared in the literature opening new interesting perspectives. For instance, by using non-CVD techniques CNTs have been obtained at remarkably low-temperature by hydrothermal [51] and solvothermal [52] routes (MWNTs without any catalyst at 160 °C and 310 °C, respectively), using polyethylene-glycol (PEG) and an alcohol ether ($C_{12}E_4$) as carbon sources. Growth of SWNT at room temperature has been obtained also by a sonochemical route at room temperature [53]. The authors describe the results of ultrasonication of a mixed solution of ferrocene and p-xylene in the presence of silica powder at atmospheric pressure and room temperature. They report that cavitation bubbles can be produced in a liquid solution during sonication, instantaneously generating local temperature hot–spots of several thousands °C [54]. This high temperature hot spots provide the required energy to decompose ferrocene and p-xylene, so producing *in situ* the Fe catalyst and the carbon source for the CNT growth. Therefore, the actual SWNT growth is occurring at high temperature and pressure while the sonochemical process is actually carried out with the solution mixture being held at room temperature.

In the last year reports have appeared on the catalytical activity of noble metals [55,56] and silicides [57] for SWNT growth by CVD. Takagi et al have demonstrated that any metal [55], even gold, silver, and copper, can act as a catalyst for SWNT synthesis. This result shows that the first requirement for SWNT synthesis is a nanoscale catalyst metal independently from the metal, and also that the properties of the metal at low dimensional scale can change dramatically, becoming less important than the chemical nature of the catalyst. These results provide new prospective to accelerate the CNT employment in the technology. As mentioned before on the application in FETs, the possibility to nucleate CNTs on silicides is an advantage, as silicides are heavily used in metal-oxide semiconductors (CMOS) as conductors, but so far, the nucleation densities achieved have been too low [56].

We spend few lines to describe the surface–bound CVD technique used in this work, called surface bound CVD , which uses thin metal films to catalyze nanotube growth, as it offers the significant advantage of compatibility with common microelectronics fabrication techniques and consequently it is the currently used technique to study the mechanism of growth of CNT.

We present each steps of a typical surface-bound CVD process on SiO_2 substrate (the most used) by using Fe or Ni or Co as catalyst [Figure 2.11 (a)]:

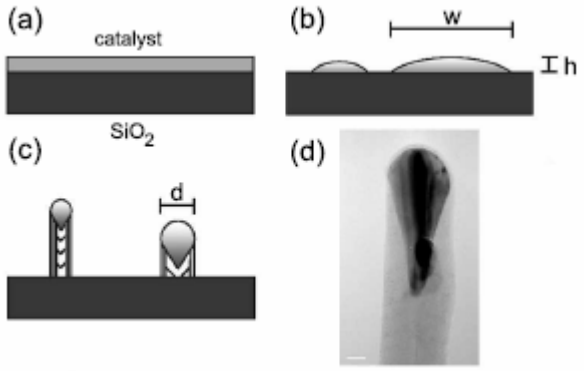

Figure 2.11*: Schematic of the nanotube growth process. The initial thin catalyst film (a) is heated up to the desired temperature and splits up into islands (for example on SiO_2 substrate) (b)nanotubes grow as the carbon precursor gas is let into the chamber (c), and a HRTEM image shows an example of a CNF grown by tip growth mechanism [58] (d, scale bar: 20 nm).*

1.Catalyst deposition (usually by sublimation from heated filaments) *ex situ or in situ* as thin film on the substrate.

2.Chemical and morphological activation of the catalyst through thermal treatment in presence of reactive or inert gases. The morphological activation consists in forming discrete catalytic nanoparticles by breaking the film into metal islands of average lateral extent *w* and height *h* [Figure 2.11(b)],due to the interplay of different mechanisms of surface energy minimization, stress release, and other factors. We will discuss these mechanisms in more detail in chapter 4, where we present the results of XPS analysis of thin films subjected to different pretreatments.

3.After the chemical-morphological activation of the surface it is required to operate in a "clean" chemical environment, that means in high vacuum conditions or in presence of carrier gasses, where the thermolysis or pyrolysis of the hydrocarbon gas precursor is obtained. The stages of the reactions can be followed by using highly sophisticated surface science tools. At this final step the nanotube growth eventually starts [Figure 2.11(c)], and the lateral size *w* of

the metal islands is generally found to dictate the nanotube diameter *d*. The metal particle found at the tip of the as-grown nanotubes undergoes heavy reshaping during growth, as confirmed by TEM imaging [58,59].

Although arc discharge, laser ablation and CVD techniques involve different temperature ranges, but analogies are evident when comparing the SWNT growth results [60,61]. For all the synthesis techniques mentioned, transition and rare-earth metals (e.g. Ni, Co, Fe, Y, La), and more efficient mixtures of them, are found to be the best elements to catalyze SWNT growth. Moreover, the morphologies of the SWNTs produced by the different techniques are very similar. In each case, SWNTs are found self-assembled in crystalline bundles, their diameters varying from 0.7 to 3 nm [60,61]. Only SWNT CVD have more probability to be found isolated. These correlations suggest that a common mechanism could explain the growth of SWNTs [62,63]. The most remarkable difference between the CVD technique and arc discharge and laser ablation techniques consist of the nucleation of many SWNTs from a single catalyst particle in case of synthesis by arc discharge and laser ablation. In these cases, CNT bundles are often found to nucleate from a single particle, often in a sea-urchin-like fashion [62] [Figure 2.12(a)]. Whereas in CVD, SWNTs are typically found to nucleate from a single catalyst particle [Figure2.12(b)].

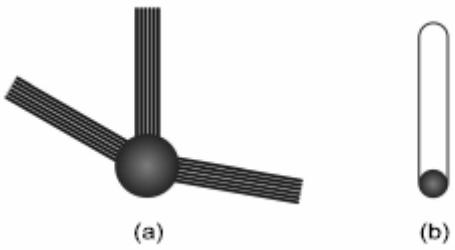

Figure 2.12 *Schematic of the SWNT growth mode in the case of (a) arc discharge/laser ablation techniques and (b) CVD techniques.*

Loiseau *et al*.[61] carried out detailed HRTEM analysis to clarify the different observed nucleation modes of SWNTs. They observe two different situations. In the first case *(arc discharge/laser ablation techniques)*, the tube growth is perpendicular to the surface of the particle where the particles are fairly large (5-20 nm), but it is rarely observed in CVD nanotubes.In this first case, the tubes are most frequently arranged in bundles, but single tubes emerging perpendicular to the surface of the particles can rarly also be observed. In such cases, the nanotube diameters are not correlated with the size of the particle. In the second

case (CVD), the growth is defined as *tangential*; the particles are generally smaller (1-5 nm), and are found to determine the SWNT diameter.

2.4 Studies on the CNT growth mechanism

First of all we want to remark that the mechanism of CNT growth is still far from a complete understanding. Such a comprehension is certainly a needed step in order to optimize the growth efficiency and ultimately could boost the actual entrance of the CNTs in the market. Hence every growth technique which is able to provide some insight on the CNT growth mechanism and on the role of the catalyst and of the carbon precursor, can provide an important impact. From this point of view, the CVD technique is particularly promising since it is compatible with a detailed chemical and morphological study of the substrate and of the catalyst after every step of the process.

In the last years this technique of growth has permitted to obtain remarkable insights, concerning the morphology, the chemical state of the catalyst. However so far enough attention has not yet been paid to the study of the chemical state of the catalyst at every step of the CVD process.

The aim of the work presented in this thesis is the systematically *in situ* investigation of the catalyst chemical state (chapter 4,5) after each step of the CVD experiment by using XPS and the correlation of these results with the morphological analysis of the surface realized *ex situ* by AFM (in chapter 4, the motivation of this work will be discussed in more details). Moreover, to understand the sequence of states that the carbon atoms go across on passing from the precursor to the CNTs, we have undertaken (see chapter 6) a real time study (by a photoemission experiment at Elettra) during the CNT growth.

Bibliography

[1] Hughes T. V. ,Chambers C. R. *US Patent* 405480 1889.

[2] Schützenberger P. and Schützenberger L., *Compt. Rend.* 111, 774 (1890).

[3] Davis W. R., Slawson R. J., Rigby G. R., *Nature* 171, 756 (1953).

[4] Baker R. T. K. and Harris P. S., *Chemistry and Physics of Carbon*, (Marcel Dekker, New York, 1978),14, p.83.

[5] Baker R. T. L. , Harris P. S., Thomas R. B., Waite R. J., *J. Catal.* 30, 86 (1973).

[6] Oberlin A., Endo M., Koyama T., *J. Cryst Growth* 32, 335 (1976).

[7] Hayashi T. et al., *Carbon* 44, 1130 (2006).

[8] De Jong K. P., Geus J. W., *Catal. Rev*. 42, 481 (2000).

[9] Brand U. J. et al., *Practical Metallography-Praktische Metallographie* 36, 406 (1999).

[10] Bernst R. et al, *Materials And Corrosion-Werkstoffe Und Korrosion* 57, 724 (2006).

[10] Toh C. H. et al., *Materials At High Temperatures* 20, 527 (2003).

[11] Iijima S., *Nature* 354, 56 (1991).

[12] Krätschmer W. et al., *Nature* 347, 354 (1990).

[13] Endo Y. and Zhao X. L. , *New Diamond Frontier Carbon Technol*. 16, 123 (2006).

[14] Journet C. , Maser W. K., Bernier P., Loiseau A., De LaChapelle M. L., Lefrant S., Deniard P., Lee R., Fischer J. E., *Nature* 388, 756 (1997).

[15] Vazquez J. , Beyers R., *Nature* 363, 605 (1993).

[16] Subramoney S., Ruoff R. S.,. Lorents D. C , Malhotra R., *Nature* 366, 637 (1993).

[17]Yu M. F., Files B. S., Arepalli S., Ruoff R. S., *Phys. Rev.Lett.* 84, 5552 (2000).

[18]Krupke R., Hennrich F., von Lohneysen H. and Kappes M.M., *Science* 301, 344 (2003).

[19] Tamir S., Drezner Y., *Appl. Surf. Sci.* 252, 4819 (2006).

[20] Scott C. D. et al., *Appl. Phys. A* 72, 573 (2001).

[21] Grobert N., *Materials Today* 10, 28 (2007).

[22] Thess A., Lee R., Nikolaev P., Dai H. J., Petit P., Robert J., Xu C. H., Lee Y. H., Kim S. G., Rinzler A. G., Colbert D. T., Scuseria G. E., Toma´nek D., Fischer J. E., Smalley R. E. *Science 273, 483* (1996).

[23] Eklund P. C., Pradhan B. K., Kim U. J., Xiong Q., Fischer J. E., Friedman A. D., Holloway B. C., Jordan K.and Smith M. W., *Nano Lett.* 2, 561 (2002).

[24] Terrones M., *International Materials Reviews* 49, 325 (2004).

[25] Hsu W. K. et al., *Chem. Phys. Lett*. 262, 161 (1996).

[26] Hsu W. K., *Nature* 377, 687 (1995).

[27] Hsu W. K. et al. , *Chem. Mater.* 11, 1747 (1999).

[28] Hsu W. K. et al. , *Chem. Phys. Lett*. 301, 159 (1999).

[29] Kuchibhatla S.V.N.T. , Karakoti A.S., Bera D., Seal S., *Progress in Materials Science* 52, 699 (2007).

[30]Lieberman M. A., Lichtenberg A. J., Principles of plasma discharges and materials processing, Wiley New York, (1999).

[31]Merkulov V. I., Melechko A. V., Guillorn M. A., Lowndes D. H., Simpson M. L., *Appl. Phys. Lett*. 79, 2970 (2001).

[32] Bower C. , Zhu W., Jin S. H. , Zhou O., *Appl. Phys. Lett* . 77, 830 (2000).

[33] Huang H. J., Kajiura H., Tsutsui S., Hirano Y., Miyakoshi M., Yamada A., Ata M., *Chem. Phys. Lett*. 343, 7 (2001).

[34] Ren Z. F., Huang Z. P., Xu J. W., Wang J. H., Bush P., Siegal M. P., Provencio P. N., *Science* 282, 1105 (1998).

[35] Chhowalla M., Teo K. B. K., Ducati C., Rupesinghe N. L., Amaratunga G. A. J., Ferrari A. C. Roy D., Robertson J., Milne W. I., *J. Appl. Phys* 90, 5308 (2001).

[36] Hirata T., Satake N., Jeong G.H., Kato T., Hatakeyama R., Motomiya K., Tohji K., *Appl. Phys. Lett*. 83, 1119 (2003).

[37] Cui H., Zhou O., Stoner B. R. J. , *J. Appl. Phys* 88, 6072 (2000).

[38] Bower C., Zhu W., Jin S. H., Zhou O., *Appl. Phys. Lett* ,77 830 (2000).

[39] Boskovic B., Stolojan V., Khan R. U. A., Haq S., Silva S. R. P., *Nature Mater.* 165, 1 (2002).

[40] Minea T., Point S., Granier A., Touzeau M., *Appl. Phys. Lett*. 85, 1244 (2004).

[41] Cantoro M., Hofmann S., Pisana S. et al., *Nano Lett.* 6, 1107 (2006).

[42] Tibbetts G.G., Bernardo C.A., Gorkiewitz D.W., Alig R.L., *Carbon* 32, 569 (1994).

[43] Tibbetts G.G., Gorkiewicz D.W., Alig R.L., *Carbon* 31, 809 (1993).

[44] Sen R., Satishkumar B. C., Govindaraj A., Harikumar K. R., Raina G., Zhang Jin-Ping, Cheetham A. K., *Chem. Phys. Lett*. 287, 671 (1998).

[45] Sen R., Govindaraj A., Rao C. N. R., *Chem. Mater*. 9, 2078 (1997).

[46] Avouris P., Chen J., *Materials Today* 9,46 (2006).

[47] Nikolaev P., Bronikowski M. J., Bradley R. K., Rohmund F., Colbert D. T., Smith K. A., Smalley R. E., *Chem. Phys. Lett.* 313, 91 (1999).

[48] Kima H. J., Hana J.H., Yanga W.S., Yooa J.B., Parkb C., Hanc I.T., Parkc Y.J., Jinc Y.W., Jungc J. E., Leec N.S.,Kimc J.M., *Materials Science and Engineering* C 16, 27 (2001).

[49] Morgen M., Ryan E. T., Zhao J. H., Hu C., Cho T. H., Ho P. S., *Annu. Rev. Mater. Sci.* 30, 645 (2000).

[50] Kong J. et al., *Science* 287, 622 (2000).

[51] Wang W. Z., Huang J. Y., Wang D. Z., Ren Z. F., *Carbon* 43, 1328 (2005).

[52] Wang W. Z., Kunwar S., Huang J. Y., Wang D. Z., Ren Z. F., *Nanotechnology* 16, 21 (2005).

[53] Jeong S. H., Ko J. H., Park J. B., Park W., *J. Am. Chem. Soc.* 126, 15982 (2004).

[54] Suslick K. S., *MRS Bull*. 20, 29 (1995).

[55] Takagi D., Homma Y., Hibino H., Suzuki S., Kobayashi Y., *Nano Lett*. 6, 2642 (2006).

[56] Nihei M., Kawabata A., Awano Y., *Jpn. J. Appl. Phys*. 42, L721 (2003).

[57] Takagi D., Hibino H., Suzuki S., Kobayashi Y., Homma Y., *Nano Lett*. 7, 2272 (2007).

[58] Ducati C., Alexandrou I., Chhowalla M., Amaratunga G. A. J., RobertsonJ*., J. Appl. Phys.* 92, 3299 (2002).

[59] Helveg S., Lopez-Cartes C., Sehested J., Hansen P. L., Clausen B. S.,Rostrup-Nielsen J. R., Abild-Pedersen F., Norskov J. K., *Nature* 427, 426 (2004).

[60] Gavillet J., Loiseau A., Journet C., Willaime F., Ducastelle F. & Charlier J. C., *Phys. Rev. Lett.* 87, 275504 (2001).

[61] Loiseau A., Gavillet J., Ducastelle F., Thibault J., Stephan O., Bernier P. & Thair S. *Compt. Rend. Phys*. 4, 975 (2003).

[62] Saito Y. Carbon 33, 979 (1995).

[63] Kataura H., Kumazawa Y., Maniwa Y., Ohtsuka Y., Sen R., Suzuki S. & Achiba, Y. *Carbon* 38, 1691 (2000).

Chapter 3

Mechanism of carbon nanotubes growth

In this chapter we present in section 3.1 a summary of the early nucleation- growth models for CNT. In section 3.2 we illustrate an overview of the general chemical and physical processes involved during nanotube growth by CVD. Then in sections 3.3 and 3.4 we report the main open points about the mechanism of growth of CNT and finally in 3.5 we present the conclusions and some recent outcomes about the nucleation and growth of CNT.

3.1 Introduction

In spite of the enormous progress in synthesis techniques, the theoretical understanding of the growth of filament form of carbon (SWCNT, MWNT, fibers) has lagged behind. Many speculation about the possible mechanisms of CNT growth are present in the literature, and nowadays there is not a unique model able to explain all the various, and often conflicting, experimental data. Actually the suggested mechanisms only match specific experimental evidences and have no generic validity. On the other hand, regarding the many possible growth situations, the *a priori* existence of only one mechanism might be unjustified. However, at least for catalytic synthesis, certain facts, such as the predominant catalytic activity of transition metals (e.g Ni, Co, Fe, Pt, Y) and rare-earth metals (e.g. La), point towards common features.

3.2 Vapour-liquid-solid (VLS) based-models for CNT nucleation and growth

Most of the existing models for the catalytic CVD growth of nanotubes are based on a mechanism formulated several years before the official CNT discovery (1991), proposed by Baker *et al.* [1] (1972), to explain the growth of carbonaceous solids with filamentary form. The mechanism proposed adopts concepts of the vapour-liquid-solid (VLS) model, introduced to explain the growth of silicon whiskers [2] in 1964 . According to Baker's mechanism, the growth is fed by chemisorption from the vapour phase. The hydrocarbon molecules decompose at the catalyst surface [Figure 3.1 (b)], and the carbon atoms diffuses down the thermal gradient to be deposited predominantly in the protected regions (not exposed to the gas) to produce the situation shown in Figure 3.1(c). The deposition of carbon at the catalyst particle is an endothermic reaction : therefore the regions where precipitation preferentially takes place will be at lowest temperature. The precipitation of carbon at the rear of the particle builds up a deposit of carbon which forces the particle away from the support. This initial mode of growth is responsible for the distortion of the liquid particle as shown in Figs. 3.1(b) and 3.1(c). The rate of carbon transport through the particle increases and consequently the filament growth rate increases. If diffusion of carbon through the particle is the rate determining step, then excess carbon from the decomposition of acetylene will be deposited at the exposed face of the particle. It is possible that the bulk material arises from carbon transported through the particle and the skin by carbon transport around its peripheral surfaces, as shown in Figure 3.1(c). Ultimately, the situation shown in figure 3.1(d) is reached where the particle is completely encapsulated by surface carbon and filament growth ceases as observed on particles which had lost their activity.

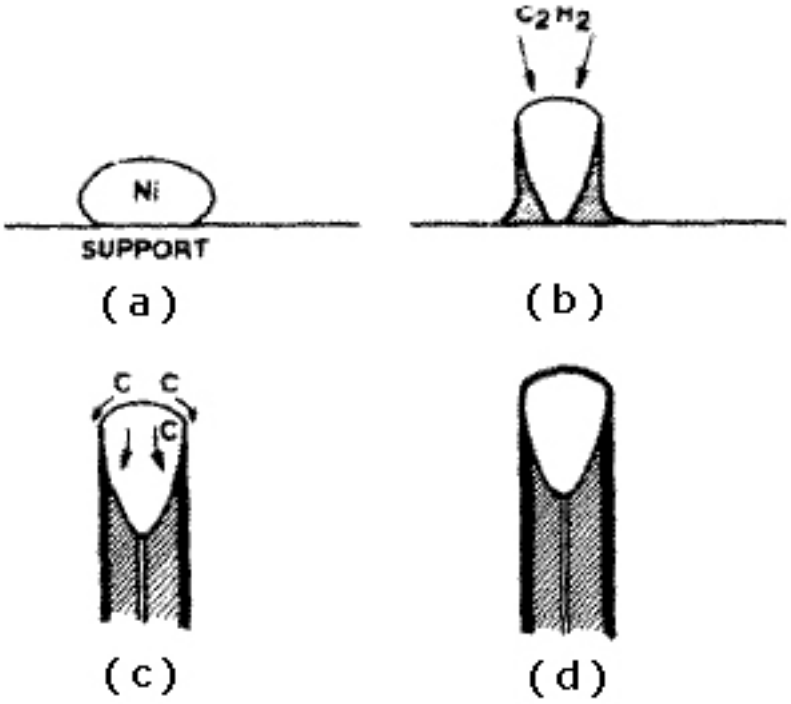

Figure 3.1 *Mechanism of carbon filament formation, in the case of tip growth mode by Baker [1].*

Another model to explain the mechanism of growth of filamentary form of carbon, which is based on the idea of VLS, was proposed by Oberlin et al. [3] in 1976. He proposed a two-step growth process. The first step is responsible for the formation of the inner nanotube core, containing long, straight and parallel carbon layers cylindrically rolled around a hollow tube. The second step consists of the thickening of the tube by a pyrolytic deposit. After the first carbon shell is formed, new hydrocarbon species dissociate on the particle surface and carbon layers develop by lateral growth following the external surface of the catalyst. Such lateral growth exerts a force strong enough to lift up the catalyst particle from the substrate.
Rostrup-Nielsen et al. [4] proposed a concentration gradient-driven mechanism to explain the diffusion of carbon through the catalyst bulk, alternative to the temperature gradient-driven process proposed by Baker et al. This assumption was further developed and studied in detail [5,6].

In the case of nanotube growth by catalytic CVD, the interaction between the metal catalyst and the supporting substrate is one of the factors influencing nanotubes growth mode. As CVD became a routinely used technique to synthesise surface-bound nanotubes, tip or base growth modes were both reported, with and without the use of plasma assistance during growth.

Base and tip growth mechanisms have been proposed, depending on the position of the catalytic particle, describing how the carbon layers form the tube body and how the metal particle interacts with the underlying substrate . Baker et al. [1,7] proposed his growth model, as presented above, based on observation that a mostly tip growth was observed for Ni-catalysed nanofibres, while a base growth for other specific deposition conditions, such as Pt-Fe/C_2H_2 systems [7]. They explained the two different observed growth mode, tip or base, attributing a crucial role to the specific interaction between the catalyst particle and the substrate [7]. Nanofibres grow with the nanoparticle at the tip (tip growth) in the case of weak catalyst-substrate interaction [Figure 3.2(a)], while the nanoparticle remains anchored to the substrate (base growth) in the case of strong catalyst-substrate interaction [Figure 3.2(b)]. Actually it is also shown by Cantoro et al [8] that the chemisorption of reducing species leads to a change in the catalyst-substrate interfacial energy and thus in the wetting of the metal on the underlying oxide. In reality, the explanation of tip/base growth is more complicated than the scenario proposed by Baker, and nowadays it seems to be a competition of different mechanisms.

Tip or base growth modes are both reported by using CVD as technique to synthesise surface-bound nanotubes. The base growth mechanism is typically observed in case of SWNTs and few-walled tubes [9-12] , while it is observed that large diameter CNFs and MWNTs grow especially by tip growth mode[13-15] rather than base growth mode [16,17]. The pressure exerted by the carbon accumulating on the bottom of the catalyst particle, while forming the graphene layers, plays a significant role. In the case of MWNTs and CNFs, the formation of multiple walls can exert enough force to lift up the particle from the substrate, regardless of the specific catalyst-substrate interaction. The same phenomenon was also observed during this thesis (see the results in chapter 6).

Figure 3.2 Schematic of (a) base and (b) tip growth modes for carbon nanotubes.

3.3 Chemical and physical processes involved during CNT growth by CVD

In the CNT growth via catalytic CVD the catalyst cluster dimension, structure and reactivity to hydrocarbon gasses play a key role to obtain the desired carbon structure (SWNT, MWNT, CNF exec). As already mentioned in the previous chapter, the best catalysts, known so far, are transition metals (Fe, Ni Co) promoting hydrocarbon decomposition, even if SWCNT synthesis has been recently obtained also by using nobel metals nanoparticles [18].

When the catalyst film is annealed during the first step of the CVD process (without hydrocarbon exposure), it breaks into islands. The islands might consist of smaller crystalline grains [5]. For wet catalyst systems, small metal clusters form after precipitation from the liquid precursor or can be predefined by chemical colloidal synthesis. The equilibrium shape of such small metal particles can be calculated based on a minimization of the surface energies for a given crystalline structure. Figure 3.3 shows the so-called Wulff construction for a catalyst cluster with an underlying face-centred-cubic (fcc) structure. Ni and Co are known to exhibit an fcc phase at given conditions [19], whereas Fe, being allotropic, exhibits a body-centred-cubic (bcc) phase (αFe), which above 912°C (at atmospheric pressure) changes to an fcc structure (γ-Fe) [20]. Geometrically, the equilibrium shape is a cuboctahedron, whereby the larger hexagonal facets have a (111) orientation and the smaller square facets have a (100) orientation. The crystal shape shows good agreement with more specific theoretical modeling for Ni [21], and experimentally observed facets in HRTEM [22]

The crystal termination by a few low-index planes might not correctly reflect the surface of larger metal clusters or particles which are part of a larger island assembly, but it does partly justify the emphasis of the (111) facet in theoretical studies.

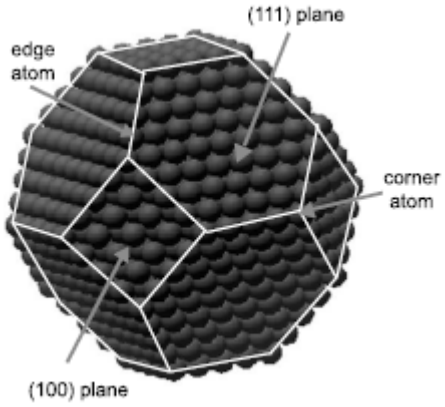

Figure 3.3 *Wulff construction for an fcc catalyst cluster. The surface area of the (111) facet is the largest, indicating its importance for surface related processes.*

An important factor for the kinetics of nanotube formation is the supply and transport of carbon to sustain growth. The adsorption and decomposition of hydrocarbons on transition metal surfaces have been studied in great detail, because of the importance of these phenomena in heterogeneous catalysis [23-29]. The importance of transition metals in graphitization has been also deeply studied. Ni was found to promote catalytic graphitization [30]. More generally, metals in the VI-VIII group can dissolve a non-graphitic form of carbon and precipitate carbon as graphite when cooled, or as a consequence of supersaturation. It was shown that C_2H_2 adsorbs molecularly on Ni(110) at 90 K, forming a re-hybridized C_2H_2 species on the surface, stable up to 270 K [31]. Heating above this temperature induces de-hydrogenation. At low temperatures (< 500 K), strong crystallographic effects have been observed on flat and stepped low-index planes of Ni [23,25,29]. The sticking coeffcients for the adsorbed carbon atoms, and the effciency in terms of carbon dissolution/segregation, depend on the specific crystallographic facet considered. We can argue that each plane contributes in a different way to the nucleation and growth of nanotubes. Schouten et al. [24] found that the sticking coefficient on the (110) facets is larger than on the (100) and the (111) facets. They also found that the diffusion-limited dissolution of carbon into the bulk of a Ni crystal from the (100) face proceeds at a rate roughly equal to the corresponding process from the (110) face.

Nanotube growth is a thermally activated process. However, there are several factors determining the energy barrier ruling the process. Depending on the specific growth conditions and the crystallographic plane considered, adsorbed carbon atoms (or dimers) can start diffusing on the catalyst surface or into the bulk. Carbon atoms can diffuse into the lattice through interstitial sites, grain boundaries, and through vacancies, if the temperature is high enough to activate them. Interstitial diffusion is a fast transport mechanism and proceeds even faster along specific crystallographic planes. The flux of carbon through the bulk of the catalyst particle depends not only on its diffusivity but also on its solubility in the catalyst lattice.

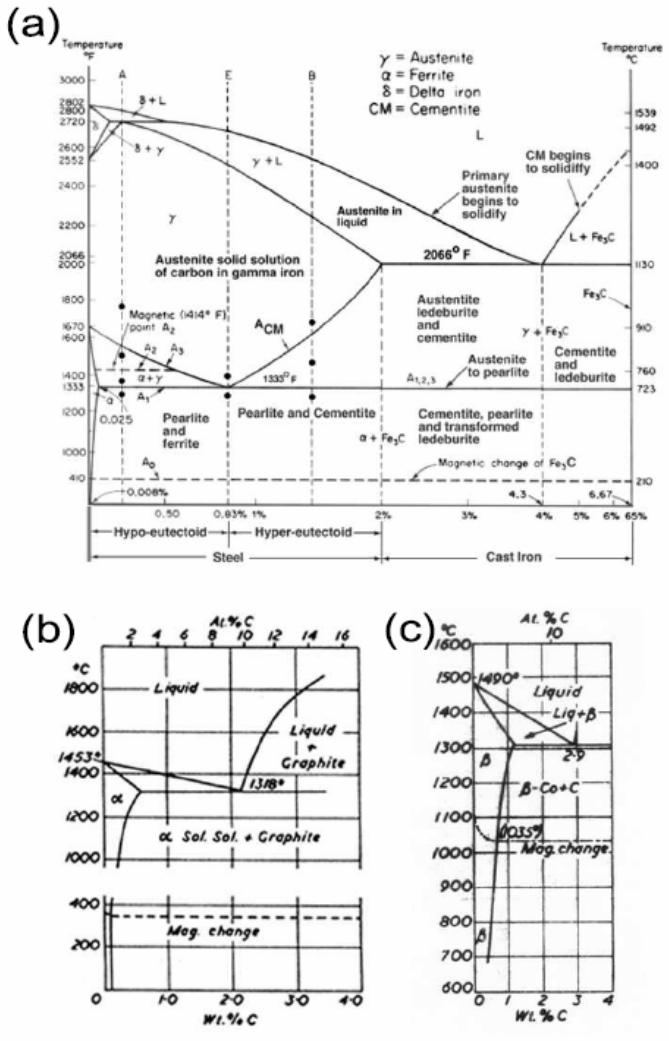

Figure 3.4 *Phase diagrams for (a) Fe-C, (b) Ni-C and (c) Co-C systems [135]. The melting temperatures of Fe, Ni and Co are 1538 °C, 1495 °C and 1455 °C, respectively. In equilibrium conditions, Ni and Co do not form stable carbides.*

As seen from the phase diagrams (Figure 3.4), the equilibrium solubility of carbon in Ni and Co is low at temperatures < 1000°C. Therefore, nanotube growth models have been suggested based on metastable carbides [32,33]. The carbon solubility can, however, be influenced by other factors, such as stress fields [34], and curvature of the metal particle. Being polycrystalline, large metal catalyst islands offer many sites for the precipitation of carbon and nanotube nucleation. At low temperatures, the solubility and diffusion coefficient of carbon are low, and hence nanotube nucleation will start first from smaller grains. These are also catalytically more active, being characterized by a higher surface-to-volume ratio.

At higher growth temperatures, the average size of the catalytic particles increases due to coalescence. Since the larger surface of the catalyst crystallites allows a larger intake of carbon atoms, and the diffusive flux of carbon through the metal becomes faster, the optimum size range is wider and nanotubes with larger diameter are formed. Helveg et al. [22] performed in-situ HRTEM experiments, where they observed thermal growth of CNTs by decomposition of CH_4 over Ni at ~ 540 °C. The initial equilibrium catalyst particle shape becomes elongated by the formation of graphene sheets at the interface layer. Such a re-shaping assists the alignment of graphene layers into a tubular structure. The elongation of the Ni catalyst crystal continues until it reaches a certain aspect ratio, before it abruptly contracts to a spherical shape (Figure 3.5). The contraction was attributed to the fact that the increase of the Ni surface energy can no longer be compensated for by the energy gained when binding the graphitic nanofibre to the Ni surface. The elongation/contraction sequence continues in a periodic manner as the nanofibre grows. Bamboo-like defects arise from detached carbon layers upon catalyst contraction. Growth stops when the graphene layers eventually encapsulate the catalyst particle completely, indicating that part of the catalyst surface must have direct contact with the gas phase.

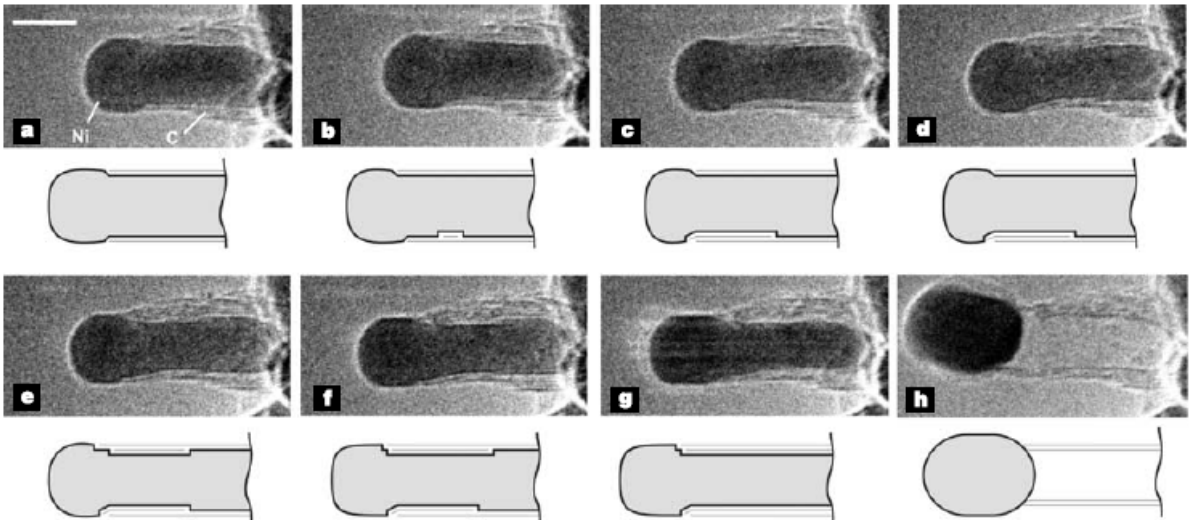

Figure 3.5 *Image sequence of a growing carbon nanofibre extracted from movie.Images a–h illustrate the elongation/contraction process. Drawings are included to guide the eye in locating the positions of mono-atomic Ni step edges at the C–Ni interface. The images are acquired in situ with CH4:H2 ¼ 1:1 at a total pressure of 2.1 mbar with the sample heated to 536 °C. All images are obtained with a rate of 2 frames* s^{-1}*. Scale bar, 5 nm.*

Monitoring the growth of nanotubes by carbon isotope labelling [35] Fan et al. showed that graphitic shells extrude from the catalyst particle and do not grow directly from the gas phase. They [35] further showed that the multi-walled structure extrudes approximately in parallel, i.e., the inner shells grow at the same rate as the outermost carbon layer. In-situ HRTEM imaging also shows that the Ni catalyst particle is solid and crystalline during growth [22]. Figures 3.4(b,c) show that neither Ni nor Co form stable carbides in bulk equilibrium conditions, and the solubility of carbon below 600 ° C is less than 0.3%. The eutectic temperature for both systems is above 1300 °C. The phase diagram for the Fe-C system [Figure 3.4(a)] is more complicated due to the carbide formation. The carbon content at the eutectic points of Ni-C and Co-C phases is approximately two times lower and the temperature is significantly higher than for the Fe-C phase. Additionally, the solidification of Ni-C and Co-C phases occurs at a relatively low concentration of carbon, at a given temperature. In the ref [36] it has been proposed that, for nm-sized particles (thus for SWNT growth), the situation is slightly different, as a size-related depression of the melting temperature for metals and carbides occurs [36-39].

Temperatures and conditions used for MWNT/CNF/SWCNT growth have been recently reported in the literature [8] where the catalyst should be in a solid state, in contrast

to the VLS model [2].The majority of previous work in the literature assumed a fixed shape and surface-to-volume ratio for the catalyzing metal, unlike the above illustrated dynamic restructuring [8,40].

For SWNTs, total energy calculations showed that the driving force for nucleation is dangling bond saturation of graphene layers during their formation [41]. Thermodynamic analysis suggests that the stage of carbon nucleation on the surface is common for all types of carbon deposits [42]. In-situ HRTEM experiments, in contrast, suggest that step edges play a key role in the nucleation and growth of graphene sheets, which, rather than deforming themselves, change the shape of the catalyst particle to give a tubular structure. A study of Ni, Co and Fe surfaces [43] showed that the (110) plane of Fe (bcc lattice) and the (111) planes of Co and Ni (fcc lattice) have the appropriate symmetry and lattice constants to overlap with the lattice of a graphene sheet. This can account for the frequent observation of graphitic planes aligned parallel to the (111) planes of the catalysing Ni particle. Many groups have observed a strong correlation between film thickness and nanotube diameter. However, we will see that this correlation is strongly related to the particular deposition conditions used. The separation of the respective roles of the catalyst surface pre-treatment and the growth stage makes this correlation weaker [5,8,10,40]. The nanotube diameter is itself correlated to the shape of the initial nanoparticle, even if a heavy reshaping occurs during growth [22] However, at fixed conditions, many groups observed that the island diameter generally dictates the maximum diameter of the growing nanotube. Figure 3.6(a) shows that, in the case of PECVD nanotubes grown from Ni and Fe catalyst films, Gupta et al. [10], and Chhowalla et al. [15] found a regular trend observing the increase of the catalyst island diameter with film thickness. The reported increase of the nanotube diameter, and decrease of nanotube length with film thickness [Figure 3.6(b)], are direct consequences. Depending on their diameter and crystalline structure, nanotubes are found to exhibit a stronger non-linearity in their growth rate as their diameter decreases. This growth saturation behaviour have been studied in more detail in [5,44].

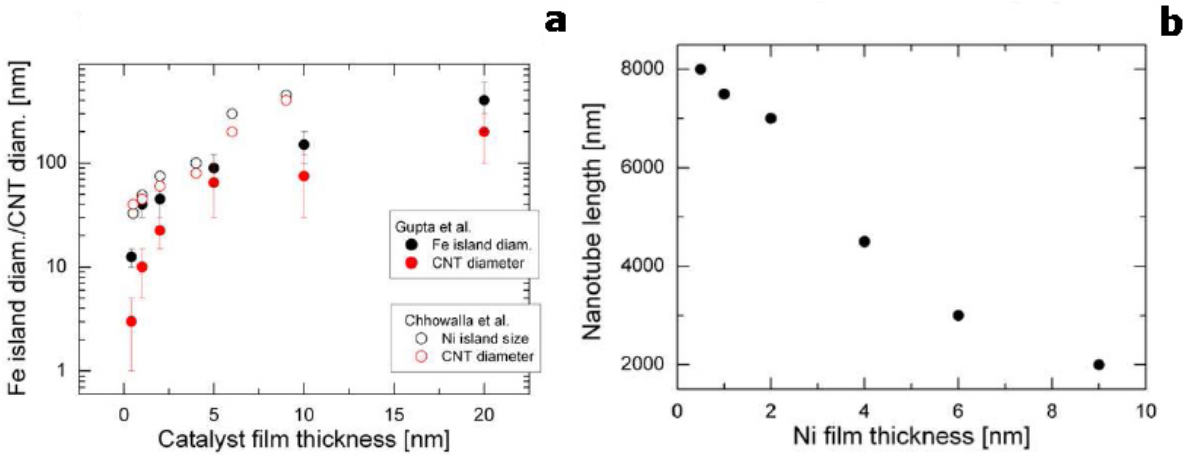

Figure 3.6 *(a) Dependence of catalyst island size and grown nanotube diameter on the original catalyst film thickness, in the case of Ni- [15] and Fe-catalysed tubes [10] grown by PECVD. (b) Dependence of nanotube length on catalyst film thickness for Ni-catalysed tubes grown by PECVD [15].*

3.4 Nowadays: surface or bulk diffusion?

The identification of the rate-determining step is of great importance in nanotube growth, as well as in crystal growth. Baker et al. [45] associated the energy of filamentary carbon growth to the activation energy of diffusion of carbon in the catalyst particle, postulating that bulk diffusion of carbon is the rate-limiting step for nanotube growth. Being a thermally activated process, carbon diffusion into or on the surface of the catalyst particle can be described by an Arrhenius-type relation: $D \propto \exp(-(E/k_BT))$, where D is the diffusion coefficient of carbon into or on the surface of the catalyst particle, E is the energy barrier for the process, and T is the temperature. The relation can be further elaborated as $\ln D \propto -E/k_BT$ and plotted linearly in a D versus 1/T plot (Arrhenius plot), with logarithmic y-scale.

Berry et al. [46] (Figure 3.7) analysed the data previously published by several authors, concerning measurements of diffusion coefficients D in bulk polycrystalline Ni in an extended temperature range (100-1000 °C) and showing in the Arrhenius plots the literature data regarding bulk diffusion of carbon onto Ni. The diffusion coefficient D spans over a 15 decades range. They neglect the data by Massaro et al. [47], as they are thought to be collected in incorrect experimental conditions. A linear fit yields activation energy of 1.5 eV.

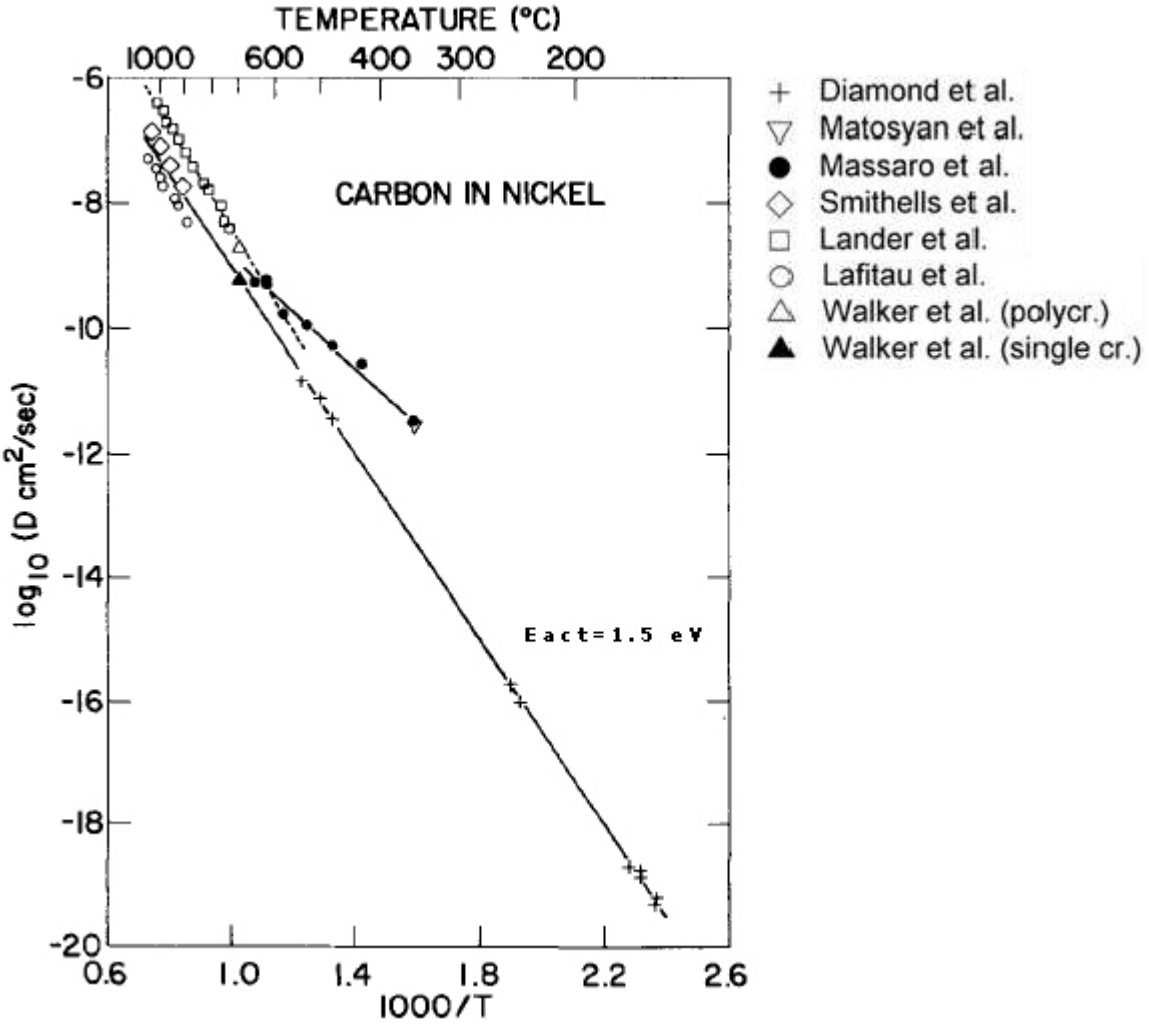

Figure 3.7 *Comparison of various studies bulk diffusion of carbon in Ni [46] by Arrhenius plots. The values for the activation energies were calculated from a linear fit of the slopes*.

Data collected by Massaro et al. [47] were initially attributed to the onset of a different diffusion mechanism, involving the carbon diffusing through the grain boundaries of the polycrystalline Ni (essentially a surface diffusion mechanism). However, they reported a value of 0.7 eV, much higher than what was correctly measured by Auger spectroscopy by Mojica et al. in 1976 [48] who estimated an activation energy of 0.3 eV for the surface diffusion of carbon onto polycrystalline Ni in the 350-425 °C temperature range. Figure 3.7 shows the Arrhenius plots for the growth rate of nanotubes grown from Ni films by thermal CVD [5] and from Ni, Co and Fe films by PECVD [49]. The activation energy for thermal CVD nanotubes is 1.2 eV [5], a value significantly close to the 1.5 eV (Figure3.7) energy value found for the bulk diffusion of carbon into Ni [46].

Hofmann et al. [49] performed density functional theory (DFT) calculations to explain the activation energies values found for PECVD-grown nanotubes (Figure 3.8). According to the Wulff construction for an fcc catalyst cluster, small metal particles reconstruct to show mainly (111) planes and, to a lower extent, (100) planes. Calculations resulted in energy barriers of about 0.5 eV, and about 2 eV for the diffusion of carbon atoms onto the Ni(111) and Ni(100) surfaces, respectively. In the case of the Ni (100) surface, a sub-surface (but not bulk) diffusion path, with 0.7 eV activation energy, can be identified. Similar results are found for Co. The calculations suggest that, once carbon atoms are available on the catalyst surface, they can grow with a very low activation energy on the (111) surface. This agrees with the results of Helveg et al. [22], who experimentally detected carbon flow on Ni (111) during thermal CNF growth and found that carbon surface diffusion over the catalyst particle seems to play a significant role. There is a significant agreement between the activation energies derived experimentally, by Hofmann et al. [49], for the nanotube growth rate of PECVD nanotubes, 0.23-0.4 eV , and the DFT calculated energies reported above. The calculated activation energy for C_2H_2 hydrogen abstraction is significantly higher than 0.5 eV on the Ni (111) surface. This explains why, to allow for the hydrogen abstraction on the catalyst surface, an extra barrier arises in pure thermal CVD growth. The plasma creates C and C-C radicals, eliminating the need for surface dissociation. Hofmann et al. [49] conclude that bulk diffusion can contribute at high temperatures, but surface diffusion is always active.

Plasma chemistry is still also a matter of controversy for carbon thin film deposition. It is known that the key effects of the plasma are a dissociation of the hydrocarbon precursor, and an etching of any amorphous carbon that may deposit on the top of the catalyst particle, thereby providing a steady supply of carbon atoms at the top surface of the catalyst particle. With respect to thermal CVD conditions, rather than assuming bulk diffusion, the observed higher activation energy of 1.2-1.5 eV for nanotube growth might also be interpreted as a cumulative effect of several contributing processes. The continuous deformation of the solid catalyst particle, showed by Helveg et al. [22] in their in-situ HRTEM measurements, indicated an interface transport mechanism of the metal, which was shown to be consistent with the suggested carbon surface transport mechanism. They proposed an activation energy of 1.2-1.5 eV, resulting from a three-step process: a breaking of the C-bond onto the Ni (111) step edge (0.7 eV), carbon incorporation under an already existing graphene sheet (0.4 eV), and diffusion at the graphene-Ni interface (0.5 eV).

In this scenario, bulk diffusion might saturate the catalyst particle, but it would not contribute to the structural growth process. However, adding up different activation energies

for non-simultaneous processes is not a correct procedure, as there is always one rate-determining step.

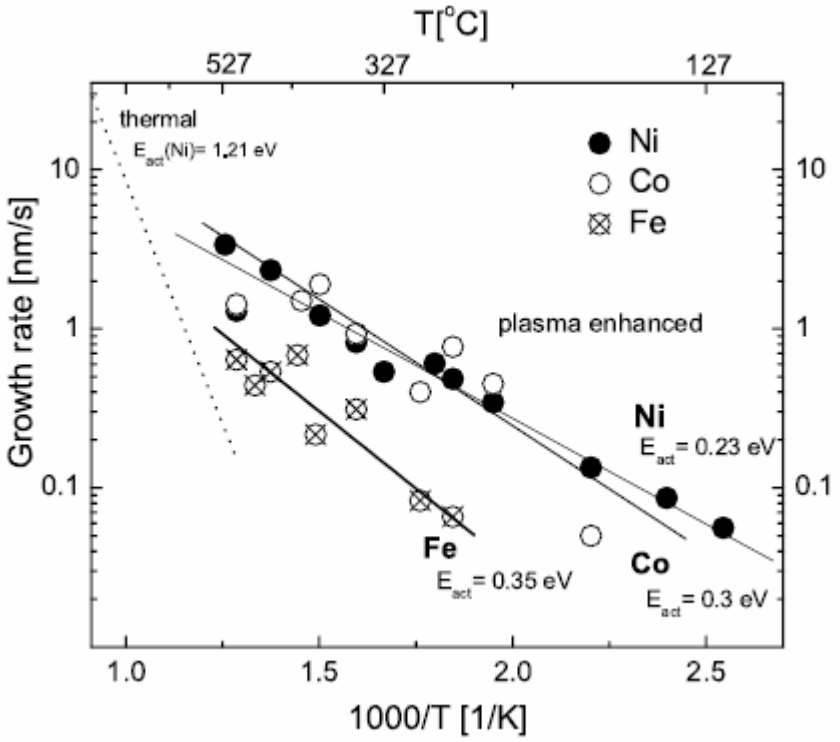

Figure 3.8 *Arrhenius plots for CNF[50] growth rates on different catalysts in NH_3 diluted C_2H_2. The activation energies are calculated from the slope of the linear fit to the data. Temperature dependent changes in the CNFs crystallinity are not considered. The dotted line is the growth rate variation for Ni thermal CVD (Eact = 1.21 eV, [5,15]).*

A surface transport mechanism for thermal growth [22] brings back the question of possible changes for a plasma excitation. Ion bombardment and the creation of strong electrostatic fields can have a significant influence on the discussed macroscopic mechanisms. This could be either beneficial, in terms of growth activation, or detrimental, considering defect formation and impurity incorporation. It has to be emphasised that most thermal growth models found in the literature assume a diffusion limited rather than a supply limited [50] reaction. However, for thermal growth, a lower pressure or temperature regime would change the balance towards a supply limit [51], whereas plasma dissociation would restore a diffusion limit.

3.5 Low Temperatures growth of SWNTs

Defect-free SWNT synthesis is generally thought to require high growth temperatures [52]. This belief arises from the success of high temperature deposition processes, such as arc discharge [53], laser ablation [54], and HiPCO [55] with local temperatures in the order of 1000-4000°C. However, we already mentioned the main motivations to lower the nanotube growth temperature, i.e. the full integration of SWCNT onto standard CMOS technology (Complemetary Metal Oxide Semiconductor), as present back-end techniques allow a maximum temperature of 450°C, the limit being set by the mechanical integrity of low dielectric constant inter-metal dielectrics [56]. Thermal CVD of good quality SWNTs at temperatures below 600°C has always been a challenge. Recently, SWNT growth has been reported at 600°C in a furnace [57] and at 550°C in both a furnace [58] and a cold-wall system [59]. In-situ HRTEM experiments show SWNT nucleation at a temperature as low as 480°C [60]. A SWNT growth temperature of 450°C has been reported for hot-wire assisted CVD [61].Remote plasmas were also successfully employed to lower the SWNT growth temperature [61-63]. Random-network FETs have been fabricated with SWNTs grown at 600°C [61] and 450°C [63] by remote PECVD. There have been recent claims of room temperature deposition of SWNTs [64,65]. However, the techniques used are not surface-bound and involve very high local temperatures of the catalyst particles, as stressed by the authors themselves, who interpret their results within the VLS model [2]. MWNTs and CNFs are often found when deviating from the optimised SWNT growth conditions or further lowering of the deposition temperature [57]. However, the high temperatures of bulk production techniques still dominate growth model considerations with the assumption that the catalyst cluster has to be liquefied and that the carbon diffusion occurs through the bulk of the catalyst cluster [50,66]. These considerations are also transferred to surface-bound CVD [67]. CNT growth below 500°C is not thought to be possible based on calculations of size-corrected melting points [68] and carbon saturation [68]. Actually, Cantoro et al.[36], reported surface-bound growth of single-wall carbon nanotubes (SWNTs) at temperatures as low as 350°C by CVD from undiluted C_2H_2. NH_3 or H_2 exposure critically facilitates the nanostructuring and activation of sub-nanometer Fe and Al/Fe/Al multilayer catalyst films prior to growth, enabling the SWNT nucleation at lower temperatures. They fund that these substrate pre-treatment and process conditions critically affect the quality of the grown

structures, resulting in a transition from SWNTs to less well-graphitised CNFs by exposure of the thin films to undiluted C_2H_2 at < 10^{-3} mbar. They showed that when Ni, Co, and Fe films above 1 nm are pre-treated in a NH_3 plasma prior to growth, the film surface is nanostructured so that CNFs are observed at temperatures as low as 200 °C, but no SWNTs are found. As mentioned above, the commonly accepted nanotube growth model constitutes a rare example of a catalytic reaction in which the rate is believed to be controlled by diffusion of carbon through the catalyst bulk from a supersaturated liquid eutectic [50,66,67,69]. This is typically related to a minimum growth temperature well above 500°C, since the size-corrected melting point of mesoscale Ni, Co and Fe catalysts cluster exceeds 500°C, even if saturated with carbon [36,37,67,68].

Low temperature growth of bamboo-like CNFs and defective MWNTs well below 400°C was reported by PECVD [69] The large catalyst cluster size of 5-100 nm allows for a small size-related melting point depression [36,37]. In fact, in-situ HRTEM showed that Ni catalyst cluster, although highly deformable, stays crystalline during CVD at 540°C [22]. This clearly shows that growth of anisotropic nanotubes can occur from a solid catalyst phase, i.e. a liquid catalyst seed is not necessary. Therefore, nowadays, there are literature data [36,49,66,68-72] which conflict the arguments that the minimum temperature for nanotube growth is at the melting point of supersaturated carbon-metal eutectics .

In the Chapter 6 we will show that the SWNT nucleation requires nm-sized catalyst clusters. The melting point of mesoscale metal clusters scales linearly with $N^{(-1/3)}$, N being the number of constituent atoms [36,37]. Iron carbide clusters appear to scale in a similar fashion [37]. An extrapolation of mesoscale pre-melting point and melting point depression into sub-nm diameter metal clusters indicates a possibility of liquefaction even at 350 °C. However, Qi et al. [37] found that such very small metal clusters prefer an icosahedral structure which leads to deviations from the above mentioned scaling, i.e. larger melting points. The smaller the metal catalyst the more dominant its surface. Therefore, by Cantoro et al. [36], independent of a definition of solid, liquid phase, or surface premelting, it can be expected that catalytic SWNT growth is governed by surface processes. Recent molecular dynamics simulations of a 1 nm-sized Fe nanoparticle show negligible carbon penetration into the catalyst bulk and that SWNT growth is fed by fast carbon diffusion on the catalyst surface [72]. No supersaturation-segregation process is necessary. Chemisorbed species such as H_2 can significantly alter a catalyst surface [73] and thus aid diffusive transport and SWNT nucleation dependent on temperature and pressure. Conceptually, they sustain that a liquid catalyst-carbon eutectic is not a necessity at low temperatures; SWNT growth is dominated by

surface processes. The findings extend to catalytic growth of anisotropic nanostructures in general [74].

3.6 Conclusion and current experimental results

As evident from the reported data, so far a unique model which can explain the various, and often conflicting, experimental data has not yet been proposed. This is because the suggested mechanisms only match specific experimental evidence and have no generic validity. On the other hand, regarding the many possible growth situations, the a priori existence of only one mechanism might be unjustified. Moreover, in the last months, several experimental results showed that SWCNT can be synthesized by using non conventional catalyst, like semiconductors and noble metals [18,75,76].

In particular, Takagi et al. [75] obtained single-walled and double-walled CNTs via CVD with ethanol in the presence of semiconductor nanoparticles of SiC, Ge, and Si. Before the growth, to remove the oxide formed on the semiconductor particles, the sample was kept in 900 °C Ar/H_2 ambient for 10 min. Then the temperature was set to 850 °C, and the CVD growth was performed by bubbling liquid ethanol using Ar/H_2 gas for 10-30 min at 5-7 10^{-2} Pa. We want to underline that the CNT synthesis with semiconductor was obtained only by using nanoparticles of 5 nm diameter or smaller.

Moreover, as already mentioned Takagi et al. [18] demonstrated that any metal, even gold, silver, and copper, can act as a catalyst for SWCNT synthesis in CVD conditions. In this case, the metal nanoparticles were deposited on SiO_2, Al-hydroxide, and sapphire and underwent heat treatment at in air at 800-950 °C, before the CVD process. After this procedure the particle diameter become smaller that 3 nm, due to the partial evaporation of nanoparticles. Actually this catalyst pre-treatment is effective for noble metals as well as for iron-family elements. This implies that potentially, any metal particle may produce SWCNTs when its size becomes 1-3 nm, and that carbon atoms can form SWCNTs in a self-assembling fashion on nanoparticles without the specific functions of iron-family elements. The crucial parameter of CNT catalyst particles seems to be a lateral dimension less than 5 nm.

Bibliography

[1]Baker R. T. K. J., *Catal.* 26, 51 (1972).

[2]Wagner R. S. and Ellis W. C., *Appl. Phys. Lett*. 4, 89 (1964).

[3]Oberlin A., Endo M. and Koyama T. *J. Cryst. Growth* 32, 335 (1976).

[4]Rostrup-Nielsen J. and Trimm, D. L. *J. Catal*. 28, 155 (1977).

[5] Ducati C., Alexandrou I., Chhowalla M., Amaratunga G. A. J. and Robertson J., *J. Appl. Phys.* 92, 3299 (2002).

[6] Klinke C., Bonard J. M. and Kern, K. *AIP Conf. Proc*. 685, 447 (2003).

[7]Baker R. T. K., and Waite, R. J. *J. Catal*. 37, 101 (1975).

[8] Cantoro M., Hofmann S., Pisana S., Ducati C., Parvez A., Ferrari A., J. Robertson, *Diamond Relat*. *Mater.* 15, 1029 (2006).

[9]Fan S. S., Chapline M. G., Franklin N. R., Tombler T. W., Cassell A. M.and Dai, H. J. *Science* 283, 512 (1999).

[10] Wang Y. Y., Gupta S. and Nemanich R. J., *Appl. Phys. Lett*. 85, 2601(2004).

[11]Kim D. H., Jang H. S., Kim C. D., Cho D. S., Yang H. S., Kang H. D., Min B. K. and Lee H. R. *Nano Lett.* 3, 863 (2003).

[12] Morjan R. E., Maltsev V., Nerushev O., Yao Y., Falk L. K. L. and Campbell E. E. B. *Chem. Phys*. *Lett.* 383, 385 (2004).

[13]Ren Z. F., Huang Z. P., Xu, J. W., Wang J. H., Bush P., Siegal M. P. and Provencio P. N., *Science* 282, 1105 (1998).

[14]Merkulov V. I., Lowndes D. H., Wei Y. Y., Eres G. and Voelkl E., *Appl. Phys. Lett*. 76, 3555 (2000).

[15] Chhowalla M., Teo K. B. K., Ducati C., Rupesinghe N. L., Amaratunga G. A. J., Ferrari A. C., Roy D., Robertson J. , and Milne W. I., *J. Appl. Phys*. 90, 5308 (2001).

[16]Bower C., Zhou O., Zhu W.,Werder D. J. and Jin S. H., *Appl. Phys. Lett*. 77, 2767 (2000).

[17]Kim D. H., Jang H. S., Kim C. D., Cho D. S., Yang H. S., Kang H. D., Min B. K. and Lee H. R. *Nano Lett.* 3, 863 (2003).

[18] Takagi D., Homma Y., Hibino H., Suzuki S., and Y.Kobayashi , *Nano. Lett.* 7, 2642 (2006).

[19]Moruzzi V. L., Marcus P. M., Schwarz K. and Mohn P. *Phys. Rev. B* 34, 1784 (1986).

[20]Biedermann A., Tscheliessnig R., Schmid M. and Varga P., *Phys. Rev. Lett*.87, 86103 (2001).

[21]Hong S. L., Shin Y. H. and Ihm J., *Jpn. J. Appl. Phys*. 41, 6142 (2002).

[22]Helveg S., Lopez-Cartes C., Sehested J., Hansen P. L., Clausen B. S., Rostrup-Nielsen J. R., Abild-Pedersen F. and Norskov J. K., *Nature* 427, 426 (2004).

[23]Lehwald S. and Ibach H., *Surf. Sci*. 89, 425 (1979).

[24]Schouten F. C., Gijzeman O. L. J. and Bootsma G. A., *Surf. Sci*. 87, 1 (1979).

[25]Demuth J. E., *Surf. Sci.* 93, 127 (1980).

[26]Felter T. E. and Weinberg W. H., *Surf. Sci*. 103, 265 (1981).

[27]Audier M., Oberlin A. and Coulon M., *J. Cryst. Growth* 55, 549 (1981).

[28] Zaera F. and Hall R. B., *J. Phys. Chem*. 91, 4318 (1987).

[29] Vattuone L., Yeo Y. Y., Kose R. and King D. A., *Surf. Sci*. 447, 1 (2000).

[30]Derbyshire F. J., Presland A. E. B., and Trimm D. L., *Carbon* 13, 111 (1975).

[31]Zaera F., and Hall R. B., *J. Phys. Chem*. 91, 4318 (1987).

[32]Kock A., Debokx P. K., Boellaard E., Klop W. and Geus J. W., *J. Catal.* 96, 468 (1985).

[33]Alstrup I., *J. Catal.* 109, 241 (1988).

[34]Tersoff J., *Phys. Rev. Lett*. 74, 5080 (1995).

[35]Fan S. S., Liu L. and Liu M., *Nanotechnology* 14, 1118 (2003).

[36] Cantoro M., Hofmann S., Pisana S., Scardaci V., Parvez A., Ducati C., Ferrari A. C., Blackburn A. M., Wang K. Y., and Robertson J., *Nano Lett.* 6, 1107 (2006).

[37]Qi, Y., Cagin, T., Johnson, W. L. and Goddard, W. A. J. Chem. Phys. 115,385 (2001).

[38] Ding F., Bolton K. and Rosen A., *J. Vac. Sci. Technol*. *A* 22, 1471 (2004).

[39] Harutyunyan A. R., Mora E., Tokune T. ,Bolton K., Rosén A., Jiang A., Awasthi N, and Curtarolo S., *Appl.Phys.Lett*. 90, 163120 (2007).

[40] Pisana S., Cantoro M., Parvez A., Hofmann S., Ferrari A. C., and Robertson J., *Phys. E* 37, 1 (2006).

[41] Fan X., Buczko R., Puretzky A. A., Geohegan D. B., Howe J. Y., Pantelides S. T. and Pennycook S. J., *Phys. Rev. Lett*. 90, 145501 (2003).

[42]Kuznetsov V. L., Usoltseva A. N., Chuvilin A. L., Obraztsova E. D. and Bonard J. M., *Phys. Rev. B* 6423, 235401 (2001).

[43]Vinciguerra V., Buonocore F., Panzera G. and Occhipinti L., *Nanotechnology* 14, 655 (2003)

[44] Hofmann S., Cantoro M., Kleinsorge B., Casiraghi C., Parvez A., Ducati C., and Robertson J., *J. Appl. Phys*. 98, 34308 (2005).

[45] Baker R. T. K., *Carbon* 27, 315 (1989)

[46]Berry B. S., *J. Appl. Phys*. 44, 3792 (1973).

[47]Massaro T. A. and Petersen E. E. *J. Appl. Phys*. 42, 5534 (1971).

[48]Mojica J. F., and Levenson L. L., *Surf. Sci.* 59, 447 (1976).

[49] Hofmann S., Csanyi G., Ferrari A. C., Payne M. C. and Robertson J., *Phys. Rev. Lett*. 95, 036101 (2005).

[50]Kanzow H. and Ding A., *Phys. Rev. B* 60, 11180 (1999).

[51]Hafner J. H., Bronikowski M. J., Azamian B. R., Nikolaev P., Rinzler A. G., Colbert D. T., Smith K. A. and Smalley R. E., *Chem. Phys. Lett*. 296, 195(1998).

[52]Dresselhaus M. S., Dresselhaus G. and Avouris, P. (eds.) Carbon Nanotubes:Synthesis, Structure, Properties and Applications, vol. 80 of *Top. Appl. Phys*.(Springer, New York, 2001).

[53]Iijima S. Nature 354, 56 (1991).

[54]Thess A., Lee R., Nikolaev P., Dai H. J., Petit P., Robert J., Xu C. H., Lee Y. H., Kim S. G., Rinzler A. G., Colbert D. T., Scuseria G. E., Tomanek D., Fischer J. E., and Smalley R. E., *Science* 273, 483 (1996).

[55]Dai H. J., Rinzler A. G., Nikolaev P., Thess A., Colbert D. T., and Smalley R. E., *Chem. Phys. Lett*. 260, 471 (1996).

[56]Morgen M., Ryan E. T., Zhao J. H., Hu C., Cho T. H. and Ho P. S., *Annu. Rev. Mater. Sci.* 30, 645 (2000)

[57]Seidel R., Duesberg G. S., Unger E., Graham A. P., Liebau M. and Kreupl F., *J. Phys. Chem. B* 108, 1888 (2004).

[58]Maruyama S., Kojima R., Miyauchi Y., Chiashi S. and Kohno M., *Chem. Phys. Lett*. 360, 229 (2002).

[59]Liao H. W. and Hafner J. H. J., *Phys. Chem. B* 108, 6941 (2004).

[60] Sharma R., Rez P., Treacy M. M. J. and Stuart S. J. J., *Electron Microsc*. 54, 231 (2005).

[61]Mahan A. H., Alleman J. L., Heben M. J., Parilla P. A., Jones K. M. and Dillon A. C., *Appl. Phys. Lett.* 81, 4061 (2002).

[62]Li Y. M., Mann D., Rolandi M., Kim W., Ural A., Hung S., Javey A., Cao J., Wang D. W., Yenilmez E., Wang Q., Gibbons J. F., Nishi Y. and Dai H. J., *Nano Lett.* 4, 317 (2004).

[63]Zhong G. F., Iwasaki T., Honda K., Furukawa Y., Ohdomari I. and Kawarada H., *Jpn. J. Appl. Phys*. 44, 1558 (2005).

[64] Min Y. S., Bae E. J., Oh B. S., Kang D. and Park W. , *J. Am. Chem. Soc*.127, 12498 (2005).

[65]Jeong S. H., Ko, J. H., Park, J. B. and Park W., *J. Am. Chem. Soc*. 126, 15982 (2004).

[66] Rummeli M. H., Borowiak-Palen E., Gemming T., Pichler T., Knupfer M., Kalbac M., Dunsch L., Jost O., Silva S. R. P., Pompe W. and Buchner B., *Nano Lett.* 5, 1209 (2005).

[67] Gavillet J., Loiseau A., Journet C., Willaime F., Ducastelle F. and Charlier J. C., *Phys. Rev. Lett.* 8727, 275504 (2001).

[68]Harutyunyan A. R., Tokune T. and Mora E., *Appl. Phys. Lett*. 87, 051919 (2005).

[69]Klinke C., Bonard J. M. and Kern K. *Phys. Rev. B* 71, 035403 (2005).

[70]Baker R. T. L. and Barber M. A., The formation of filamentous carbon, vol. 14 of Chemistry and physics of carbon (Dekker, New York, 1978).

[71] Chen M., Chen C. M., Shi S. C. and Chen C. F., *Jpn. J. Appl. Phys*. 42, 614(2003)

[72]Raty J. Y., Gygi F. and Galli G., *Phys. Rev. Lett*. 95, 096103 (2005).

[73]Paal Z. and Menon P. G., Hydrogen Effects in Catalysis (Dekker, New York,1988

[74]Colli A., Hofmann S., Ferrari A. C., Ducati C., Martelli F., Rubini S., Cabrini S., Franciosi A., Robertson J., *Appl. Phys. Lett*.,86, 153103 (2005).

[75] Takagi D., Hibino H., Suzuki S., Kobayashi Y., and Homma Y., *Nano. Lett.*, 7, 2271 (2007).

[76] Pisana S., Jungen A., Zhang C., Blackburn A.M., Sharma R., Cervantes-Sodi F., Stampfer C., Ducati C., Ferrari A.C., Hierold C., Robertson J., Hofmann S., *J. Phys. Chem. C,* 111, 17249 (2007).

Chapter 4

Chemical and structural characterization of Fe layer on different substrates

This chapter will report the results of the study of the chemical interaction between the Fe catalyst and the substrates generally used for CNT growth, e.g. SiO_2 and Al_2O_3, and highly ordered pyrolytic graphite (HOPG). The goal is to understand how the choice of a particular substrate, or a particular catalyst treatment, can influence the size-distribution of the catalyst NPs, affecting, as a consequence, the growth of CNT via CVD. The chapter is divided into two parts, the first (section 4.1) describes Fe interaction on the oxidic substrates, i.e. SiO_2 and Al_2O_3, while the second (section 4.2) on HOPG. Two short forewords are reported before our experimental data, giving a brief overview on the mechanisms occurring during metal film deposition on oxides (subsection 4.1.1) and HOPG (subsection 4.2.1). Finally a short summary and our conclusions are presented (section 4.3).

4.1 Fe deposition on SiO_2 and Al_2O_3 surfaces

4.1.1 Mechanisms occurring during metal film deposition on oxides

Oxide-supported metal particles and films are used extensively in heterogeneous catalysis, as well as in a whole range of other technological applications. The nature of the metal-oxide interface has been widely studied and a number of review articles has been published [1-3]. When depositing a thin metal film onto an oxide substrate, we might wonder what bulk phase should form at equilibrium, in the absence of kinetic constraints [1,2,]. This depends on the relative thermodynamic stability of the various oxides and intermetallic

compounds that might form. If a metal *A* is deposited onto an oxide *BO*, then *A* could reduce the surface of *BO* to metallic *B* and itself become oxidised to *AO* if the reaction (*s* stands for solid phase)

$A(s) + BO(s) \leftrightarrow AO(s) + B(s)$

results in a negative total free energy change. Neglecting differences in formation entropies of the oxides, which are usually almost negligible, this occurs when the standard heat of formation of the AO is more negative than that of BO. Note that the late transition metals have the least stable oxides, and therefore the lowest affinity for oxygen. The affinity of transition metals for oxygen generally decreases from left to right across the periodic table.

If the two metals form stable intermetallic compounds, then one must also consider whether reactions such as

$2A(s) + BO(s) \leftrightarrow AO(s) + AB(s)$

are thermodynamically downhill. This often occurs when depositing metals with very stable oxides onto alumina or when depositing Al onto oxides, since metal-Al compounds tend to be very stable.

Passing now to the growth morphology, the wetting behaviour of a metal film on an oxide is essentially the capability of the metal to form, at equilibrium, a continuous film on the oxide (i.e. wetting the oxide) or to form metal particles on the oxide surface. These particles are characterized by some measurable contact angle θ between the metal-vacuum interface and the metal-oxide interface (see Figure 4.1). The full wetting condition of a metal onto an oxide is defined as the situation where the contact angle θ equals zero.

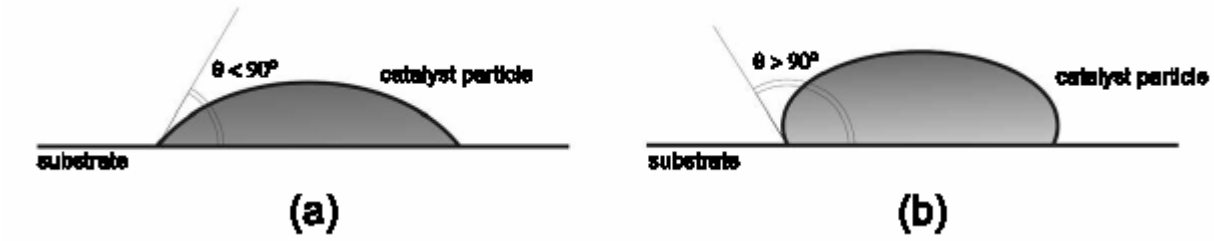

Figure 4.1 *Schematic of the wetting behaviour of metal onto a substrate. The contact angle θ between the metal-vacuum interface and the metal-oxide interface is indicated in the case of (a) good wetting (0 < θ < 90°) and (b) poor wetting (90° < θ < 180°).*

We can still define a good wetting behaviour of the metal onto the oxide when θ has values between 0 and 90° [Figure 4.1(a)], whereas we observe poor wetting when 90 < θ < 180° [Figure 4.1 (b)].

The wetting is a consequence of the balance between the metal-oxide interfacial free energy, $\gamma_{m/ox}$, the surface energy of the oxide in vacuum, $\gamma_{v/ox}$, and that of the metal, $\gamma_{v/m}$. The metal fully wets the oxide when $\gamma_{v/ox} \geq \gamma_{v/m} + \gamma_{m/ox}$. In this case, a continuous metal film is formed whose thickness is simply related to the volume of metal deposited. If $\gamma_{v/ox} < \gamma_{v/m} + \gamma_{m/ox}$, then the metal does not wet the oxide-vacuum interface. In this case, the metal will form thicker 3D particles and leave regions of oxide surface in between. The interfacial free energy, $\gamma_{m/ox}$, includes any metal oxide bonding as well as the bonding involved in any interfacial layers that are formed where, for example, the metal may be partially oxidised. Interfacial energies γ are positive, and good bonding between the phases at the metal-oxide interface would lead to small positive values of $\gamma_{m/ox}$. Since the surface free energy of metals is usually larger than, or comparable to, that of oxides, it means that the metal-oxide interfacial free energy must be very small, or there must be good bonding at the metal-oxide interface, for wetting to occur. Experiments show that mid- to late-transition metals do not wet oxide surfaces (such as silica and alumina) in their liquid state, and contact angles of ~ 100° are generally found.

Even though wetting is not thermodynamically allowed for mid- to late-transition metals, this does not mean that a monolayer of metal, perhaps in oxidised form, might not form before the 3-D particles grow. This is called the Stranski-Krastanov growth mode. If 3D particles form without this intermediate monolayer, we fall in the Volmer-Weber growth case. Contact angle measurements usually do not distinguish between these two modes. Surface science measurements have proven a Volmer-Weber mode in many cases of transition metals on oxides, but data have been reported where either a Stranski-Krastanov mode or a layer-by-layer growth mode (Frank-van der Merve mode) at room temperature (RT) and below can occur. This must be a metastable condition for the mid-to-late transition metals, since the first monolayer irreversibly turns into 3-D particles when annealed. Thus, the layer-by-layer growth at low temperatures must be due to kinetic effects associated with deposition dynamics. In fact, the strength of metal-metal bonds is much greater than metal-oxide bonds, so energetically the film should grow in 3D from the onset. However, peculiar kinetic conditions can drive the early growth to 2D islands. The transition between the 2D and 3D growth, which occurs over a narrow range of coverages near the critical coverage, can be measured directly using surface sensitive techniques.The adhesion energy $E_{adh} = \gamma_{v/m} + \gamma_{v/ox} - \gamma_{m/ox}$ is defined as the work needed to separate the metal-oxide interface, in vacuum. Therefore, another way of specifying the thermodynamic criterion for wetting is simply that, if wetting occurs at equilibrium, $E_{adh} \geq 2\gamma_{v/m}$. If $E_{adh} < 2\gamma_{v/m}$, then wetting does not

occur and particles of metal are instead expected to form on the oxide surface. The adhesion energies are determined by the strength of local chemical bonds formed at the interface, both metal-oxygen and metal-metal. For example, Ni, Co and Fe grow on SiO_2 in a Volmer-Weber mode, since the heat of formation of their oxides (-122 to -98 kJ/g_{at}: for Ni, -120 to -126 kJ/g_{at}: for Co and -133 to -165 kJ/g_{at}: for Fe) are higher than that of SiO_2 (-287 kJ/g_{at}:), and ultrathin layers will consist of isolated islands [4]. In addition, it should be remarked that the presence of gases can influence the wetting thermodynamics and kinetics of the metal deposit by altering the corresponding interfacial free energies ($\gamma_{g/ox}$ and $\gamma_{g/m}$).

Let us now pass to the catalytic properties and to the chemisorption properties of the metal deposit: many studies have demonstrated that they depend on the thickness of the film and its morphology. As discussed above, the metal film will sometimes grow in the form of islands. When these islands are only one atom thick (i.e. below the critical coverage), all the metallic chemisorption sites in the island are bonded to the oxide lattice below, whereas on thicker islands most of these sites are offered by metal atoms which themselves are bonded to other metal atoms. 2D metal islands (i.e. flat islands with large terraces) present a chemisorption behaviour (activation energies for the desorption and dissociation of adsorbed molecules) similar to the one peculiar of the low-index bulk metal surfaces (large terraces and highly coordinatively unsaturated surface sites). When the 2D islands are very thin, the chemisorption properties can be enhanced by the low effective coordination of the metal adatoms arising from the weaker bonding to the oxide lattice below, and by the limited particle size.

One very important point is related to the intrinsic stability of the metal particles. This is a general issue of Nanoscience and Nanotechnology: when an array of metal particles is heated, the mobility of its atoms will increase, the islands will coarsen and coalesce by the well known Ostwald ripening or surface migration phenomena. This is driven by a complex thermally activated mechanism that minimises surface energy and/or the free energy of the substrate-metal interface [5-8]. These phenomena are sustained by surface and interfacial diffusion, favoured also by stresses within the interface and differences between the thermal expansion coefficients of the film and substrate [9]. Annealing at progressively higher temperatures results in an increase of the surface roughness and in the formation of large, isolated islands, at the expense of smaller close-packed islands. As the temperature raises, diffusion across the substrate allows mass transport of individual metal atoms. This mechanism is strongly dependent on the type of metal, the type of substrate and the annealing environment. The temperature at which metal atoms become mobile and coarsening effects

become measurable may be significantly lower than the bulk melting temperature. As a rule of thumb, the Tamman and Huettig temperatures are defined as 0.5 and 0.3 times the melting temperature (in K), and represent the temperatures at which the atoms become mobile in the bulk and at defects, respectively [10]. As an example, coarsening effects for Fe (T_{melt}= 1538 °C) can occur at temperature as low as 461 °C. This temperature can be even lower depending on the substrate interactions, size-corrected melting points and the annealing atmosphere [11-13].

4.1.2 Fe on Al_2O_3 and SiO_2 surfaces: *in situ* XPS analysis of catalyst-substrate chemical interaction and *ex situ* characterization of catalyst/substrate morphology

Fe films (of formal thickness from <0.1nm up to 0.8nm) were deposited on Al_2O_3 and on SiO_2 surfaces at RT, in an UHV experimental apparatus (base pressure ≈$2x10^{-10}$mbar), using an evaporation rate of ≈ 0.1nm/h. We measured the Fe 2*p* photoemission spectra on the as deposited films, after annealing in UHV at 580°C (temperature of CNT growth) for 5min, and at the end of CVD process (data presented in chapter 5).

Iron formal thickness was calculated from the attenuation of the substrate photoemission peaks (Al 2*p* and Si 2*p* for Al_2O_3 and SiO_2, respectively) as a consequence of increasing Fe coverage, using the formula:

$d=\lambda \exp(-I/I_0)$

where λ is the electron inelastic attenuation length in iron at the kinetic energy of the emitted photoelectrons, and I/I_0 is the ratio between the intensity of the substrates photoemission peaks measured, respectively, after and before Fe deposition (all spectra are collected in normal emission geometry, as detailed below). In the case of deposition on SiO_2, we calculated the attenuation of the Si 2*p* photoemission peak, while in the case of deposition on Al_2O_3, the attenuation of Al 2*p*. We used the λ factor derived by the average value reported from Gries and Tanuma Rowell andPen (from optical data and formula predictive) which are, for our Si 2*p* and Al 2*p* peaks, 1.809 nm and 1.842 nm, respectively. We note that the formula reported above is correctly used to determine the thickness of a continuous film growing in layer-by-layer mode (Frank-van der Merve mode), and in our case it can only give a rough estimate of the actual film thickness. Actually, Ref. [14] observed that Fe deposited at RT on Al_2O_3, using an evaporation rate similar to ours, grows in a simultaneous multilayer (SM)

mode rather than a layer-by-layer mode. In such SM growth mode, Fe condensates in layers growing before the underlying layers are completely formed, and the film therefore consists of a terraced rough structure [15]. As already mentioned in the previous section, Fe grows on SiO_2 by a 3D Volmer-Weber mode, since the heat of formation of its oxides (-133 to -165 kJ/g_{at}: for Fe) is higher than that of SiO_2 (-287 kJ/g_{at}:), and therefore ultrathin deposits will consist of a series of isolated 3D islands [4]. As a result, in both cases herein investigated the Fe thickness determined by the above formula is to be only considered as a rough estimate of the actual physical values (accurate STM calibrations would be needed to give physically significant numbers). Figure 4.2(a),(b) compares the Fe 2*p* photoemission spectra obtained on the two substrates after the deposition at RT of different Fe thickness. All spectra have been measured in normal emission geometry, and have been normalized to the photon flux. It is clear that on the Al_2O_3 substrate, the Fe 2*p* photoemission line shows different components [Figure 4.2 (a)], whose relative intensity depends on Fe thickness, while on SiO_2 [Figure 4.2 (b)] only one component is always present, which correspond to metallic Fe (binding energy, BE, 707.3 and 720.4eV for Fe $2p_{3/2}$ and $2p_{1/2}$, respectively [16,17]).The extra peaks at 711.3 and 710.5 eV, more evident in the low coverage spectrum of Figure 4.2 (a), are due to the contribution of different Fe oxidized states, Fe^{2+} and Fe^{3+} , whose Fe $2p_{3/2}$ BEs are, respectively, 709.8 and 711 eV [18,19]. We note that the relative intensity between the non-oxidized and oxidized peaks increase up to ~0.3 nm and after that it decreases as a function of the Fe coverage [Figure 4.2(a)]. For coverage higher than ~ 0.6 nm only the features relative to metallic iron are observed [Figure 4.2 (a)]. No Al reduction or formation of metallic Fe-Al species can be argued as the Al 2*p* peak remains unvaried throughout the entire Fe deposition process [20]. The formation of iron oxide is indicative of a chemical reaction at the interface between the evaporated Fe and the Al_2O_3 substrate, while the observation that only metallic Fe is present on the surface also at low coverage on SiO_2 is an indication that in this case the interaction is weak. In the case of Fe/Al_2O_3, we monitored, together with Al 2*p* and Fe 2*p*, also the Oxygen 1*s* signal and Silicon 2*p* signals, (we remember that the Al_2O_3 films were grown on SiO_2 films, see experimental details in the appendix Appendix A2.1). The oxygen signal, detected on the substrate before Fe deposition, includes two components, one belonging to Al_2O_3 film and the other to the underlying SiO_2 substrate. For this reason it was difficult to extract information about the third weak component of oxygen, which is expected to originate from Fe oxidation [21,22]. In the case of Fe/SiO_2, we monitored the Si 2*p*, Fe 2*p*, and O 1*s* signals.

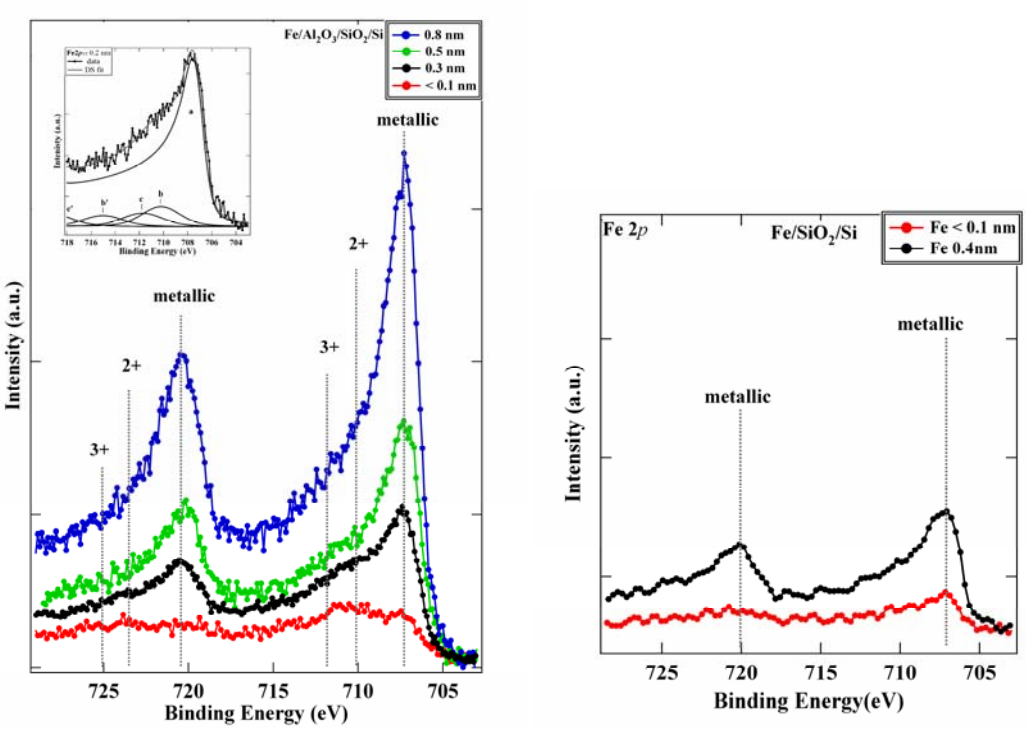

Figure 4.2 *Fe 2p photoemission spectra (hv=1253.6eV) of: (a) Fe films deposited on $Al_2O_3/SiO_2/Si$ at RT in UHV of different thickness <0.1nm (red line), 0.3nm (black line), 0.5nm (green line), 0.8nm (blue line); (b) Fe films deposited on SiO_2/Si at RT in UHV of different thickness, <0.1nm (red line) and 0.3nm (black line). All spectra are normalized to the photon flux and measured in normal emission geometry.*

Fe oxidation at the Fe/Al_2O_3 interface and no Al reduction are in accord to previous XPS [14] and Auger Electron Spectroscopy (AES) [23] results. In addition, a theoretical study by Johnson and Pepper [24] about the interfaces occurring between Al_2O_3 and some transition metals (Ag, Cu, Ni and Fe), using the molecular orbital approach, predicts and characterizes the interaction between the d orbitals of the transition metals and the p orbitals of the O^{2-} anions belonging to the Al_2O_3 top surface (the interaction between the Al ions and the deposited transition metal is not taken into account). As a consequence, charge transfer from Fe to surface O atoms should take place, ruling out re-hybridization of Fe and Al orbitals (Fe-Al bond formation). In addition, we can confidently exclude the formation of the $FeAl_2O_4$ alloy at the interface, because it has been observed only after annealing at temperature higher than 1122°C in low vacuum/air conditions [25-27].

After UHV annealing at 580°C, which is the temperature used in the CVD process for CNT growth, some changes occurs in the Fe 2*p* XPS spectra on both substrates. Figure 4.3 (a), (b) show, respectively, the XPS spectra of the Fe 2*p* doublet measured on a 0.3 nm-thick Fe film grown on Al_2O_3 and on a 0.5 nm-thick Fe film grown on SiO_2 at RT (red) and after

annealing at 580°C (black). The Fe 2*p* spectra of samples annealed in the temperature range 550-630°C present the same features observed at 580°C (data not shown).

Looking to the spectra collected on the Al_2O_3 substrate [Figure 4.3 (a)], the first noticeable observation is the disappearance of the Fe^{2+} component and slight increase of photoemission intensity in correspondence to the Fe^{3+} BE.

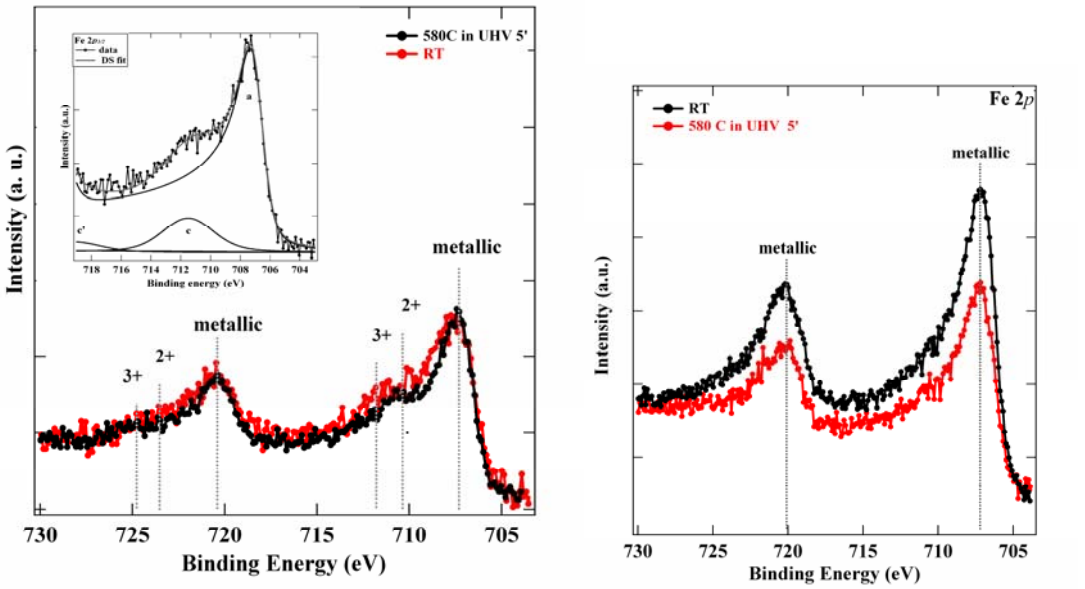

Figure 4.3 *Photoemission spectra (hv=1253.6eV) of the Fe 2p doublet of a 0.3 nm-thick Fe film deposited on Al_2O_3 (a) and of a 0.5 nm-thick Fe film deposited on SiO_2 (b) at RT (red lines) and after annealing for 5min. at 580°C (black lines). The films were deposited and annealed in UHV conditions. All spectra are normalized to the photon flux and measured in normal emission geometry. The inset in (a) shows the result of the fit performed on the annealed film deposited on Al_2O_3. (see text for more details).*

However the total area of the Fe 2*p* spectrum remains almost the same, before and after the annealing. This is a first indication that a noteworthy coalescence phenomena of Fe does not occur on Al_2O_3. On SiO_2 substrate [Figure 4.3 (b)], after the annealing at 580°C, the area under the Fe 2*p* curve decreases of ≈35%, but the lineshape does not change significantly, and no Fe^{2+} and Fe^{3+} peaks contributions are detected either before or after the annealing. This behaviour suggests the occurrence of Fe coalescence into islands on SiO_2, as confirmed also by AFM characterization, as we will see below [Figure 4.4 (b), (d)]. As already mentioned, the Fe 2*p* lineshape changes after annealing at 580°C on Al_2O_3. To better follow this behaviour, we analysed the XPS spectra by performing a non-linear mean square

fit of the data in the energy range of the Fe $2p_{3/2}$. We used a Shirley background, and we reproduced the photoemission intensity by using, as fit function, Doniach-Sunjic lineshapes, centred at the BE compatible with Fe^0, Fe^{2+} and Fe^{3+}, and at the energies of the shake-up satellites associated with Fe^{2+} oxidation state (~ 5.4eV higher BE than Fe^{2+} ; ~ 7.5eV higher BE than Fe^{3+}). We kept zero the asymmetry parameter for Fe^{2+}, Fe^{3+} and satellites peaks, whereas we used as metallic component the fit realized on a thick metallic Fe film with asymmetry equal to 0.46 which is a value compatible with the literature (0.44-0.56 eV) [28]. We fixed the Lorentzian line-width at 0.67 eV for all Fe^0, Fe^{2+} and Fe^{3+} peaks. By fits results after annealing, we observed the disappearance of the Fe^{2+} for Fe layer more than 0.25 nm, a slight increase of the metallic Fe^0 and a relevant increase of Fe^{3+} area. This behaviour is compatible with the *scenario* of a barely coarsening phenomenon which determine the slight increase of the metallic Fe^0 component, and the transition from Fe^{2+} to Fe^{3+} as consequence of annealing . Actually , regarding the latter point, this transition is in agreement with other observations in the literature [29] since the Fe^{3+} is the most stable state for Fe oxidized [30].

The XPS *scenario* of the Fe coalescence on SiO_2 after annealing is also confirmed by *ex situ* AFM measurements in air. In this case, Fe films were deposited in high vacuum conditions (base pressure 10^{-6}mbar), the films thickness were monitored *in-situ* by a quartz crystal balance during Fe deposition, and calibrated *ex-situ* by spectroscopic ellipsometry and AFM. Figure 4.4 shows the results of AFM characterization performed on both SiO_2 and Al_2O_3 supports, on as-evaporated Fe films at RT, and after annealing in vacuum at 750°C for 5 min. AFM scans were collected *ex-situ* in tapping mode at ambient conditions, therefore including the effects of Fe oxidation upon air exposure [31], which leads to an overestimation of the Fe film thickness [32].

Both SiO_2 and Al_2O_3 supports, before Fe deposition, are characterized by similar RMS roughness (~0.15 nm). The as-deposited Fe films at RT [Figure 4.4 (a), (b))] are relatively smooth and characterized by similar RMS roughness (0.19 nm), while the RMS Fe roughness on SiO_2 and Al_2O_3 supports is noticeably different after annealing in vacuum conditions (pressure $<10^{-5}$mbar) at 750°C for 6 min [Figure 4.4 (c),(d)]. In the case of Fe on SiO_2, the RMS roughness increases from 0.19nm [Figure 4.4(b)] to 2.76nm [Figure 4.4(d)], while in the case of Fe on Al_2O_3 remains unvaried (0.19nm, Figure 4.4 (a,c)]. This result suggests that Fe is subjected to a noteworthy coalescence when deposited on SiO_2, whereas on Al_2O_3 the coalescence happens barely.

Actually, other works reported on the clustering/agglomeration of Fe on SiO_2 upon annealing in vacuum [33]. Coalescence occurs whenever enough energy is fed to the system,

increasing the mobility of the atoms and allowing their diffusion over the substrate surface and clustering/agglomeration into larger islands. Coalescence is driven by a complex mechanism that involves the minimization of the surface energy and/or the free energy of the substrate/metal interface [5-8,34]. The de-wetting phenomenon is found to depend on the chemical affinity between the two compounds/elements involved. The final size of the metal islands depends on the annealing temperature and the initial film thickness. Fe and SiO_2 are characterized by a low chemical interaction, resulting in the occurrence of Fe de-wetting and increased diffusivity on SiO_2 at high temperatures [4].

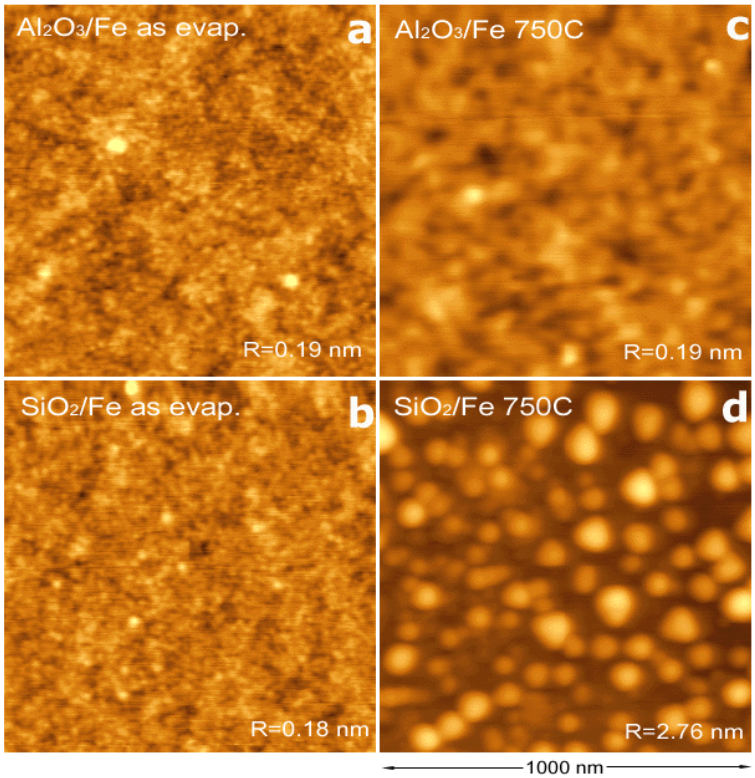

Figure 4.4 *AFM topography images of 1.1nm-thick, as-evaporated (in vacuum conditions, pressure ~10^{-6} mbar) Fe films on (a) $Al_2O_3/SiO_2/Si$ and (b) SiO_2/Si. The same films are scanned after annealing performed in vacuum (base pressure <10^{-5}mbar) at 750°C for 5min (c),(d). All scan size dimensions are 1x1 μm^2.*

Relevant coarsening of Fe on Al_2O_3 is not observed after heating in vacuum both by AFM [Figure 4.4(a,c)] and by XPS measurements (Figure 4.3). XPS indicates that evaporated Fe interacts with the oxygen of the topmost Al_2O_3 layer. As a consequence, Fe coalescence is prevented on this substrate, because the strong chemical bond formed between Fe and Al_2O_3 decreases the mobility of the metal on the underlying support. Literature also confirms these

findings [14,23]. In contrast, the weaker interaction between Fe and the SiO_2 support results in higher Fe mobility with respect to the Al_2O_3 case. These different phenomena are represented in Figure 4.5. Agglomeration of Fe into larger islands on SiO_2 as compared to Al_2O_3 is confirmed also by TEM analysis (see chapter 5).

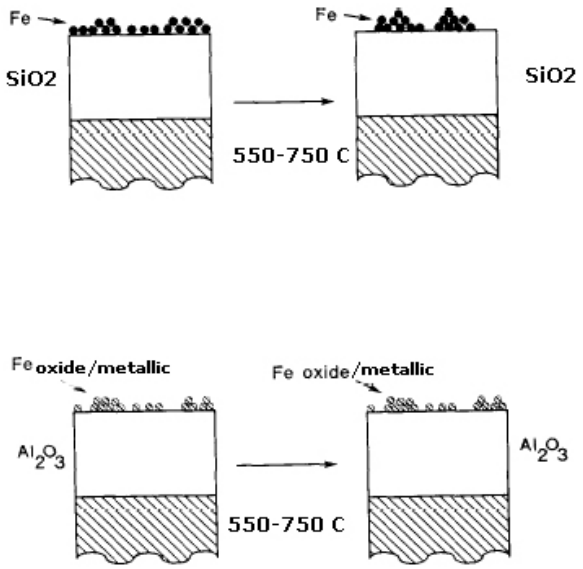

Figure 4.5 A schematic representation of the effects of heating on Fe/Al_2O_3 and Fe/SiO_2. Heating Fe/SiO_2 in the temperature range 550-750 °C causes noteworthy iron agglomeration, whereas heating Fe/Al_2O_3 in the temperature range 550-750 °C causes barely agglomeration.

4.1.3 Fe - SiO_2 interaction: effect of H_2 sputtering

It is well known in literature that the CNT yield obtained after CVD growth on Fe/SiO_2 surfaces is significantly enhanced when the catalyst film undergoes different pre-treatments, like, for example, H_2 sputtering or H_2 exposure at high pressure [33,35]. On the other hand, as we will explain in details in chapter 5, there is no need to apply any pre-treatment when the CVD growth is performed on Fe/Al_2O_3, since high CNT density as obtained by using a wide range of CVD parameters. To try to understand this point, we have studied the effect of sputtering with hydrogen ions a 0.5 nm-thick Fe film grown on SiO_2 in a controlled environment (see Appendix A1.1 for the experimental details).

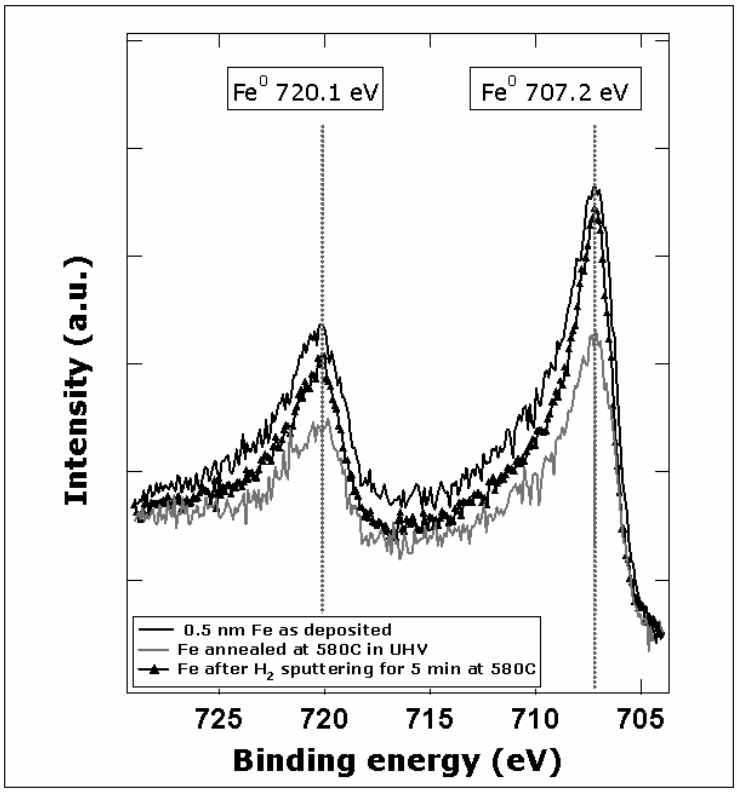

Figure 4.6 *Fe $2p_{1/2}$–$2p_{3/2}$ photoemission spectra (hv=1253.6 eV) acquired after every step of the CVD process. The black line represent the spectrum collect immediately after deposition in situ of 0.5 nm-thick Fe film on Si/SiO_2 substrates, the grey line represent the spectrum collect immediately after annealing in UHV for 5 min at 580 °C, the triangle line represent the spectrum collect immediately after exposure at H_2 sputtering (5 min) at 580 °C. All spectra are normalized to the photon flux.*

The iron film (0.5 nm thick) was deposited on SiO_2 at RT in UHV condition, and then was heated at 580°C. After that, we sputtered the films with H_2 (E_{ions}≈160eV) for 5' at 580°C. All the above steps have been performed in UHV environment, and after each step the sample has been analysed by means of *in situ* photoemission spectroscopy.

The evolution of the Fe 2*p* spectra is shown in Figure 4.6. As we have already shown in section 4.1.2, the BE of the 2*p* line of the as-deposited Fe (707.2 eV) corresponds to its metallic chemical state, [36]. We remark that no extra-components related to any Fe oxidized state or to silicides, which may inhibit the CNTs growth, are visible [37,38]. After annealing at 580°C, no significant lineshape changes are observed, but the de-wetting of the film and nano-islands formation causes the 35% decreasing of the absolute intensity of the Fe $2p_{3/2}$ peak (Figure 4.6, grey) [4,33,35] . It is well known that the islands diameter distribution depends on the initial film thickness and on the annealing temperature [39,40]. In our case, the nano-particle (NP) lateral dimension after UHV annealing is centred at ≈25 nm and has a

broad distribution, as revealed by SEM images acquired on a sample that underwent the same treatments, shown in Figure 4.7, left. The subsequent hydrogen treatment at the same annealing temperature (580°C) causes the formation of NPs with a narrower islands dimension distribution, and centred at ≈5nm, as shown in the SEM image of Figure 4.7, right. The effect of NPs redistribution is reflected also in the Fe 2*p* photoemission spectrum, with an increasing of its intensity (≈20%), as shown in Figure 4.6 (line plus triangles).

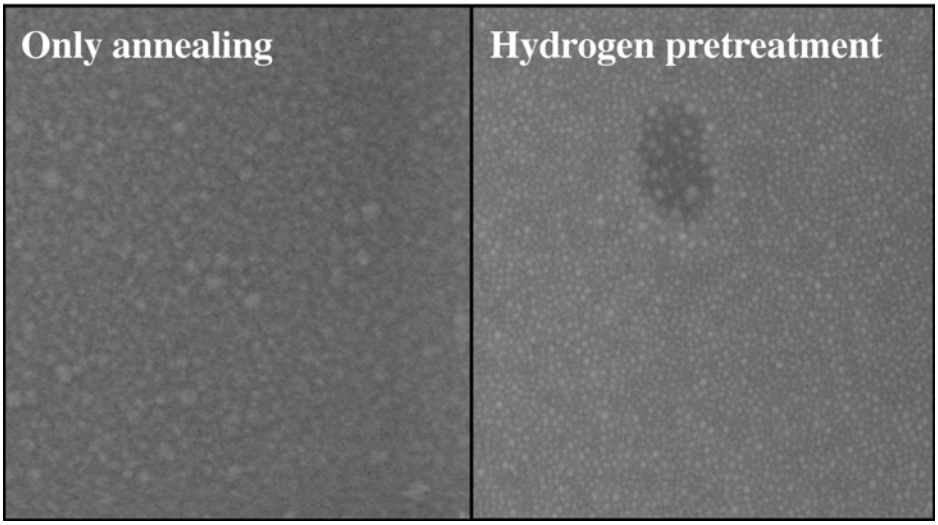

Figure 4.7 *Left: SEM image acquired after annealing at 580°C in UHV a Fe film of ≈0.5nm deposited at RT on SiO_2. Right: SEM image acquired after Hydrogen treatment at 580°C a Fe film of ≈0.5nm deposited at RT on SiO_2. Both images dimensions are 500nmx550nm.*

Actually the hydrogen exposure at high temperature a Fe film has two effects: morphological and chemical. After this treatment the film presents lower islands dimensions and narrower islands distribution with respect to the simple annealing in vacuum [33]. In addition, it reduces the generally oxidized Fe NPs, and both effects enhance the efficiency of the catalyst film for CNTs growth [33,35,41-43]. H_2 sputtering could create Fe-SiO_2 bonds [44], preventing Fe sintering during sample heating. Partial burial of Fe clusters into the underlying SiO_2 layer could induce a chemical reduction of the latter accompanied by concurrent Fe oxidation, as observed in the case of Fe deposited on native SiO_2 [44]. However no Fe 2*p* lineshape changes are observed in all the three steps of our catalyst preparation, and the same results are given also by the ultraviolet photoemission spectra acquired on the same sample (spectra not shown). These experimental data indicate that Fe remains in the same state in all the steps of the catalyst preparation, including the hydrogen sputtering. However we cannot exclude that hydrogen can have also chemical effects, not detectable by XPS.

A possible explanation could be due to the presence of chemisorbed/physisorbed species, such as hydrogen, which may alter the interaction with C_2H_2. In particular, hydrogen penetration into subsurface layers could loosen the catalyst surface and may give higher carbon diffusivities during C_2H_2 dosing, encouraging the SWNT nucleation [45].

4.2 Fe deposition on highly oriented pyrolitic graphite (HOPG)

4.2.1 Metallic films deposited on (0 0 0 1) basal plane of HOPG

Metal films deposited on the (0 0 0 1) basal plane of highly oriented pyrolitic graphite (HOPG), unlike on semiconductor and metal substrates, are described by a weak substrate-film interaction. In these systems, particularly on the atomically flat HOPG terraces, the absence of strong bonds between the metal and the substrate provides high diffusion mobility to metal adatoms and clusters [46,47]. In contrast to the terraces, the natural defects, such as step edges, exhibit strong interaction with the adsorbed metal and behave as nucleation sites for the growth of metal NPs. Such step edge features have been exploited to produce one-dimensional metal nanostructures [48,49]. Thus, the overall behaviour of most metals deposited on HOPG at RT consists of inhomogeneously distributed three dimensional (3D) metal islands (Volmer–Weber growth mode), with a concentration higher on step edges than on terraces, and a wide size distribution [50]. The metal/HOPG system is a suitable model to study the size-dependent properties of supported NPs, since the NPs intrinsic properties should not be dramatically altered by the interaction with the substrate. However, the control of growth processes and the production of NPs with desired characteristics is a challenging task.

Some recent works addressed the manipulation of growth processes and the control of size characteristics of noble NPs (Au, Ag) supported on defective HOPG [51,52]. STM investigation shows narrow size distribution of the NPs nucleated at defect sites, while X-ray photoelectron spectroscopy (XPS) studies reveal the size-dependent electronic properties of the NPs [53,54]. A bimodal Au particle size distribution (large and small clusters) on defective HOPG has been attributed to the presence of two different nucleation sites: artificially produced defect sites (for the growth of small NPs) and surface regions with high

adatom mobility (for the growth of large NPs) [55]. These results demonstrate the crucial role of artificial defects of the HOPG substrate to produce supported noble NPs with tunable structural and electronic properties.

In the following section, we show our results regarding the growth of Fe NPs on highly defective HOPG e, produced by Ar^+ ion sputtering. Preliminarily we studied the growth of Fe NPs on untreated HOPG. The vapour phase deposition of Fe on the treated substrate results in the growth of Fe NPs uniformly distributed over the surface with narrower size distribution, compared to that on non-sputtered HOPG surface. The homogenous morphology of Fe grown at RT likely implies that all underlying defects have same trapping properties, independently of their shape and size. However the STM images of sputtered and annealed HOPG surfaces show defects with different shape and size. The data are discussed on the basis of a relation between the trapping properties of defects and their geometry (size and shape).

4.2.2. Results and discussion

Before going into detailed results and discussion, we report here some important aspects of our experimental procedure. The HOPG has been cleaved in air and immediately inserted in the experimental chamber, where it has been thoroughly degassed up to 900°C for 30 min. Once the HOPG sample is inserted into the chamber, all further experiments, including sputtering, Fe deposition and annealing, have been performed *in-situ*. All Fe depositions discussed in this paper have been performed by keeping the HOPG substrate at RT. The nominal Fe deposition rate has been measured by a quartz oscillator. A fixed Fe deposition rate has been obtained by keeping the evaporation power (~3.0 W, corresponding to ~0.8 Å/min) constant by measuring the e-beam current on the Fe rod (5–4.2 mA) and the voltage applied to the Fe rod (600–700 V). The effective amount of deposited Fe has been estimated using STM data where the substrate is visible. One monolayer (ML) of Fe is taken as the surface density of the bcc metal, i.e., 12.17×10^{14} atoms/cm^2. In order to produce highly defective substrates, the HOPG has been sputtered with Ar^+ ion beam (incidence angle 30°) at a pressure of 2.7×10^{-7} mbar in sample preparation chamber, using an ion energy of 400 eV and an ion current density of 0.9×10^{13} ions/cm^2 s.

The nucleation and growth processes on HOPG of transition metals from the vapour strongly depend on the deposition conditions, such as deposition rate, coverage, substrate temperature, etc. [52]. In the results presented below, the density of defects on the substrate

surface and the amount of deposited Fe are the main parameters to control the nucleation and growth processes. Here, keeping the deposition conditions constant (formal thickness ~2 ML), we compare the Fe deposits on non-sputtered and ion-sputtered (highly defective) HOPG substrates, showing the effect of substrate surface defects on the growth processes.

First we have studied Fe deposits on the nonsputtered HOPG (0001) basal surface, which contains large atomically flat terraces. In Figure 4.8a, the STM image of the Fe deposit grown on non-sputtered HOPG is shown. The Fe growth takes place likely due to the diffusion of deposited metal adatoms and small clusters over the surface, leading to their coalescence and formation of 3D NPs randomly nucleated either on terraces or on step edges. The NPs on terraces, not trapped by defects, are weakly bonded to the substrate. They may diffuse and be captured by other NPs or substrate step edges. At steps, the NPs are immobile and completely cover the step, indicating their strong interaction with the step edges. The histogram in Figure 4.8(b), showing the Fe NP lateral size distribution, is obtained by measuring the width at half maximum from the constant current profiles of the STM images. This histogram shows a wide NPs size distribution, with a mean value of 5.85 nm and a standard deviation of 2.11 nm. The height of the NPs, also estimated from the constant current profiles in the STM images, exhibits a narrower distribution (histogram in Figure 4.8c), with a mean value of 2.76 nm and a standard deviation of 1.0 nm. The difference between corresponding values of NP height and lateral size may indicate the flattened 3D geometry of Fe NPs [51]. However, this difference may be caused by the overestimation NPs lateral size in STM image due to the tip convolution effects [51], rather than real particle geometry. Since we did not use other experimental techniques to measure the real geometry of the particles, no conclusions can be drawn on this matter. Successively, we studied the Fe deposit on highly defective HOPG surface.

The STM images of HOPG substrate with a sequence of treatments prior to Fe deposition are shown in Figure 4.9. The clean HOPG surface, possessing large terraces [Figure 4.9(a)], has been sputtered by Ar^+ (400 eV) ions for 1 min. The sputtering induces a layer of disordered carbon species, as observed in the STM image [Figure 4.9(b)]. This layer is likely formed by carbon atoms remaining on the surface after extraction from the graphite lattice sites during sputtering, since the energy of Ar+ ions (400 eV) is significantly higher than the threshold energy (~47 eV) required to extract a carbon atom from its lattice site [55].

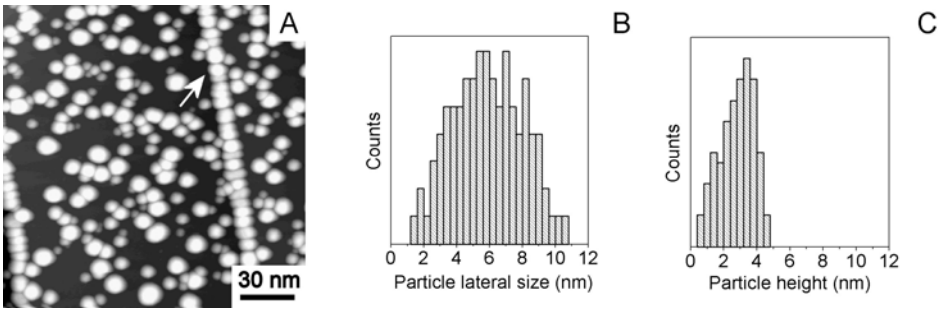

Figure 4.8 *(a) STM image (170 x 170 nm^2) of ~2ML Fe film on non-sputtered HOPG surface. Tunneling parameters: sample bias U = 2 V and tunnelling current I = 0.15 nA. The corresponding histograms show (b) the lateral size distribution with a mean value of 5.85 nm and a standard deviation of 2.11 nm, and (c) the height distribution of the Fe NPs with a mean value of 2.76 nm and variance of 1.0 nm. The arrow indicates the HOPG step edge covered with Fe NPs.*

The disordered carbon layer is removed after an in-situ annealing of the sputtered HOPG at 800 °C for 10 min, leading to different sputtering-induced defects, as shown in Figure 4.9(c).

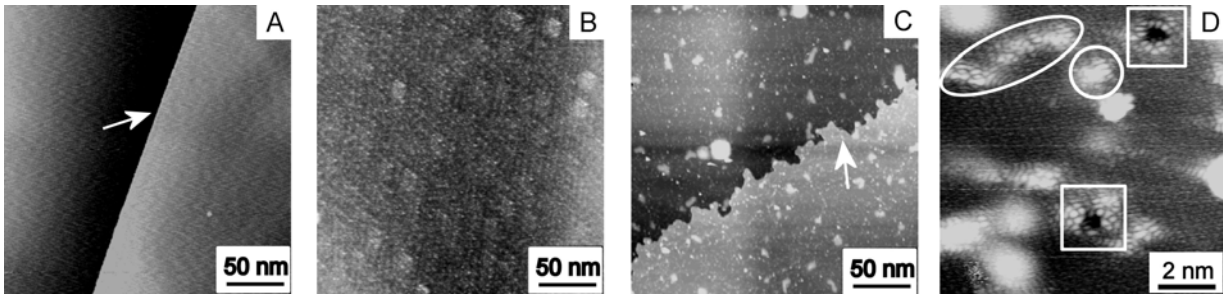

Figure 4.9 *STM images of HOPG surfaces before and after treatments. (a) Clean HOPG surface (250 x 250 nm^2). Tunneling parameters: U = -1.2 V, I = 0.2 nA. (b) HOPG surface after sputtering with Ar+ beam (400 eV) for 1 min (250 x 250 nm^2). Tunneling parameters: U = -1 V, I = 0.3 nA. (c) (250 x 250 nm^2). HOPG surface after sputtering and subsequent annealing at 800°C. Tunneling parameters: U = -0.8 V, I = 0.2 nA. Arrows in images (a) and (c) show the HOPG step edges. (d) High resolution STM image (10 x10 nm^2) of sputtered and annealed HOPG surface. Tunneling parameters: U = -0.4 V, I = 0.2 nA. The squared area shows the craters surrounded by distorted crystalline structure. Defects with circular and elongated shapes are shown with circle and ellipse, respectively.*

The high resolution STM image [Figure 4.9(d)] shows atomically resolved hillock-like structures and craters surrounded by distorted lattice, as previously observed [56]. These defects have different shapes and dimensions, as evidenced by circles and squares in [Figure 4.9(d)]. Fe deposited on this highly defective HOPG surface exhibits significantly different morphology compared to Fe deposited on non-sputtered HOPG surface. A typical STM image of a formal thickness ~2 ML Fe film is shown in [Figure 4.10(d)], which resembles the results of recent works [52,53] on noble NPs produced in a similar way. Unlike on the non-sputtered HOPG surface, where Fe NPs are preferentially located on step edges, on the defective surface the terraces provide high density nucleation sites as well, resulting in the uniform distribution of the Fe NPs over the entire surface.

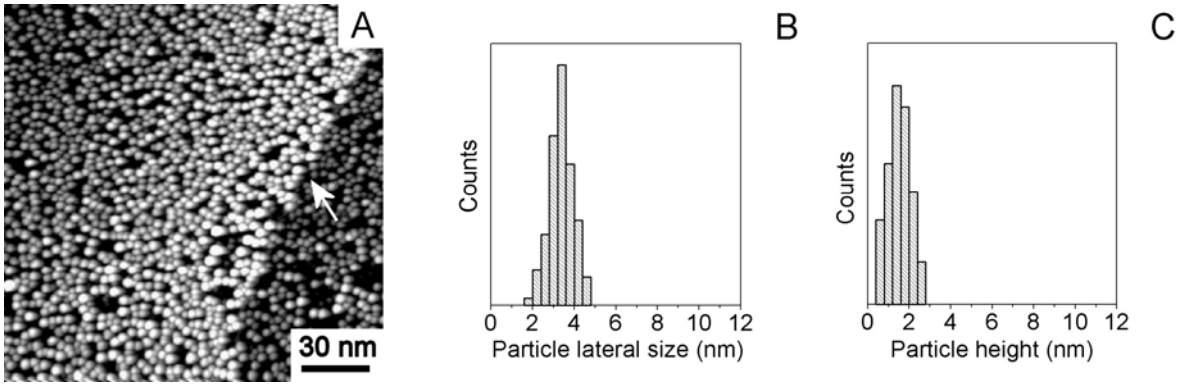

Figure 4.10. *(a) STM image (170 x 170 nm^2) of ~ 2ML Fe film deposited on Ar^+ ion sputtered HOPG surface. Tunneling parameters: U = 2 V, I = 0.15 nA. The corresponding histograms show (b) lateral size distribution with a mean value of 3.28 nm and standard deviation of 0.58 nm, and (c) heightdistribution of Fe NPs with a mean value of 1.4 nm and standard deviation of 0.26 nm. The arrow shows the HOPG step edge covered with Fe NPs.*

This behavior can be explained by the uniform distribution of sputtering-induced defects on the surface, observed in Figure 4.9(c), implying that these defects act as nucleation sites for the growth of Fe NPs, by trapping the mobile metal species in the vicinity. The histogram in Figure 4.10(b) shows the lateral size distribution of the 3D NPs, with an average size of 3.28 nm and a standard deviation of 0.58 nm. Compared to the histogram of Figure 4.8 (b), one can note the narrowing of the NP lateral size distribution. This can be explained by taking into account the effect of sputtering-induced defects on the growth process kinetics. In the initial stage, Fe atoms adsorbed on defect-less regions can diffuse over surface until they are captured by defects. Although the mobility of the atoms may not necessarily be changed, with

respect to that on non-sputtered HOPG terraces, the diffusion kinetics of adsorbed Fe atoms may be significantly varied. The change is likely ascribed to the variation of the diffusion path length of Fe adatoms. Assuming that the diffusion path length is proportional to the distance between defects, the high density of sputtered-induced defects results in a decrease of the diffusion path length, so that only NPs located in the vicinity of a defect can be trapped at this defect. For a given amount of deposited Fe, the number of adatoms nucleated at a defect, i.e., the size of the NPs, depends on the defects density. We therefore suggest that the uniform coverage with narrow lateral size distribution of the Fe NPs can be ascribed to the effect of sputtering-induced defects on the growth process. Histogram in Figure 4.10(c) shows the Fe NP height distribution, estimated from the constant current profile taken from STM images. Compared to the NPs deposited on non-sputtered HOPG [Figure 4.8(c)], in this case the mean height (1.4 nm, standard deviation of 0.26 nm) is twice smaller. However, precise estimation of the real height distribution of Fe NPs on sputtered HOPG is difficult, because the sputtered HOPG is significantly rough [see Figure 4.9(d)], and this roughness may affect the NP height estimation. Therefore further interpretation of the height distribution in this case is complicated and may lead to doubtful conclusions. One should note that, though the NPs grown at RT have uniform apparent shape and the overall morphology of the Fe film is correlated to the uniform distribution of defects on the substrate, the sputtering-induced defects on the HOPG surface have different shape and size [see circles and squares in Figure 4.9(d)]. This would suggest the absence of correlation in shape and size between a given defect morphology and the Fe NP shape grown on this defect at RT. In order to obtain more information on the defect trapping properties, the Fe deposits have been annealed in-situ at 800 °C for 3 min.

For comparison, we have first annealed ~2 ML Fe deposited on non-sputtered HOPG [Figure 4.11(a)]. After annealing, the Fe NPs remain only at step edges, while the terraces are almost swept off clusters, indicating that during annealing most of Fe re-evaporate from the surface. In the case of Fe deposited on sputtered HOPG, after annealing the step edges are still decorated by Fe particles, while the terraces present NPs trapped at the defects [Figure 4.11(b)]. The size of the NPs ranges from few nanometers up to about 15 nm. We did not present a histogram for this case, because NPs with size of the order of the defect size cannot be distinguished from the defect itself. However, the distinguishable NPs present a wide size distribution, likely indicating different trapping behavior of different defects. During annealing, the Fe NPs weakly trapped on defects, such as local surface distortions, may re-evaporate from the surface or diffuse and coalesce with the strongly trapped Fe particles, and

thus on some defects the metal particles are completely absent [circle in Figure 4.11(c)]. On the other hand, the metal particles strongly interacting with defects, such as craters, remain immobile and may grow up by agglomerating other Fe particles [see Figure 4.11(b)]. However, further comprehensive studies as function of various film coverage, different defect characteristics (by changing the sputtering conditions), and different annealing temperatures are needed in order to understand the relation between the growth processes of the metal particles and the characteristics of sputtering-induced defects.

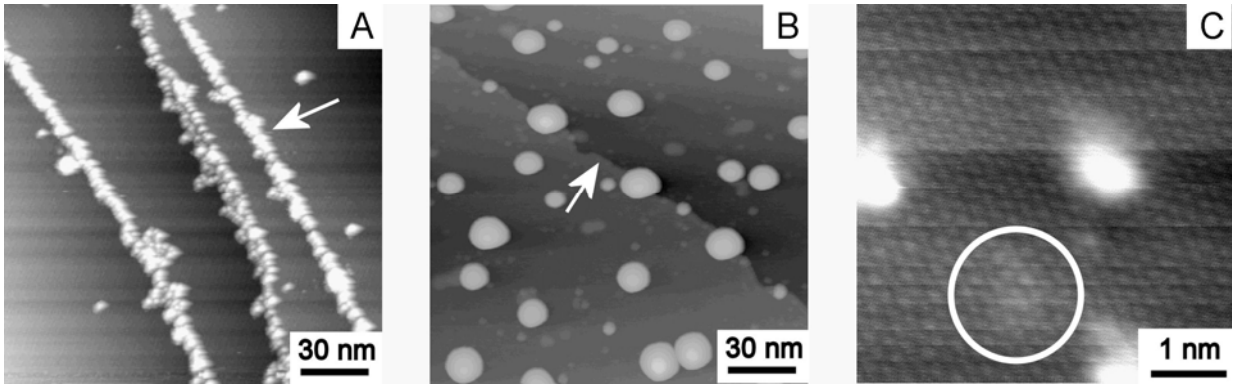

Figure 4.11. *STM images of ~2 ML Fe films annealed in-situ at 800 °C: (a) (170 x 170 nm^2) deposited on unsputtered HOPG, showing clean substrate terraces and Fe particles trapped only at step edges. Tunneling parameters: U = -2.5 V, I = 0.3 nA. (b) (170 x 170 nm^2) deposited on sputtered HOPG, showing the NPs trapped at defects on terraces. Tunneling parameters: U = -1.4 V, I = 0.2 nA. Arrows in images (a) and (b) show the HOPG step edges covered by Fe. (c) High magnification (5 x 5 nm^2) STM image of the Fe/sputtered HOPG surface, showing a defect (circle) where the metal particles are completely absent. Tunneling parameters: U = 0.15 V, I = 0.4 nA.*

4.3 Summary and conclusions

In this chapter the experimental results concerning the chemical interaction between Fe deposits (from <0.1 nm up to 0.8nm) and the substrates that are generally used for CNT growth, i.e. SiO_2, Al_2O_3, and HOPG have been reported. The goal was to understand how the choice of a particular substrate, and/or a particular catalyst treatment, can influence the size-distribution of catalyst NPs and, consequently, the growth of CNTs via CVD. Actually several experimental results demonstrated that Al_2O_3 surface is a CNT growth promoter, but so far only few groups paid attention to the influence of the substrate and of the substrate-catalyst interaction.

Fe depositions have been performed in different UHV experimental apparatus. In the case of Fe/SiO_2 and Fe/Al_2O_3, we have performed *in situ* XPS investigations on the as deposited system, after annealing at the CNT growth temperature, and after H_2 sputtering treatments. All samples have been *ex-situ* characterized also by SEM and AFM. In the case of Fe deposition on HOPG the catalyst NPs distribution, after different surface preparations and annealing temperatures, has been studied by *in situ* STM. After heating at the temperature of growth (580°C, 750°C), we found a barely coarsening phenomenon of the Fe NPs on Al_2O_3, connected with a strong chemical interaction between Fe and Al_2O_3. On the contrary, after annealing at the same temperature, we found a noteworthy coarsening of the Fe NPs on SiO_2/Si, in conjunction with no evidence of $Fe\text{-}SiO_2$ chemical bond. We connect this different catalyst particles size-distribution to the significant different chemical interaction between the catalyst and the two substrates, and it explains the systematically higher yield of CNTs achieved on Al_2O_3 substrate. Similar catalyst NPs size-distribution, found on the Al_2O_3 substrate, can be achieved also on SiO_2, but only after H_2 sputtering. In addition, we found that the above treatment does not causes any significant changes in the chemical state of the catalyst, and does not promote any further bonding with SiO_2.

We have also studied the effect of substrate surface defects on the Fe film morphology by comparing films deposited on non-sputtered and Ar^+ ion-sputtered HOPG surfaces. In the first case the Fe particles, with higher density on the step edges than on terraces, have a larger size distribution; in the latter case the Fe NPs, uniformly arranged over the surface, have a narrow size distribution. The overall morphology of Fe deposits on sputtered HOPG is correlated to the uniform distribution of substrate defects. However, an individual defect morphology does not correlate with the shape of Fe NPs grown on this defect at RT. Annealing the films at 800°C reveals different capturing properties of the sputtering-induced defects. The obtained Fe/HOPG system can be considered as a suitable system for further studies of size-dependent magnetic and catalytic properties of Fe NPs also for CNT growth via CVD.

Bibliography

[1] Campbell C. T., *Surf. Sci. Rep*. 27, 1 (1997).

[2] Parker S. C., Grant A. W., Bondzie A.V. and Campbell C. T., *Surf. Sci*. 441, 10 (1999).

[3] Wallace W.T, Min B.K., and Goodman D.W., *Topics in Catalysis* 34, 17 (2005).

[4] Pretorius R., Harris J. M. and Nicolet M. A., *Solid State Electron*. 21, 667 (1978).

[5] Wen J. M., Evans J. W., Bartelt M. C., Burnett J. W. and Thiel P. A. , *Phys. Rev. Lett*. 76, 652 (1996).

[6] Jiran E. and Thompson C. V., *J. Electron. Mater*. 19, 1153 (1990).

[7] Bartelt N. C., Theis W. and Tromp R. M., *Phys. Rev. B* 54, 11741 (1996).

[8] Gadkari P. R., Warren A. P., Todi R. M., Petrova R. V. and Coffey K. R., *J Vac. Sci. Technol.* A 23, 1152 (2005).

[9] Venables J. A*., Surf. Sci*. 300, 798 (1994).

[10] Moulijn J. A., van Diepen A. E. and Kapteijn F., *Appl. Catal. A* 212, 3 (2001).

[11] Qi Y., Cagin T., Johnson W. L. and Goddard W. A., *J. Chem. Phys*. 115, 385 (2001).

[12] Harutyunyan A. R., Mora E., Tokune T. , Bolton K., Rosén A., Jiang A., Awasthi N., and Curtarolo S., *Appl.Phys.Lett* 90, 163120 (2007).

[13] De los Arcos T., Garnier M. G., Seo J. W., Oelhafen P., Thommen V. and Mathys D., *J. Phys. Chem. B* 108, 7728 (2004).

[14] Arranz A., Perez- Dieste V., Palacio C., *Surf. Sci*. 521, 77 (2002).

[15] M.G. Barth, Rolland A., *Thin Solid Films* 76, 45 (1981).

[16] Myers C.E ., Franzen H.F., Anderegg J.W. , *Inorg. Chem*. 24, 1822 (1985).

[17] Allen G.C ., Curtis M.T., Hooper A.J., Tucker P.M. , *J. Chem. Soc. Dalton Trans*. 1525 (1974).

[18] Mills P., Sullivan J.L., *J. Phys. D.* 16, 723 (1983) .

[19] Konno H., Nagayama M. J. , *Electron Spectrosc. Relat. Phenom*. 18, 341 (1980).

[20] Domen K., Chuang T.J., *J. Chem. Phys*. 90, 3318 (1989).

[21] Brainard W.A., Wheeler D.R., *J. Vac. Sci. Technol*. 15, 1801 (1978).

[22] Strohmeier B.R., Hercules D.M., J. *Phys. Chem*. 88, 4922 (1984)

[23] Colaianni M.L., Chen P.J., Yates J.T., *Surf. Sci*. 238, 13 (1990).

[24] Johnson K.H., Pepper S.V., *J. Appl. Phys*. 53, 634 (1982).

[24] Fujimora T., Tanaka S.I., *J. of Mater. Sci.* 34, 425 (1999) .

[25] I. Okamoto, Naka M., Asami K.and Hashimoto K., *Trans. JWRI* 11, 131 (1982).

[26] Sakata K., Honma K., Ogawa K., Watanabe O.and Nii K., *J. Mater. Sci.* 21, 4463 (1986).

[27] Naka M., Okamoto I., *Quart. J. Jpn. Welding Soc*. 3, 702 (1985).

[28] van Campen D.G., Pouliot R.J., Klebanoff L.E., *Phys.Rev.B*, 48, 17533 , (1993).

[29] Simmons J. M., Nichols B.M, Marcus M.S., Castellini O. M., Hamers R. J., and Eriksson M.A., *Small* 2,902 (2006).

[30] Chase M.W., *J. Phys. Chem. Ref. Data* 9, (1998)

[31] Wang C. M., Baer D. R., Thomas L. E., Amonette J. E., Antony J., Qiang Y., Duscher G.,*J. Appl. Phys*. 98, 94308 (2005).

[32] Gan L., Gomez R.D., Powell C.J., McMichael R.D., Chen P.J., Egelhoff W.F., *J. Appl. Phys*. 93, 8731 (2003).

[33] Pisana S., Cantoro M., Parvez A., Hofmann S., Ferrari A.C., Robertson J., *J. Phys. E* 37, 1 (2006).

[34] Liehr M., Lefakis H., Legoues F.K., Rubloff G.W., *Phys. Rev*. B 33, 5517 (1986).

[35] Cantoro M., Hofmann S., Pisana S., Ducati C., Parvez A., Ferrari A. C., and Robertson J., *Diamond Relat. Mater.* 15, 1029 (2006).

[36] Panzner G., and Egert B., *Surf. Sci*. 144, 651 (1984).

[37] Nemoshalenko V.V., Didyk V.V., Krivitskii V.P., Senekevich A.I., *Zh. Neorg. Khimii* 28, 2182 (1983).

[38] Shabanova I.N., Trapeznikov V.A., *J. Electron Spectrosc. Relat. Phenom*. 6, 297 (1975).

[39] Colomer J. F., Stephan C., and Lefrant S., *Chem. Phys. Lett.* 317, 83 (2000).

[40] Wei Y. Y., Eres G., Merkulov V. I., and Lowndes D. H., *Appl. Phys. Lett.* 78, 1394 (2001).

[41] Vajtai R., Wei B. Q., and Ajayan P. M., *Philos. Trans. R. Soc. London* A 362, 2143 (2004).

[42] Hofmann S., Cantoro M., Kleinsorge B., Casiraghi C., Parvez A., Ducati C., and Robertson J., *J. Appl. Phys*. 98, 34308 (2005).

[43] Hofmann S., Ducati C., Kleinsorge B., and Robertson J., *Appl. Phys. Lett*. 83, 135 (2003).

[44] Garnier M. G., de los Arcos T., Boudaden J., and Oelhafen P., *Surf. Sci*. 536, 138 (2003).

[45] Paal Z., and Menon P. G., *Hydrogen Effects in Catalysis*, Dekker (New York) (1988).

[46] Lewis L.J., Jensen P., Combe N., Barrat J.L., *Phys. Rev*. *B* 61, 16084 (2000).

[47] Bardotti L., Jensen P., Hoareau A., Treilleux M., Cabaud B., *Phys. Rev. Lett*. 74, 4694 (1995).

[48] Atashbar M., Banerji D., Singamaneni S., Bliznyuk V., *Nanotechnology* 15, 374 (2004).

[49] Walter E., Murray B., Favier F., Kaltenpoth G., Grunze M., Penner R., *J. Phys. Chem. B* 106 11407 (2002).

[50] Binns C., Baker S.H., Demangeat C., Parlebas J.C., *Surf. Sci. Rep.* 34, 105 (1999).

[51] Lopez-Salido I, Lim D.C., Kim Y.D., *Surf. Sci.* 588, 6 (2005).

[52] Lopez-Salido I., Lim D.C., Dietsche R., Bertram N., Kim Y.D., *J.Phys. Chem. B* 110, 1128 (2006).

[53] Buttner M., Oelhafen P., *Surf. Sci*. 600, 1170 (2006).

[54] Bansmann J.et al., *Surf. Sci. Rep.* 56, 189 (2005).

[55] Marton D., Boyd K.J., Lytle T., Rabalais J.W., *Phys. Rev. B* 48, 6757 (1993).

[56] Hahn J.R., Kang H., *Phys. Rev. B* 60, 6007 (1999).

Chapter 5

CNT Growth on Al_2O_3 and SiO_2

In this Chapter the experimental results concerning the CNT growths on SiO_2 and Al_2O_3 substrates via Chemical Vapour Deposition (CVD) will be discussed. The CVD processes were performed in different experimental apparatus, spanning significantly different CVD parameters. By using the same experimental conditions, we found a systematically higher yield of CNTs on Al_2O_3 with respect to SiO_2. The different results are explained to be due to the different size-distribution of the catalyst NPs observed on the two substrates before growth, which are strictly related to the different metal/substrate interaction (as shown in Chapter 4).

The first part of the chapter (5.1) gives a short introduction explaining the motivations and the importance of the experimental data we acquired. Then, in 5.2, the results of CVD processes performed in UHV chamber on SiO_2 and on Al_2O_3 as a function of the growth parameter (temperature, pressure and catalyst thickness) are summarized. The next section (5.3) underlines the substrate role in the CNTs CVD growth and the catalyst chemical state. In section 5.4 we show some preliminary results concerning the influence of the growth pressure in the CVD process for CNTs growth. Finally we present our conclusions in 5.5.

5.1 Introduction

Understanding the catalytic processes involved in the growth of carbon nanotubes (CNTs) by catalytic CVD is important to achieve the desired degree of growth control.

To achieve a high degree of applicability in the industrial technology, it is crucial to reach a complete control on the SWNTs morphology directly on the appropriate substrate. Structures of large-scale organized SWNTs, consisting of high density forest of vertical aligned nanotubes, are useful for the fabrication of nanotube-based devices, as nanotransitors [2], electron emitters for optoelectronic displays [3] and nanoelectrodes for DNA detection [4]. In addition, large-scale arrays of SWNTs forming macroscopic cylinder show high uniformity and flexibility [5], which are characteristic adapted to yarn fabrication [6,7].

Since several years, vertical alignment of MWNTs has been obtained [8-10] but only recently (2004) a fast development in the growth techniques included the achievement of vertically aligned (VA) high density forest of SWNT/MWNTs [11] and of SWCNTs [5,12-15] by direct CVD process without applying any electric or magnetic field. The forest of VA-SWNTs with high degree of purity and without amorphous carbon and CNF/MWNT have been obtained by using different tricks in the CVD conditions, such as employing etching compounds for amorphous carbon (like alcohol as carbon precursor or adding water), and controlling the catalyst NPs size-distribution by using the appropriate substrates, as the density and alignment of thermal-CVD grown CNTs are strongly related to interactions of metal catalysts with (oxide) support layers. Refs [16,17] reported that only by using Al_2O_x or Al_2O_3 as support layers, a dense growth of VA-SWCNT has been obtained. Otherwise, by employing the same growth conditions, only a low density of horizontal SWCNTs has been grown on Fe/SiO_2. These results show the essential role of the Al_2O_3 support layer as an enhancer of the nanotube growth rate.

So far few groups paid attention to the influence of the substrate on the CNTs growth [18-21] and to the catalyst chemical state. De los Arcos, et al. [18,21] studied the Fe chemical state by XPS and the Fe NPs size distribution of Fe films deposited in low vacuum chamber on Al_2O_3, TiN and TiO2 supports. The analysis was done at different stages: as deposited, after annealing and after the growth of CNF mixed with a little amount of CNT. They observed that after annealing in a vacuum (10^{-5} mbar) up to 840 °C of a Fe deposit, the smallest diameter distribution among all the substrates considered (TiN, TiO_2, Al_2O_3) is on Al_2O_3 support. In addition the Fe NPs have higher oxidized component than the ones deposited on TiO_2 and TiN. They emphasize that dense growth of thin nanotubes with a comparatively fast growth rate is promoted by FeO particles, while more metallic particles on TiN and on TiO_2 of roughly the same size, showed a very poor performance. They address that the final chemical state of the catalyst (therefore a mixture metallic/oxidized) determines in turn the growth mode of CNT, though it is not clear if each particle is a mixture of the two

phases, or if two different families of particles (metallic and oxidized) are present. Therefore so far the influence of different support layers (Al_2O_3, SiO_2, TiO_2 etc) on the chemical state and on the morphology of the catalyst NPs is still unknown.
We studied CNT growth on Al_2O_3 and SiO_2 substrates in three different experimental apparatus. We used significantly different growth parameters, but the same CVD process has been performed on the two substrates in each experimental system.

5.2 CNT CVD low pressure growth: temperature, catalyst coverage and pressure dependence

We have performed a systematic investigation of CNTs growth via CVD at low pressure (<$8x10^{-4}$ mbar), spanning different growth conditions. The CNTs have been grown on SiO_2 and Al_2O_3 substrates via CVD in different UHV experimental systems, where all the steps of the CVD process and of the catalyst film preparations have been done in sequence, without any contamination due to air exposure. In these apparatus (Appendix A.1.2) it is possible to control the chemical state of the catalyst (before and after the growth) and to monitor precisely all the CVD parameters like: precursor gas purity, partial gas pressures and gradients, sample temperature, gas fluxes, etc. Using similar experimental conditions, we were able to reproduce the same growth results in all the different experimental systems. The CVD processes have been performed by using SiO_2 and Al_2O_3 as substrate, Fe as catalyst, and acetylene as precursor gas. All the samples have been analysed *in-situ* by photoemission spectroscopy, after each step of our growth procedure (described in the experimental section, see also chapter 4), to study all the possible chemical changes and to exclude the presence of any contaminations. All samples have been characterized also *ex-situ*, after the growth, by scanning electron microscopy (SEM) and Raman spectroscopy.

The growth and catalyst preparations have been performed by exploring the following parameter ranges: Fe thickness (≈0.08nm-0.8nm), acetylene growth pressure ($7x10^{-7}$mbar-$1x10^{-3}$mbar), and growth temperature (400°C-660°C). In the temperature range used, we can assume that the Fe NPs (formed upon annealing) are in solid state during the entire CVD process [22].

A typical CVD route consisted of a preliminary outgassing of the substrate at 550-600°C, followed by Fe catalyst deposition at RT, and successive ramping-up to the actual

CNT growth temperature (see Appendix A2.1. for more experimental details). Finally, the CVD process was performed dosing acetylene at the growth temperature.

Here we summarize the resulting CNT(F)s obtained on the two substrates in the range of investigated parameters. Figure 5.1 shows the resulting CNT(F)s on Fe/Al_2O_3 system for Fe layer thickness ~0.1-0.8 nm. For thickness lower than ~0.1nm we did not observe any tubular graphitic structure. By changing the range of Fe thickness from ~0.1 up to 0.8 nm, we observed that it affects the diameter of the CNT. In particular the CNT diameter decreases and the width of diameter distribution becomes narrower by decreasing the Fe thickness (by Raman spectroscopy measurements, due to the cut-off of our notch filter, we cannot detect SWNT diameters >2 nm.).As the diagram shows (Figure 5.1), we can obtain high density of SWNTs at very low pressure, like $8x10^{-6}$ mbar at temperature about 580-600°C. Going down with the pressure the density of the CNTs decreases and at the same time more defective tubes and short CNFs (~ 20-50 nm) grow. The lowest pressure at which tubular structure have been identified is $7x10^{-7}$ mbar. We precise that the reported pressures are the real pressures exerted from the C_2H_2 gas on the sample because of the gas at the growth pressure was introduced in ~ 1-3 sec by opening a valve .That was done by separating the growth chamber from the pre-chamber which was previously filled with C_2H_2 at a pressure slightly higher than the growth one.

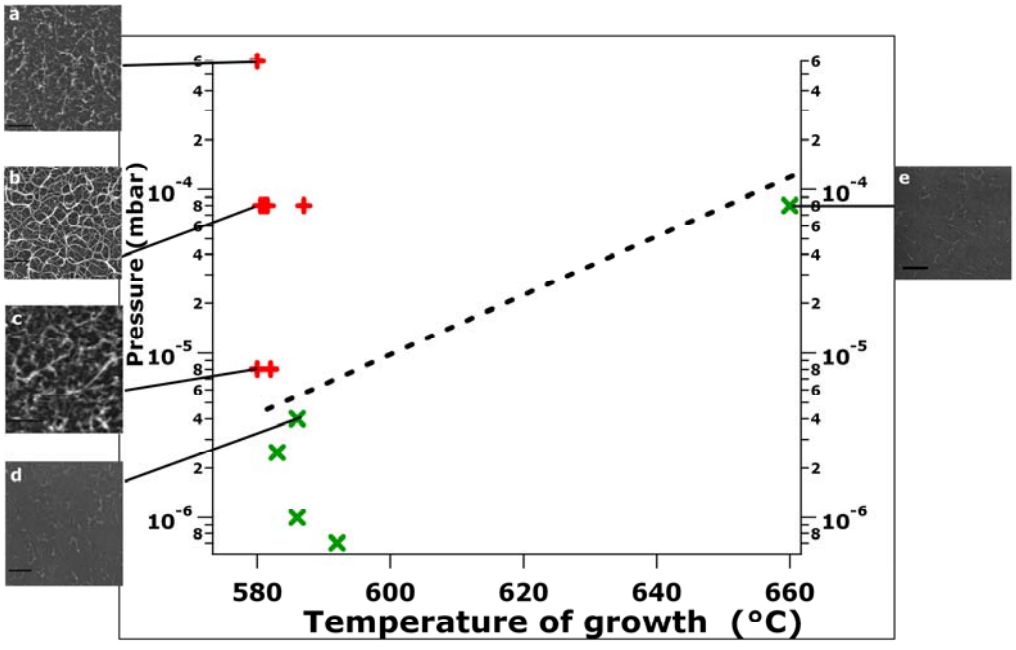

Figure 5.1 *Fe (0.1-0.8nm) /Al_2O_3/SiO_2/Si: SEM images of SWCNT bundles grown at the reported conditions, more precisely the pressure are: (a) 580 °C, 6×10^{-4} mbar [scale bar 100nm] (b) 580 °C,*

8×10^{-5} mbar [scale bar 200nm] (c) 580 °C, 8×10^{-6} mbar [scale bar 100nm] (d) 586 °C, 4×10^{-6} mbar [scale bar 200nm] (e) 660 °C,8×10^{-5} mbar [scale bar 200nm].

We want also to remark that these are extreme conditions, no other work is present in the literature were CNTs can be grown at this low pressure. The best growth temperature was about 580-600°C, increasing the temperature up to 660°C we observed a decreasing of the density of CNTs and also the highest temperature used (660°C) seems promote the growth of CNFs with respect to CNTs. We explain this behaviour with a probably coalescence phenomenon of the Fe atoms/NPs into bigger islands whose diameter favours the nucleation of CNFs. On SiO_2 we obtained very low density of CN(F)Ts and, sometime not reproducible growths [0.5 nm-thick Fe film to undiluted C_2H_2 (8×10^{-4} mbar pressure) for 5 min at 580 °C, Figure 5.2(a)]. We investigated these parameter range: 0.1-0.5 nm Fe, 400-600°C, at pressures of growth ~10^{-3} mbar. To try to increase the CNT yield, we tested a pretreatment of the catalyst layer at the growth temperature by H_2 sputtering (sputter gun, Δt =20', E_{ions}=300 eV). In this case, at 580°C and at $8x10^{-4}$ mbar [Figure5.2(c)] we obtained the same density of SWNT-bundles obtained on Fe/Al_2O_3 system. By decreasing the temperature up to 400°C we obtained high density of CNFs [Figure 5.2(b)].

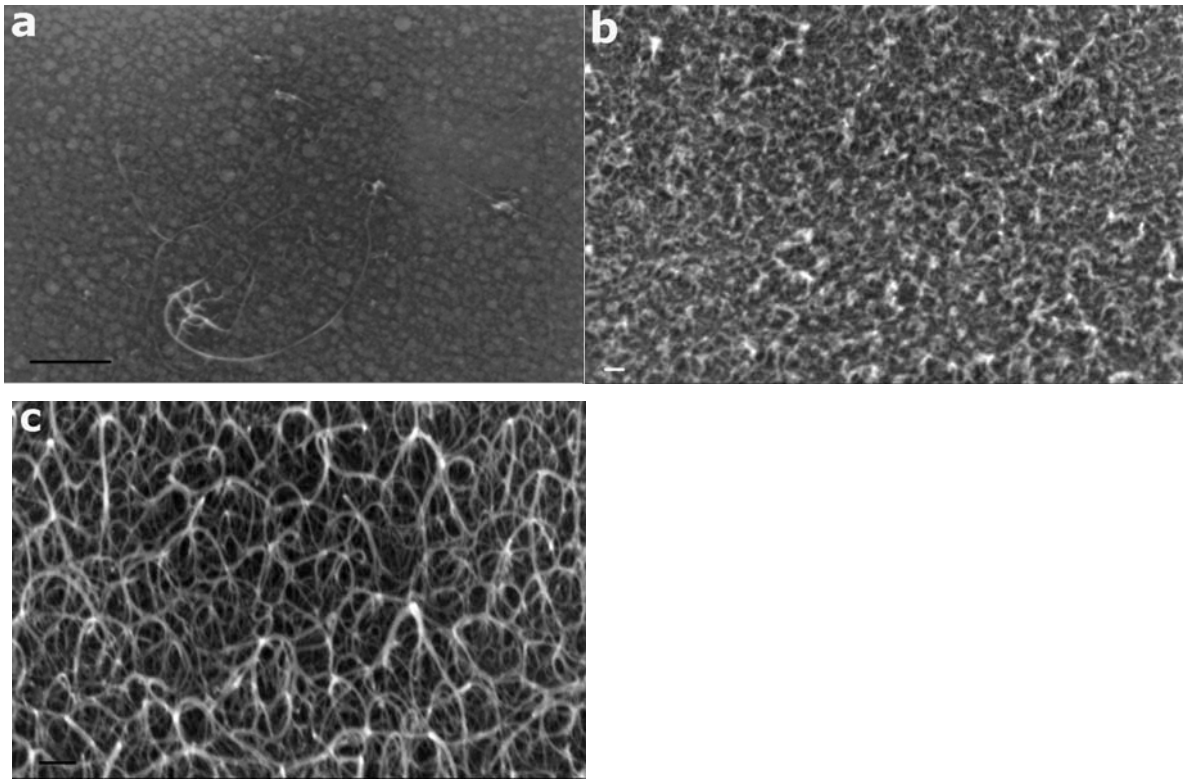

Figure 5.*2 Fe(0.5nm) /SiO_2/Si: (a) SWNT and CNF growth at 580°C at $8x10^{-5}$ mbar C_2H_2 pressure (b) CNF growth at 400°C at $8x10^{-5}$ mbar applying H_2 sputtering on Fe layer at 580°C before growing*

(c) SWNT bundles grown at 580°C at 8x10^{-5} mbar C_2H_2 pressure applying H_2 sputtering on Fe layer at 580°C before growing [scale bars: (a)100nm,(b)100 nm,(c)20nm].

5.3 CNT CVD growth: substrate dependence

Figure 5.3 shows the results of CNT growths performed in three different equipments, by exposing Fe layers of similar thickness (0.3-0.5nm) to CVD processes. The substrates were commercial, polished n-type Si(100) wafers covered with 150nm thermally grown SiO_2 [Figure 5.3(a-c), left], or covered with 150nm thermally grown SiO_2 plus 10nm of sputtered Al_2O_3 [Figure 5.3(d-f), right]. We used significantly different growth parameters, but we stress that the same CVD process and the same catalyst pre-treatment have been done in each experimental apparatus on both substrates. In particular the growths have been performed in significant different conditions: at very low growth pressure (8x10^{-5}mbar), at low growth pressure (10^{-2}-10^{-3} mbar) and at atmospheric pressure. After growth all samples have been characterized by Raman spectroscopy, AFM, SEM and/or TEM. Figure 5.3(a,d) shows the results of the lowest-pressure growth, carried out in the UHV chamber (see Appendix A1.1 for more experimental details). The growth procedure consisted in annealing an *in-situ* deposited, 0.5 nm-thick Fe layer at 580°C for 5 min, and then exposing it to undiluted C_2H_2 (8x10^{-5} mbar) at the same temperature. We observe a dense mat of bundled SWNTs (as revealed by Raman, not shown), distributed mainly laterally on the substrate, in the case of growth on Al_2O_3-supported substrate [Figure 5.3 (d)], while the SWNT yield is significantly lower on SiO_2 support [Figure 5.3 (a)]. As we are going to show, this trend has been observed in all experimental apparatus we used.

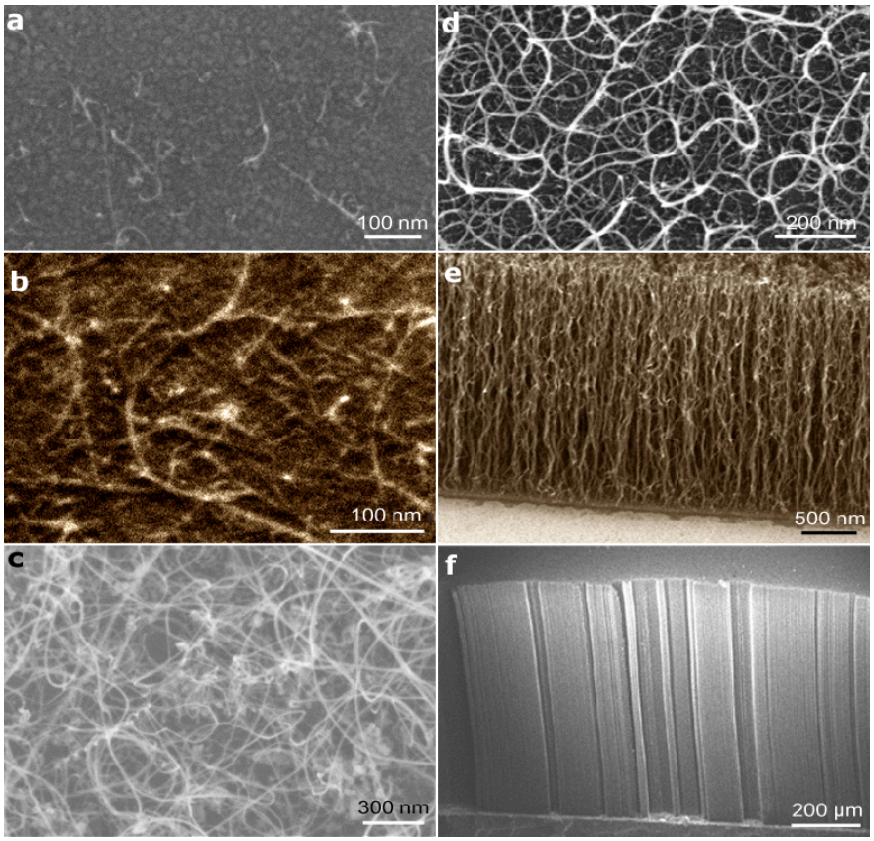

Figure 5.3 *SEM images of CNTs grown by thermal CVD on SiO_2 supported substrates (a-c) and on Al_2O_3 supported substrates (d-e) in different experimental apparatus. Figures(a) and (d) refers to the growth done in UHV apparatus, (b) and (e) in a low vacuum apparatus, (c) and (f) in a conventional furnace.*

In Figure 5.3(b,e) the results of the growths performed in low vacuum conditions are shown (see appendix A1.2 for more experimental details). The CNTs were grown by annealing an *ex-situ* deposited Fe layer (thickness:0.5nm) at 500°C in NH_3 atmosphere (0.6 mbar) for 15 min, and then exposing the layer to undiluted C_2H_2 (10^{-2}-10^{-3} mbar) at the same temperature for 5 min at 500°C. A transition from long, bundled SWNTs (as revealed by Raman, not shown) arranged mainly laterally on the substrate [Figure 5.3(b)] to a mixture of SWNTs and more vertically extended CNFs [Figure 5.3(e)] (as revealed by Raman, not shown) is observed when passing from a SiO_2-supported to a Al_2O_3 supported substrate. Finally, the samples shown in Figure 5.3(c,f) have been grown by annealing an *ex-situ* deposited Fe layer (thickness: 1.1nm) in 2:5 Ar:H_2 atmosphere at 750°C for 15 min, and then exposing the layer to 2:5:0.1 Ar:H_2: C_2H_2 (atmospheric pressure) at 750°C for 5 min in a conventional horizontal furnace. The growth on Al_2O_3-supported Fe catalyst results in up to ~0.7 mm long, vertically oriented, dense MWNT forests [Figure 5.3(f)] (by Raman spectroscopy). By using this

condition it is possible to obtain rate of growth up to 500 μm/min and hence several mm long-vertically oriented MWNT forests in 20 min (not shown). Also in this case, the CNT yield is drastically reduced when using SiO_2 as catalyst support and in this case only disordered MWNTs parallel to the substrate were observed as growth result [Figure 5.3(c)]. From the above results it is clear that Al_2O_3 as catalyst support has a crucial role in CNT growth, and allows a drastic increase in CNT density and length with respect to SiO_2 support. Chemically speaking, XPS measurements showed that Fe does not form bonds with SiO_2, and this imply a in higher NP mobility on SiO_2 than on Al_2O_3 at high temperatures (see section 4.1.2). The high mobility of Fe on SiO_2 creates islands too large for the nucleation of SWNTs (particularly in the case of CNT growth in HV/UHV conditions) and a large distribution of their diameters, which hinders the vertical growth of CNT. Actually, dense VA-SWNTs forests are mostly affected by the density and diameter distribution of the catalyst NPs. These conditions are satisfied on Fe catalyst layers grown on Al_2O_3. In fact, the interaction of Fe with the oxygen of the topmost Al_2O_3 layer hinders self-surface diffusion and thus the coalescence into large particles [as shown by AFM, see Figure 4.4(a,b)], resulting in a narrow distribution of the islands diameters.

Seidel et al. [16] observed the high CNTs yield on Al_2O_3 not obtainable on SiO_2 & Noda et al. observed the forest growth up to mm long [17] on Al_2O_3, speculating about the possible role of the Al_2O_3 as catalyst in decomposition/de-hydrogenation of the hydrocarbon gas. Al_2O_3 should adsorbs the hydrocarbons, and its derivates should diffuse over the Al_2O_3 surface to the Fe catalyst nanoparticles, where they are incorporated. In contrast, the hydrocarbon gas can be decomposed only on the Fe nanoparticles when using SiO_2 as support. However, as shown in figure 5.4, we didn't observe any signature related to the above phenomenon. We collected the C 1s photoemission peak on the clean Al_2O_3 substrate, after outgassing in UHV for 1h at 600°C (see Appendix A.2.1), and after its exposure to the growth conditions (5 min to C_2H_2 pressure of $8x10^{-5}$ mbar to 580°C). No C 1s intensity increase has been detected (Figure 5.4). In this condition of measurement, we are able to detect carbon up to ~3 nm of depth in Al_2O_3. Therefore we can even exclude also some subsurface inter-diffusion of carbon in Al_2O_3. Same experiment has been performed on SiO_2 substrate and the result was the same. These outcomings indicate that Al_2O_3 does not play any catalytic role in hydrocarbon decomposition.

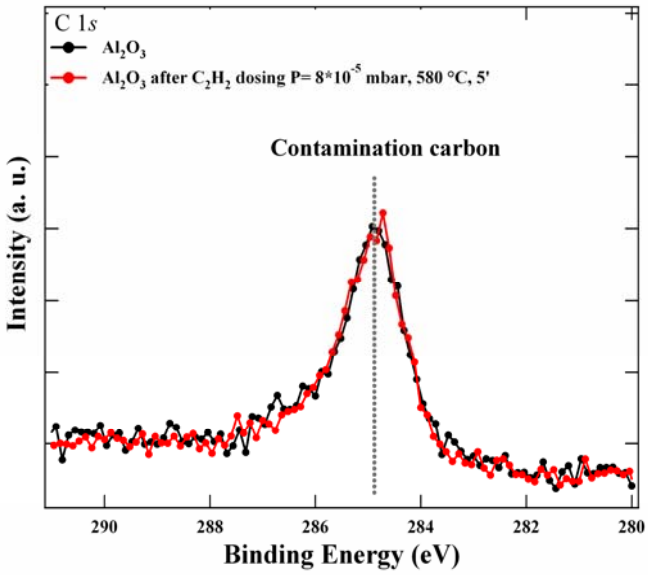

Figure 5.4: *C1s signal (hv= 1253.6 eV) collected on Al_2O_3 substrate .Black spectrum has been collected after Al_2O_3 outgassing in UHV chamber (1h 600°C), the red one has been collected after exposure for 5 min to C_2H_2 pressure of $8x10^{-5}$ mbar to 580°C . Any increase of the intensity of C1s signal has not been found.*

Actually an high dense growth of SWNT bundles, comparable to the one obtained at the same growth conditions on Al_2O_3, has been achieved on SiO_2 by performing a H_2 sputtering treatment of the catalyst layer before the CVD process. Figure 5.5(a) shows the results of the CVD growth done on SiO_2 at the same conditions of the sample grown in Figure 5.5(a). It is evident that the SWNT bundles yield is very similar to that one on Al_2O_3 without any pre-treatment [Figure 5.3(d)]. To obtain this result, the growth process has been performed after a catalyst layer pre treatment consisting in 5 minutes of H_2 sputtering at 580°C (E_{H2}≈200eV). As already discussed in Chapter 4, this kind of treatment may induce chemical and morphological changes in the catalyst layer. In our experimental conditions, we proved (section 4.1.3) that the H_2 sputtering narrows down the catalyst NPs diameters distribution which has a lower mean-value than before the pretreatment (Figure 4.7). Moreover XPS results (Figure 4.6) indicate that the Fe catalyst remains always in metallic state, therefore the formation of Fe-SiO_2 bonds can be ruled out.

However we cannot exclude a chemical effect of the H ions on the catalyst (involving low binding energies), e.g. H chemisorption that can significantly modify the surface energies involved [23]. Chemisorbed species such as H can significantly alter catalyst surface energies [24], leading to temperature- and pressure-dependent catalyst surface reconstruction, thus altering its interaction with C_2H_2. Hydrogen penetration into subsurface layers can loosen the

catalyst surface [24] and may give higher carbon diffusivities during SWNT nucleation. This hypothesis is supported by the growth results obtained by using, in the same conditions, He gas instead of H_2 for the sputtering process. The choice was determined because of He is inert and has an atomic mass close to H_2. Therefore it may help to understand if the H_2 sputtering has some "chemical" effect on the C-Fe interaction or if it only increases the roughness of the surface generating a splitting of Fe islands. Indeed, if H_2 influences only the Fe/SiO_2 roughness we should expect a high CNTs yield also after the He sputtering pre-treatment, since we use the same sputtering conditions and He has similar atomic mass to the hydrogen. Our results show that He sputtering increases the yield of growth on bare SiO_2, but it is definitely lower than the effect of H_2 sputtering [Figure 5.5(b)].

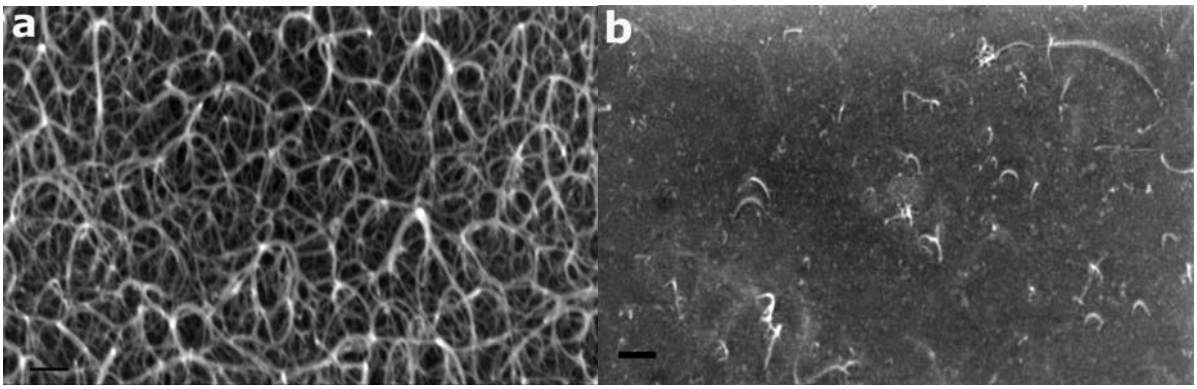

Figure 5.5 *a) SEM images of CVD growth on SiO_2 after H_2 sputtering pre-treatment at 580°C (Δt:5 min., E_{H2}:160eV, p:1x10^{-6} mbar); b) SEM images of CVD growth on SiO_2 after He sputtering pre-treatment at 580°C (Δt:5 min., E_{He}:160eV, p:1x10^{-6} mbar). Both samples have been grown at the same experimental conditions of the sample of Figure 5.3(a, d) [scale bars: (a) (b) 100 nm].*

From the above results, it is clear that the specific substrate-catalyst interaction has a key role in determining the yield/density/direction of the growth CNT. In particular, we found that dense MWNT/SWNT forests (mm-long) can be grown in the furnace on Al_2O_3 spanning a wide range of CVD parameters. We attribute the reason of this different growth result to the significantly different substrate/catalyst interactions occurring on the two surfaces. Actually the CNTs yield can be drastically increased on SiO_2 by performing a catalyst pretreatment by H_2 sputtering. This treatment causes not only a morphological effect, splitting of Fe NPs, but it should have s also chemical effects occurring throughout the heating of the sample, like its chemisorption /physisorption may alter the interaction with C_2H_2. In particular, hydrogen penetration into subsurface layers could loosen the catalyst surface and may give higher carbon diffusivities during C_2H_2 dosing, encouraging the SWNT nucleation [24].

5.3.1. Growth from Fe oxidized

As mentioned in the introduction, there is a controversy about whether Fe oxidized (Fe^{2+} especially) could catalyze growth of CNTs better than metallic Fe [18,21]. To clarify the role of Fe chemical state on the growth, we deliberately oxidized Fe at different degrees exposing to controlled O_2 pressures for different times**.**

At this aim we deposited always the same thickness of Fe (0.5 nm) on Al_2O_3 support in UHV then we heated up the sample to 580 °C at different O_2 pressures (in the range: $8x10^{-8}$-$8x10^{-7}$ mbar) for each substrate for 5 or 8 min to obtain different degrees of oxidation of Fe. After that we collected the Fe 2p signal [Figure 5.6(a)]. Then we exposed the sample at the growth conditions (580°C , C_2H_2 $8x10^{-5}$ mbar, 5min) and collected C 1s and Fe 2p signal. Figure 5.5 shows the Fe 2*p* signal obtained at different O_2 pressures, and Figure 5.6(a) shows one of the two growth results obtained for the sample [black line in Figure 5.6(a)] .We also prepared a Fe layer on 0.5 nm/ Al_2O_3 which was exposed to the air for about 2 months. After that time we observed that the entire Fe layer was completely oxidized, as reported in the reference [25]. Therefore we introduced the sample in the UHV chamber and performed XPS analysis. The Fe 2*p* signal shown characteristic binding energy of complete oxidation Fe (710 eV Fe^{2+}, 711.5 Fe^{3+} [26,27]). Following this analysis, we annealed the sample at 580°C for 5 min *in situ* and Fe was still completely oxidized [by Fe 2*p* signal analysis reported in Figure 5.6(a)]. We exposed the sample to the growth conditions (C_2H_2 $8x10^{-5}$mbar pressure, 580 °C, 5 min) and collected C 1s and Fe 2*p* signal. At the end of the growth all the samples have been characterized by SEM and Raman spectroscopy to detect the presence of CNT. In Figure 5.6(a) shows all the Fe spectra collected after annealing and normalized to the oxygen peak, to be able to compare the different amount of metallic Fe .The spectra shown as continuous line [Figure 5.6(a)] represents the sample from where CNT growth has been obtained, and the spectra reported as dotted line [Figure 5.6(a)] represents the sample from where any tubular form of carbon has not been obtained. Moreover for the sample where no tubes have been grown, showed no increase in C1s intensity and no chemical reduction of Fe as a possible consequence of C_2H_2 cracking . This indicates that Fe oxidized does not interact with C_2H_2. We observed that in the presence of little Fe metallic component together with the oxidized component, high density of CNT can grow [Figure 5.6(b)], whereas no growth occurs when Fe was completely oxidized or the metallic Fe was below the certain threshold (below than green spectrum). None the less there was no increase in C1s peak after the exposure to C_2H_2,

confirming the fact that there is no reaction between oxidized Fe & C_2H_2 at the growth conditions.

In conclusion our experiments completely exclude the possibility of oxidized Fe being involved in catalysis of CNT growth contradicting speculations made in the literature [18,21] about its role in catalysis. Moreover our experiments suggest that, a partial oxidation of Fe on Al_2O_3 support layer does not decrease the yield of growth possibly because of stronger anchor of oxidized Fe to the substrate than pure metallic Fe, preventing the formation of too big islands for the CNT nucleation. Indeed we miss the link as to how Fe oxidized /metallic are distributed morphologically on the surface. It is not clear at this point, how the oxidized and metallic components are distributed in each particle.

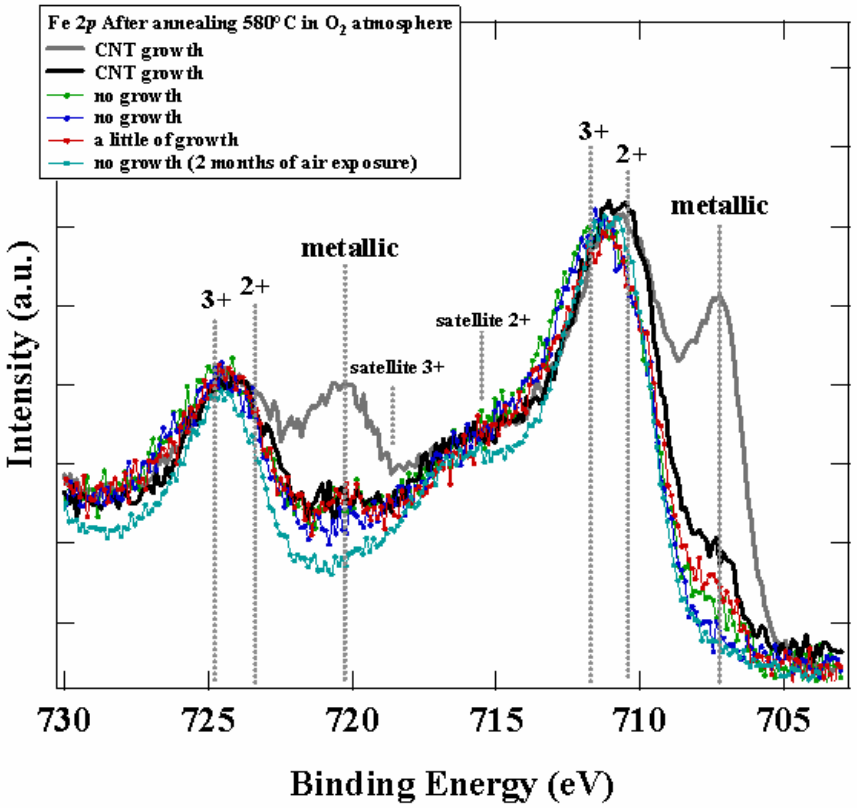

Figure 5.6 *(a)Fe 2p signal from Fe 0.5 nm/Al_2O_3: The gree spectrum has been collected after exposure to 6.5x10^{-8} mbar of O_2, 5' at 580°C, the black one after exposure to 6.5x10^{-8} mbar of O_2,8' at 580°C, the red one after exposure to 1.5x10^{-7} mbar of O_2, 5' at 580°C, the green one after exposure to 1.5x10^{-7} mbar of O_2, 8' at 580°C, the blue one after exposure to 2x10^{-7} mbar of O_2, 8' at 580°C, finally the azure one is the sample keept in the air with Fe deposited over for 2 month and then it has been intreoduced intothe chamber . This spectrum has been collected after 5' at 580°C in UHV.In the label box the growth results for each spctrum are reported.Only the spectra corresponding to the red, gree and balck gave CNT growth.*

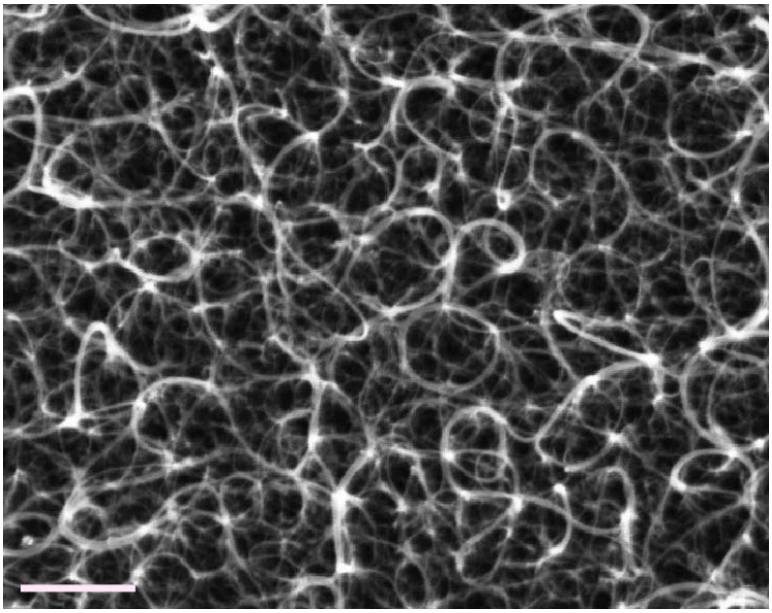

Figure 5.6 (b) *SEM image of the bundled SWNTs grown on the Fe(0.5nm)/Al_2O_3 sample exposed to 6.5x10^{-8} mbar of O_2,8' at 580°C(scale bar 200 nm).*

5.4 CNT CVD growth: pressure dependence

As we reported in the previous chapter, and confirmed by literature [28,29], the strong chemical bond formed between Fe and Al_2O_3 prevents Fe coalescence and decreases the NPs mobility at high temperature (580°C-750°C). In contrast, at the same temperature, the weak interaction between Fe and SiO_2 results in Fe agglomeration into larger islands and in higher metal NPs mobility as compared to Al_2O_3. These finding are confirmed by the NP diameters distributions extracted by TEM analysis after the CVD process.

Figure 5.7(e),(f) shows the HRTEM images of MWNTs grown in the conventional furnace at 750°C at atmospheric pressure (5:2:0.1 Ar:H_2:C_2H_2) for 20 min from 1.1 nm-thick Fe layer deposited onto electron beam transparent membranes covered with Al_2O_3 [Figure 5.7 (e)] and SiO_2 [Figure 5.7(f)] (see Appendix, A1.2 and A2 for more experimental details). Figure 5.7, left refers to the growth performed on a SiO_2 covered transparent membrane, while Figure 5.7, right refers to the growth performed on an Al_2O_3 covered membrane. Even if the Fe coverage is the same in both cases, as verified by a quartz microbalance, the results show a narrower diameter distribution of Fe NPs in the case of Al_2O_3 [centred at ≈5nm Figure 5.7(b)] with respect to SiO_2 [centred at ≈9nm Figure 5.7(a)]. In addition, and in agreement with

literature [30], the corresponding CNT diameter distribution well reproduce the diameters distribution of the catalyst islands, as shown in Figure 5.7(c),(d).

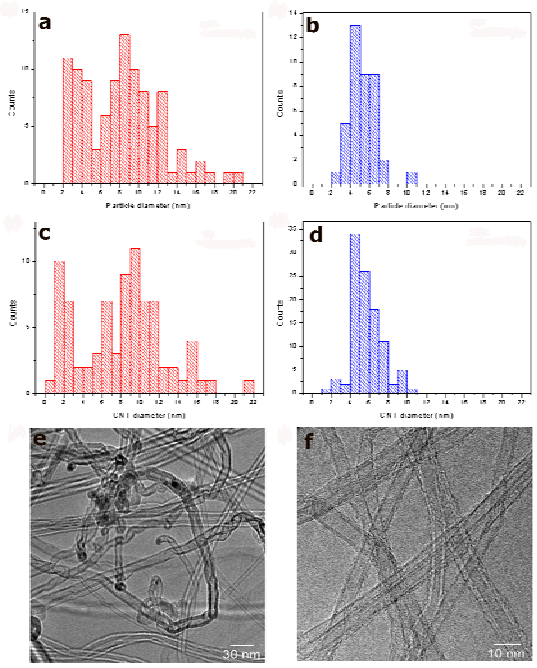

Figure *5.7 (a),(b) Fe NPs diameters distribution after the CVD growth, respectively, on SiO_2 and on Al_2O_3 starting from 1.1 nm-thick Fe layers; (c),(d) CNT diameters distribution grown, respectively, on SiO_2 and on Al_2O_3; (e),(f) HRTEM images of MWNTs grown by CVD in the furnace , respectively, onto SiO_2 and Al_2O_3 layers grown on electron beam transparent membranes.*

Consequently, in the furnace growth conditions, the systematic difference of CNTs yield reflects the catalyst morphology before CNT growth, and it is related with the different interaction existing between Fe and the two supports (see discussion of previous section).

The results of the growth changes significantly when the CVD process is performed at low pressure. In fact we found that the CNT growth at very low pressure ($8x10^{-6}$-$8x10^{-5}$mbar) favors the growth of SWNTs, independently of the substrate and of the initial catalyst NP size distribution. Figure 5.8 shows the HRTEM images of CVD processes done at the same growth temperature on similar substrates, but using a significantly lower growth pressure than in the furnace ($8x10^{-5}$mbar). As before, Figure 5.8 left refers to the growth performed on a SiO_2 covered transparent membrane, while Figure 5.8 right refers to the growth performed on an Al_2O_3 covered membrane. In this case, the Fe coverage was significantly lower than in the previous case (1.1nm vs 0.3-0.7nm), implying smaller NP dimensions, as shown in Figure 5.8(a),(b). We note also that the broader particle distribution observed on Al_2O_3 in this case is due to a higher Fe coverage with respect to SiO_2 (respectively, for Al_2O_3 0.5 nm and 0.3 nm

for SiO_2). Here we did not find a direct correspondence between the catalyst NP diameter distribution and the resulting CNT diameter distribution [Figure 5.8(c),(d)], on the contrary on both surfaces the CVD growth produced only SWNT, which are organized in bundles on the Al_2O_3 substrate and isolated and highly defective on SiO_2, as revealed by the HRTEM images [Figure 5.8(e) for SiO_2;(f),(g) for Al_2O_3]. All the particles with diameter higher than ~ 2.5-3 nm did not nucleate any tubular form. We hypothesize that at low pressure the number of carbon atoms (decomposed from C_2H_2) available for unit of time and area is not sufficient for the MWNT nucleation and therefore only SWNT nucleation can take place, requiring lower feed stock. It is important to remark that this low-pressure growth was not investigated before, and this preliminary result requires more experimental data to achieve a better understanding of this behaviour.

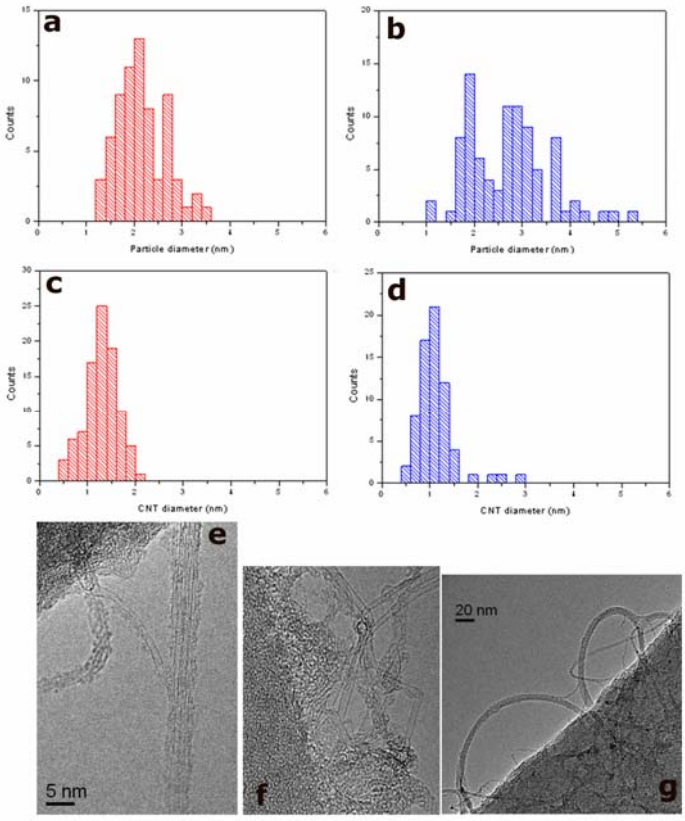

Figure 5.8 *(a),(b) Fe NPs diameters distribution after the CVD growth in UHV chamber, respectively, on SiO_2 and on Al_2O_3 starting from about ~0.7 nm-thick Fe layers for Al_2O_3 and ~0.3 nm for SiO_2; (c),(d) CNT diameters distribution grown, respectively, on SiO_2 and on Al_2O_3; HRTEM images of SWNTs grown onto SiO_2 (e) and onto Al_2O_3 (f),(g) layers grown on electron beam transparent membranes.*

5.5 Conclusions

By performing a systematic study of CNTs growth in different experimental apparatus and by using significant different growth conditions, we found that Al_2O_3 as Fe catalyst support has a crucial role in CNT growth, allowing a drastic increase in CNT density, rate, direction with respect to SiO_2.

In some report in the literature these growth results have been shown, however by performing in situ photoemission studies on the catalyst NPs in UHV environment, we have been able, for the first time, to attribute this experimental result to different Fe-support interactions. Combined XPS-AFM studies (reported in the chapter 4) highlighted a high mobility of Fe on SiO_2, due to a weak Fe-SiO_2 interaction. This is the reason of the formation, at the growth temperature, of islands, whose dimension is too large for the nucleation of SWNTs (particularly important in the case of CNT growth in HV/UHV conditions). Moreover we found a broad distribution of islands diameters, which probably hinders, together with high mobility of the islands during the growth process itself, the vertical growth of CNT on SiO_2. Whereas, we found a barely coarsening phenomenon of the Fe NPs on Al_2O_3, connected with a strong chemical interaction between Fe and Al_2O_3, present since the Fe deposition at RT. In fact, we found that the interaction of Fe with the oxygen of the topmost Al_2O_3 layer hinders self-surface diffusion and thus the coalescence into large particles, resulting in a narrow distribution of the islands diameters.

The CNTs yield can be drastically increased on SiO_2 by performing a catalyst pretreatment with H_2 sputtering. This treatment causes not only the splitting of Fe NPs, but it has also chemical effects, occurring throughout the heating of the sample. A possible explanation could be due to the presence of chemisorbed species, such as H, which may alter the interaction with C_2H_2. In particular, hydrogen penetration into subsurface layers could loosen the catalyst surface and may give higher carbon diffusivities during C_2H_2 dosing, encouraging the SWNT nucleation. In addition, we found that high density of SWNT bundles can grow at very low pressure (up to $8x10^{-6}$mbar), and moreover their nucleation and growth is favoured with respect to the MWNT/CNFs independently from the substrate and the initial catalyst NPs distribution. We are the first group using this low growth pressures, and the selective growth of SWNT vs MWNT, depending on the pressure, has been never observed before. However these are preliminary results, and more experimental data are needed to deeply understand this phenomenon.

We conclude that the use of an Al_2O_3 support (for Fe) favours CNT growth in a wide range of parameters (Fe thickness, catalyst pretreatment's, annealing and growth temperatures, pressure of growth), because of the specific character of its interaction with Fe. As we will show in the next chapter, the role of the support is crucial in the early nucleation of the SWNT, because it influences the reshaping of the catalyst crystal and hence the graphitic lattice-metal dynamics, which is formed at the first stages of growth, and in turn the chiral selectivity.

Bibliography

[1] Saito R., Dresselhaus G., Dresselhaus M.S., *Physical Properties of Carbon Nanotubes*, Imperial College Press, London, (1998).

[2] Choi W.B., Chu J.U., Jeong K.S., Bae E.J., Lee J.W., Kim J.J., Lee J.O., *Appl. Phys. Lett*. 79, 3696 (2001).

[3] Dai L.M., *Smart Mater. Struct*. 11, 645 (2002).

[4] Li J., Ng H.T., Cassell A., Fan W., Chen H., Ye Q., Koehne J., Han J., Meyyappan M., *Nano Lett.* 3, 597 (2003).

[5] Hata K., Futaba D. N., Mizuno K., Namai T., Yumura M., and Iijima S., *Science* 306, 1362 (2004).

[6] Zhang M.,. Atkinson K. R,. Baughman R. H., *Science* 306, 1359 (2006).

[7] Zhang M., Fang S.,. Zakhidov A. A,. Lee S. B., Aliev A.E., Christopher D. W., Atkinson K. R.,. Baughman R. H., *Science* 309, 1215 (2005).

[8] Modi A., Koratkar N., Lass E., Wei B., Ajayan P.M., *Nature* 424, 171 (2003).

[9] Fan S., Chapline M.G., Franklin N.R., Tombler T.W., Cassell A.M., Dai H., *Science* 283, 512 (1999).

[10] Wei B.Q., Vajtai R., Jung Y., Ward J., Zhang R., Ramanath G., Ajayan P.M., *Nature* 416, 495 (2002).

[11] Cantoro M., Hofmann S., Pisana S., Scardaci V., Parvez A., Ducati C., Ferrari A.C.,. Blackburn A. M, Wang K.Y., and Robertson J., *Nano Lett.* 6, 1107 (2006).

[12] Murakami Y., Chiashi S., Miyauchi Y., Hu M., Ogura M., Okubo T., Maruyama S., *Chem. Phys. Lett.* 385, 298 (2004).

[13] Zhong G., Iwasaki T., Honda K., Furukawa Y., Ohdomari I., and Kawarada H., *Jpn. J. Appl. Phys.* 44, 1558 (2005).

[14] Zhang L., Tan Y., and Resasco D. E., *Chem. Phys. Lett*. 422, 198 (2006).

[15] Zhang G., Mann D., Zhang L., Javey A., Li Y., Yenilmez E., Wang Q., McVittie J. P., Nishi Y., J. Gibbons, and H. Dai, *Proc. Natl. Acad. Sci.U.S.A.* 102, 16141 (2005).

[16] Noda S., Hasegawa K., Sugime H., Kakhei K., Zhang Z., Maruyama S., and Yamaguchi Y., *Jpn. J. Appl. Phys.* 46, 399 (2007).

[17] Seidel R., Duesberg G. S., Unger E., Graham A.P., Liebau M., and Kreupl F., *J. Phys. Chem. B*, 108, 1888 (2004).

[18] de los Arcos T., Garnier M.G., Seo J.W., Oelhafen P., Thommen V., Mathys D., *J. Phys. Chem. B* 108, 7728 (2004).

[19] Zhang L., Tan Y., Resasco D. E., *Chem. Phys. Lett.* 422, 198 (2006).

[20] Prabhakaran K., Watanabe Y., Homma Y., Ogino T., Wei B. Q., Ajayan P. M., Kurikka V. P., Shafi M., Ulman A., Heun S., Locatelli A., and Cherifi S., *Langmuir* 19, 35223 (2003).

[21] de los Arcos T., Oelhafen P., Thommen V., Mathys D., *J. Phys. Chem. C* 111,16392 (2007).

[22] A. Jiang, N. Awasthi, A. N. Kolmogorov, W. Setyawan, A. Börjesson, K. Bolton, A. R. Harutyunyan, and S. Curtarolo, *Phys. Rev. B* 75, 205426 (2007).

[23] W. F. Egelhoff, D. A. Steigerwald, *J. Vac. Sci. Technol*. A 7, 2167 (1989).

[24] Paal Z., Menon P.G., *Hydrogen Effects in Catalysis*; Dekker: New York, (1988).

[25] Wang C.M., Baer D. R., Thomas L. E., Amonette J. E., Antony J. , Qiang Y., Duscher G.,*J. Appl. Phys*. 98, 94308 (2005).

[26] Mills P., Sullivan J.L. , *J. Phys. D.* 16, 723 (1983) .

[27] Konno H., Nagayama M., *J.Electron Spectrosc. Relat. Phenom*. 18, 341 (1980).

[28] Arranz A., Perez-Dieste V., Palacio C., *Surf. Sci.* 521, 77 (2002).

[29] Colaianni M.L., Chen P.J., Yates J.T., *Surf. Sci*. 238, 13 (1990).

[30] Helveg S., Lopez-Cartes C., Sehested J., Hansen P. L., Clausen B. S., Rostrup-Nielsen J. R., Abild-Pedersen F., Norskov J. K., *Nature* 427, 426 (2004).

Chapter 6

Dynamics of Carbon bond formation during the growth of SWNT/CNF

In the present chapter we present our real-time TEM and XPS data acquired during the CVD growth of CNTs. We remark that this is the first real-time XPS study appeared in the literature and only few real-time TEM investigations are already present, even if the applications of these techniques for the study of CNT growth can give an important contribution to understand the mechanism of CNTs nucleation and can help to find the optimized conditions to grow CNTs with peculiar features (i.e. chirality, tube diameters, length, etc).

After a short introduction (section 6.1) about the importance of this work, we present the results obtained by real time Environmental Electron transmission Microscopy and XPS (section 6.2) and XPS data obtained at the end of the growth (section 6.3).

6.1. Introduction

Existing models of catalytic nucleation rely heavily on the quality of direct experimental observation. SWNT nucleation during high-temperature arc-discharge and laser ablation processes is difficult to monitor *in situ* [1] because of the high temperatures and the short time-scale involved.

So far, most of the experimental evidence for SWNT formation from condensed catalyst particles arises from post-growth high-resolution transmission electron microscopy (HRTEM) [2]. Presently, CVD is increasingly important for applications [3] because it allows the controlled, selective growth of CNTs directly on a substrate as well as bulk production [4]. In addition, it is enables the direct observation of the catalytic nucleation process at the atomic scale [5,6].

Previous *ex situ* characterization of CVD growth suggests that a CNT grows by carbon extrusion, [7] i.e., that CNT growth is fed solely via the catalyst particle interface. Post-growth HRTEM analysis typically finds the SWNT wall aligned tangential to the catalyst cluster, whereby the catalyst particle appears to have dictated the tube diameter [8,9]. However, such post-growth characterization is static and can be ambiguous due to changes during cooling and transfer. This leaves key questions such as how the CNTCNTs nucleate and whether the catalyst is liquid or solid difficult to answer.

In the following paragraphs we present atomic-scale, video-rate ETEM and *in situ* time-resolved XPS of catalytic CVD of SWNT and CNF. We found that SWNT nucleates at C_2H_2 pressures below 10^{-6} mbar, which allows a time-resolved recording of core level photoemission spectra. From real-time TEM, we observe that the transition metal catalyst NPs on SiO_2 support show crystalline lattice fringe contrast and high deformability before and during CNTCNT formation. A SWNT nucleates by lift-off of a carbon cap. Cap stabilization and CNTCNT growth involve the dynamic reshaping of the catalyst nanocrystal itself. For a carbon nanofiber, the graphene layer stacking is determined by the successive elongation and contraction of the catalyst NP at its tip.

By *in-situ* XPS measurements, realized while dosing C_2H_2, we find a rapid transition from an initial chemisorbed carbon on metallic Fe catalyst NPs to a sp^2 graphitic carbon network. The above process undergoes through the formation of an intermediate carbidic stage, which is still visible, albeit attenuated, until the end of the growth.

By XPS analysis, done after dense growth of SWNT on Al_2O_3, we observed the presence of a weak carbidic peak, together with the graphitic one. The origin of the carbidic phase is a discussed point in the literature. In particular it is not clear whether it comes from the NPs which drive the growth of a CNT, or whether from the NPs which did not nucleate CNT, or whether it is just surface-subsurface phase, or involves the entire bulk of the nanoparticels, or finally whether it is just a temporary state for the NPs bound to CNT and it is permanent state for the no reacted ones.

6.2 *In situ* Observations of Catalyst Dynamics during Surface-Bound CNT Nucleation

We focus on C_2H_2 decomposition over SiO_2-supported Ni and Fe catalyst films. It is important that the gases and pressures during ETEM observations are similar to those used in normal CVD experiments [10,11] so that we can draw realistic conclusions about what determines structural selectivity (for the experimental details, see the Appendix A5.1.).
As already described (see chapter 3 and Appendix A2), the overall CVD growth process consists of two steps, a catalyst pretreatment step followed by a CNTCNT growth step. In step 1, the initial thin film catalyst is transformed by dewetting from the SiO_2 into a series of isolated NPs (Figure 6.1). It is known that dewetting initiates at grain boundaries and edges through surface diffusion and that the metal thereby can remain crystalline [12,13]. The film restructuring, further sintering, and the crystal shape [14] reflect a surface and interface energy minimization. A reactive ambient can change the chemical state of the catalyst and influence its shape via adsorbate-induced changes of surface energies and changes of the interfacial energy [14], hence the catalyst particle shape and size distribution are related intimately to the CVD conditions used [15,16.]

Our HRTEM analysis shows that Ni (Figure 6.1) and Fe [Figure 6.2 (a),(b)] NPs are crystalline during the pretreatment step before CNF [Figure 6.1(a),(c) 480 °C in 1 mbar NH_3 on an SiO_2membrane], and SWNT growth [Figure 6.1(b),(d) at respectively 450 °C and 615 °C in vacuum ,10^{-6} mbar on SiO_2 membrane].A nominally 1 nm thick catalyst film typically transforms into an island size distribution centered around 5nm, [15,17] which is broadened considerably here by the non planarity of the TEM-compatible substrates. For most nanocrystals, only one set of lattice fringes is visible, which can make the analysis of their

chemical state solely based on lattice assignments ambiguous. The 0.20 nm reflection is expected for metallic fcc Ni(111), but also for Ni_2O_3(200) and Ni_3C(113). We therefore we performed XPS as discussed later, to follow changes in the chemistry related to the particle. It should be noted that in the real time ETEM measurements, the initial Ni films were (partially) oxidized due to transfer in air. For the real time ETEM measurements the Fe and Ni deposition have been performed *ex situ* (see for the deposition details Appendix 2.2). It appears that some of the Ni nanocrystals that are held at 480 °C in NH_3 are still oxidized, as the 0.21 ± 0.01 nm spacing can best be assigned to (200) lattice planes in NiO(0.208 nm) [Figure 6.1(c)].

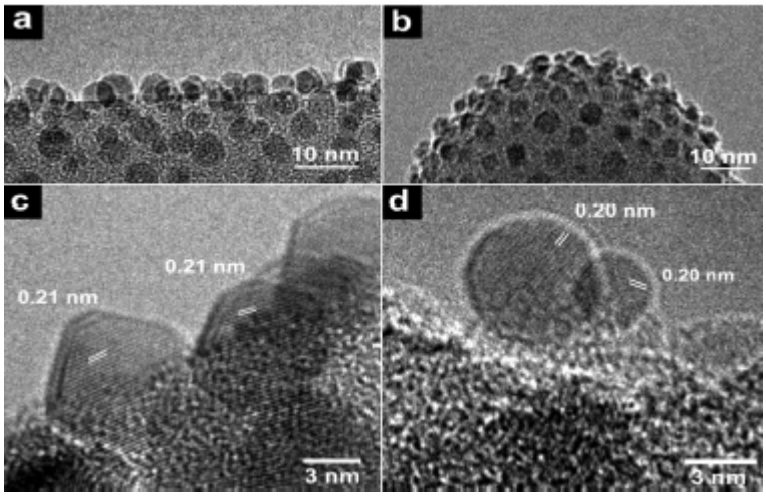

Figure 6.1 *ETEM images of an initially (partially) oxidized 1 nm Ni film recorded at (a,c) 480 °C in 1 mbar* NH_3 *on an* SiO_2 *membrane, (b) 450 °C, and (d) 615 °C in vacuum (10-6 mbar) on an* SiO_2*-covered silica NP.*

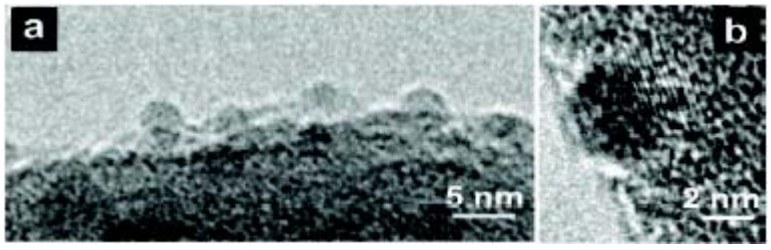

Figure 6.2 *(a,b) ETEM images of an initially oxidized 0.3 nm Fe film at 480 °C in 1 mbar* NH_3 *on an* SiO_2*-covered silica NP*

This observation would also be consistent with the faceting, although we cannot comment on NH_3-induced restructuring. In addition, measurements of lattice spacings from nanocrystals may be affected both by their finite size and rapid variation in thickness and by variations in their orientation [18] . XPS reveals that the Fe and Ni 3p core levels of UHV-deposited Fe and Ni remain metallic (Figure 6.3) during the pre treatment step as expected from the results shown in the previous chapter. Figure 6.3 shows the Fe3p core level signals recorded after every step of the CVD on 0.5 nm Fe layer. The Fe peak is centered at the binding energy of 52.8 eV which is compatible with the metallic chemical state [19]. After annealing in UHV at 580°C the intensity of the Fe 3p signal decrease for more than ~40%. This is an indication of the transition from a thin film to islands of Fe as we shown in the section 4.1.3. After the hydrogen ion-sputtering the intensity still the same like after the annealing step. We interpret this with a no relevable changes of the Fe islands dimension, probably due to the lower efficiency of the sputter gun used in this experiment with respect to that one used in the analogous experiment realized in TASC Laboratory (section 4.1.3). Finally after the growth the Fe intensity spectrum decreases as consequence of the carbon covering. All these Fe3p curves are at the same binding energy, which is compatible with metallic chemical state and they don't show other components.After the growth we were not able to detect the presence of iron carbide (whereas it is evident from C 1s core level signal), since there is no chemical shift in the Fe core levels.

Now we turn to the real time XPS data discussion of the CNT growth step. CNTs were nucleated by exposing 0.5 nm thick Fe layer, deposited SiO_2/Si *in situ* to undiluted C_2H_2 ($2x10^{-7}$ mbar)at 580 °C for 5 min. Figure 6.4(b) shows the evolution of the C 1s core level photoemission spectrum during C_2H_2 exposure at a pressure of $2x\ 0^{-7}$ mbar (see appendix A5.2 for more experimental details). The acquisition time for each spectrum was 15 sec, and we followed the evolution of the C1s core level peak during all the exposure time to C_2H_2**.**

No carbon contamination was detectable before growing. In addition, no C 1*s* peak was detected exposing the SiO_2 surface where the Fe catalyst was not present to C_2H_2 gas at high temperature, thus we can rule out any possible interaction between C_2H_2 and the SiO_2 surface in our experimental conditions.

The SEM picture of the as-grown sample, on which we collected the temporal sequence of spectra, is shown in Figure 6.4(a).

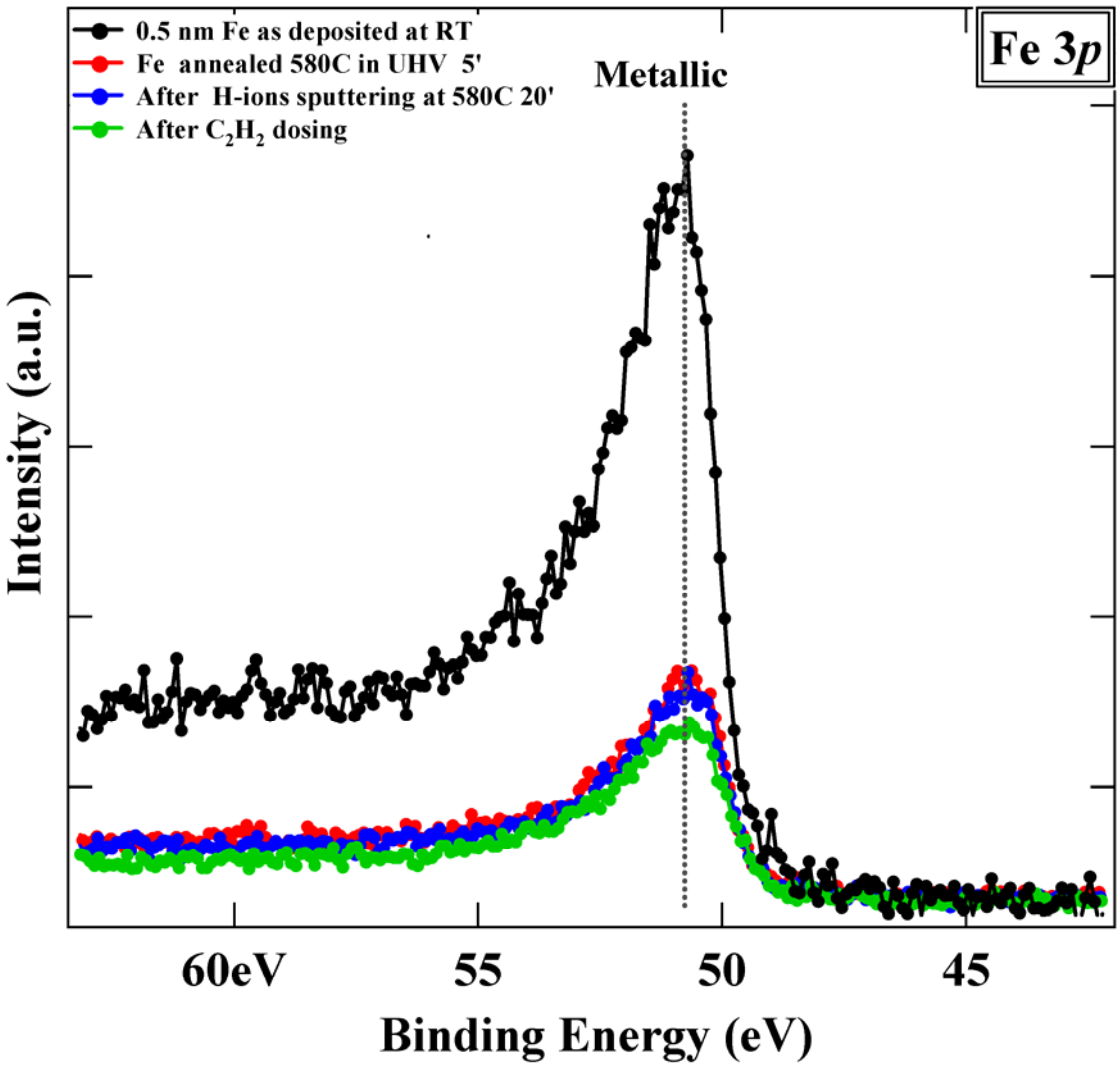

Figure 6.3 *Fe 3p photoemission spectra (hv=400 eV) acquired after every step of the CVD process. The black line represent the spectrum collect immediately after deposition in situ of 0.5 nm-thick Fe film on SiO_2/Si substrates, the blue line represent the spectrum collect immediately after annealing in UHV for 5 min at 580 °C, the red line represent the spectrum collect immediately after exposure at H_2 sputtering (20 min) at 580 °C, finally the green line represent the spectrum collect after the growth. All spectra are normalized to the photon flux.*

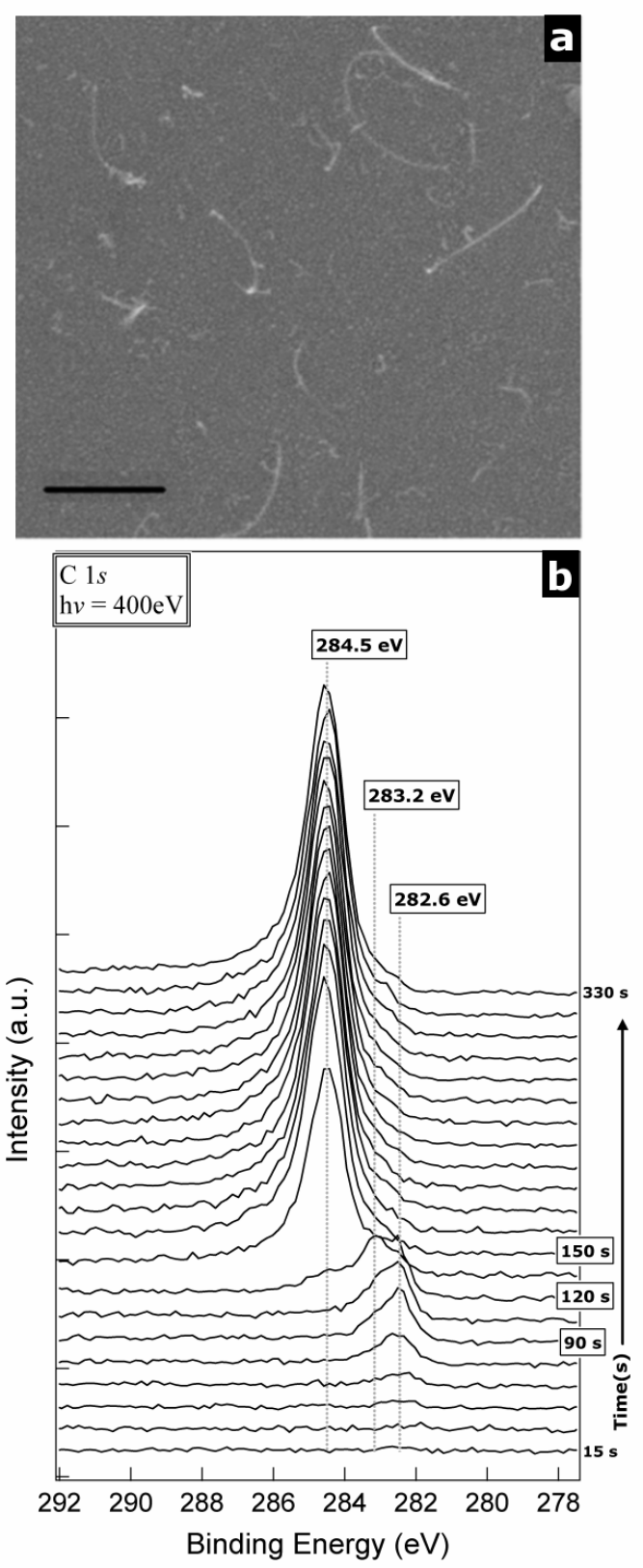

Figure 6.4*(a) Time-resolved evolution of C 1s core level during Fe exposure to 2x 10^{-7} mbar (background pressure)* C_2H_2 *at 580℃.(b) show an SEM image of part of the probed area (scale bar 200 nm)*

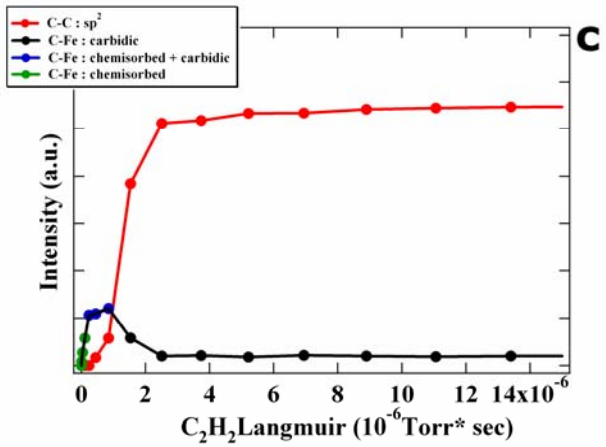

Figure 6.4(c) *shows the Intensity of the different carbon 1s signals versus the* C_2H_2 *dose of exposure. The evolution of C 1s peaks during the* C_2H_2 *dosing (Langmuir) shows a rapid transition from an initial chemisorbed carbon on metallic Fe catalyst NPs to a* sp^2 *graphitic carbon network*

The carbon 1s peak dynamics can be described as follows [Figure6.4(c)]: as soon as C_2H_2 is let into the chamber, a peak at 282.6 eV appears, indicating that C is chemisorbed on the Fe catalyst [20,21]. After 90 s incubation, another peak at 283.2 eV appears, persisting for 30 s. We attribute this peak to the formation of carbidic C [20,22.]. Our data indicate that the chemisorbed C state persists up to 25% C concentration. At higher concentrations, the C-Fe bond changes, and the carbidic C signature at 283.2 eV appears. The formation of a sp^2, graphitic C network is detected by the appearance of another peak at 284.5 eV (corresponding to the typical C 1s binding energy of the C-C bond) [20,23]. The intensity of the latter peak increases very rapidly: after 15 s, the chemisorbed C and carbidic C peaks drastically reduce. The graphitic peak saturates after 150 s, suggesting a termination of CNT growth, and it dominates over the chemisorbed C and carbidic C peaks. The carbidic peak remains until the stop of the gas even if it is barely visible. In literature, a binding energy of 282.6 eV, measured by XPS on the surface of Fe single crystals annealed at high temperatures, was attributed to chemisorbed C [20,21]. In Ref. [21], chemisorbed C of sub-monolayer thickness was measured after sample heating up to temperatures in the 377–577°C range. In Ref. [20], the Fe sample was heated at temperatures between 450 and 700°C, obtaining again sub-monolayer-thick chemisorbed C or graphitic C on the metal surface as separate phases, reversibly transformed into each other under specific annealing conditions. We thus use Ref. [20] to define the reference binding energies for chemisorbed C and graphitic C, since they characterized by XPS a system similar to ours (carbon bonded to Fe). At the conditions used

here, the XPS information depth is ~ 0.8 nm, hence the attenuation of the chemisorbed peak in Figure 6.4(b) may result from increased carbon network formation. We could not detect a carbon signal after CVD process on the plain SiO_2 substrate under our conditions, indicating a highly selective C_2H_2 decomposition on the metal catalyst . Due also to the small catalyst cluster dimension (~1-3nm for SWNT), the XPS data does not allow a clear distinction between surface carbide [24] (carbon-rich (sub)surface layer) and bulk catalyst carbide formation [25].

To have more information about the carbon structures on which we collected the temporal serial of C 1s peak, we realized Raman spectroscopy measurements. Raman spectroscopy is a fast and non-destructive method for characterization of carbon materials [26]. In the case of SWNTs, important information such as diameter, orientation, metallic or semiconducting character and chirality, can be obtained from this experimental technique [27]. Figure 6.5 shows a Raman spectrum (633 nm) of the sample shown in Figure 6.4. We observe a structured G peak at ~1600 cm^{-1}, typical of CNTs [26-31], and the D peak at ~1300 cm^{-1}, indicative of defects and disordered graphitic material [26]. The presence of well defined Radial Breathing Modes (RBMs) in the low frequency range (inset of Figure 6.5), together with the shape of the G peak, is the typical signature of SWNTs [27,28]. SWNT diameters (corresponding to the RBMs observed) can be calculated using $d=C_1/(\omega_{RBM}-C_2)$, with C_1=214.4 nm cm^{-1} and C_2=18.7 cm^{-1} [29], resulting in a 0.8–1.3 nm diameter distribution. Due to the cut-off of our notch filter, we cannot detect SWNT diameters >2 nm.

It is interesting to note that the time evolution observed for the chemisorbed and graphitic C peaks [Figure 6.4(b)(c)] is similar to reported SWNT incubation times extrapolated for low-pressure C_2H_2 exposure of Ni [6]. We also note that in the latter study electron diffraction indicated the absence of bulk Ni_3C during SWNT growth [6]. Carbidic carbon has been reported previously as the single remaining species following temperature-programmed C_2H_2 and C_2H_4 decomposition on Ni [32].

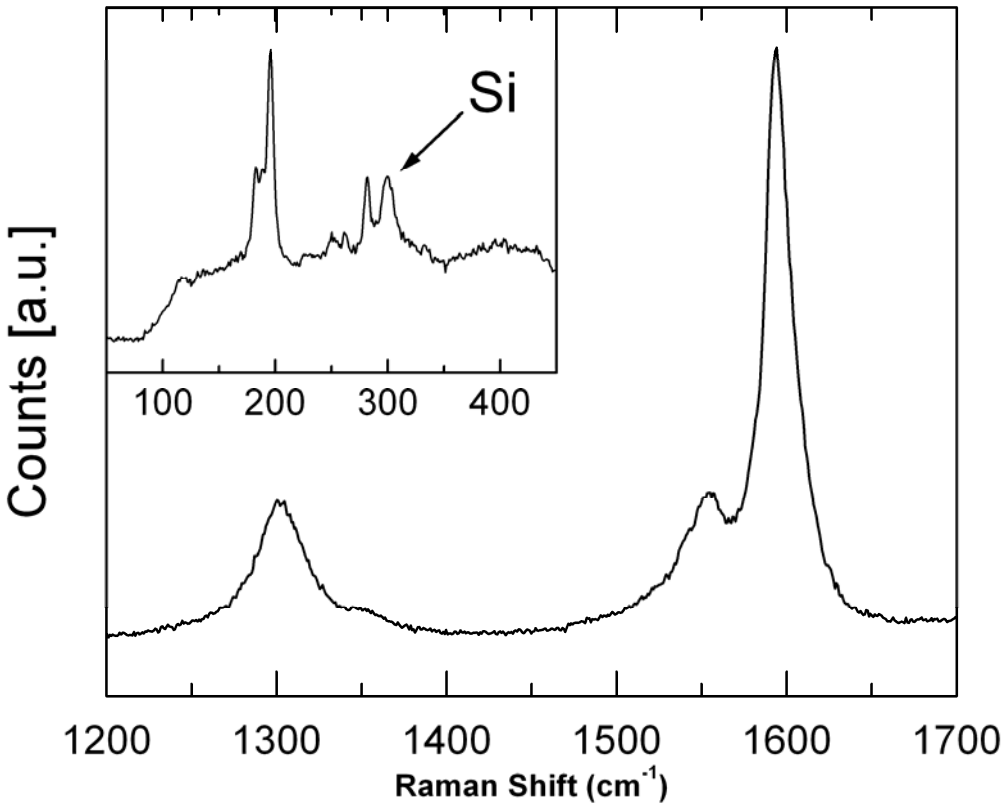

Figure 6.5 *Raman spectra of two CNT samples grown in the SuperESCA chamber. The Sample is that depicted in Figure 6.3(a).*

ETEM shows that the core of a Ni catalyst NP remains crystalline during the continuous exothermic C_2H_2 dissociation and carbon network formation (Figure 6.6). The 0.18 nm lattice spacing observed in Figure 6.6(a) can be assigned to (200) lattice planes in metallic Ni. During CNF nucleation, the catalyst particle transforms from its initial equilibrium shape (Figure 6.7) into a highly elongated shape. ETEM videos show that the Ni particle elongates until it suddenly contracts into a rounder shape, and the sequence recurs (Figure 6.7). Typically, the substrate anchorage is overcome during the first contraction and the catalyst crystal lifts off the substrate, resulting in a tip growth mode .

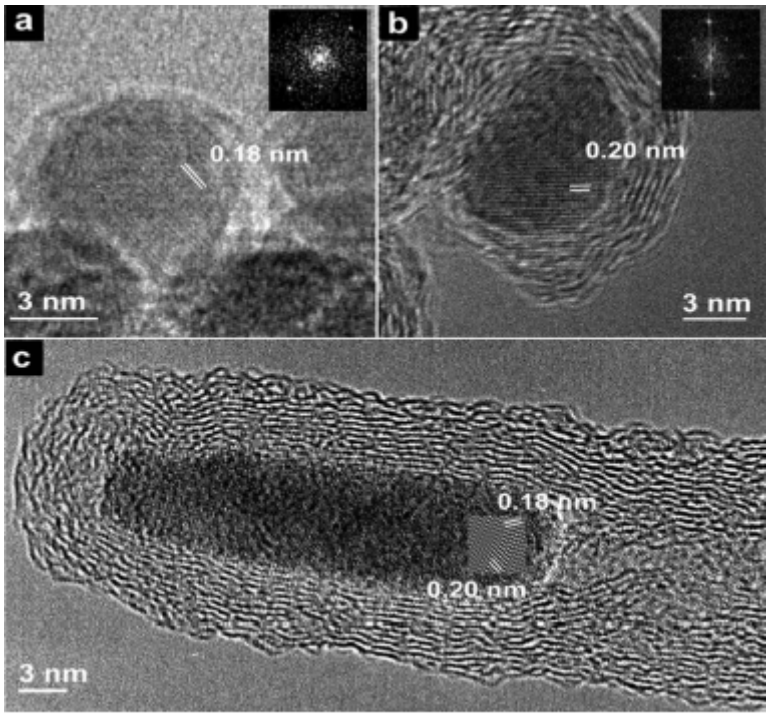

Figure 6.6 *ETEM images of Ni nanocrystals recorded at (a) 480℃ and (b) 360℃ in 3:1 NH_3: C_2H_2 at 1.3 mbar total pressure. The insets show FFTs of the respective particles. (c) HRTEM image of the tip region of a Ni-catalyzed CNF grown ex situ at 700℃ in 2.7:1 NH_3: C_2H_2 at 5.2 mbar total pressure. The fcc Ni particle is imaged in the [110] projection. The inset shows a Fourier-filtered image of the lattice.*

The Ni catalyst behaves in an apparent "liquid-like" fashion analogous to the observations for solid-state dewetting (Figure 6.1) [13]. In this context, "liquid-like" denotes that the Ni exhibits fast self-diffusivity but shows long-range crystalline order, in contrast to real liquids. Dynamic coexistence is typically observed for NPs less than 2 nm in size, [33] thus mainly relevant for small-diameter SWNT nucleation. Carbon layers terminate at a stepped Ni surface, which is analyzed in more detail in Figure 6.7(a). The Ni fcc lattice is seen in a [110] projection. The corresponding ball-and-stick model [Figure 6.7(b)] shows Ni steps 3-4 monolayers in height, with graphitic layers emerging at various angles. Subsequent graphitic layers nucleate at an already-grown Ni-C interface. Such C-stabilized Ni step-edges are often not in direct contact with the CVD atmosphere, i.e., are not at the same time the active sites for C_2H_2 dissociation. Thus the process involves diffusion of C atoms toward and Ni atoms away from the graphitic layer-Ni interface [5] This Ni flux contributes to the observed elongation of the Ni catalyst crystal. The dynamics of the Ni crystal reshaping (Figure 6.7) are essential for the alignment of the graphitic layers into a CNF rather than a

carbon onion [Figure 6.6(b)]. For a bamboo-structured CNF, the Ni particle elongation is followed by an abrupt contraction, which leaves a conformal carbon overcoat behind and thereby creates the characteristic bamboo-like intersects (Figure 6.7). The time at which a contraction occurs has been attributed to the point at which the increase in Ni surface energy can no longer be compensated by the energy gain of binding the graphitic fiber to the Ni surface [5]. A more continuous elongation/contraction of a catalyst particle with a wedge-shaped tail will lead to a herringbone-like CNF crystallinity. A tangential extrusion of graphene layers without the carbon (re)coating of the catalyst particle tail will result in the formation of a hollow MWNT. An analysis of such dynamical behaviour at the nanoscale requires further modeling, as many bulk properties appear to distinctively change. We also find that splitting of the catalyst particle can lead to CNF branching or to encapsulation of catalyst metal along the CNF body (data not shown). For the given CNF CVD conditions, defect incorporation and disordering are frequently observed. The carbon arrival rate appears to be too high compared to the defect repair rate to effectively anneal out defects while they are still near the growth front. The resulting defective C network in turn influences the catalyst particle dynamics, possibly leading to a further propagation of defects in the growing CNF structure. It should be noted that the stepped Ni-C interface (Figure 6.8) can extend asymmetrically around the Ni particle, leading to incomplete closure of graphitic C sheets. As it is known from HOPG [34], open-ended graphene layers are stable during formation if the carbon dangling bonds can be saturated, e.g., by hydrogen.

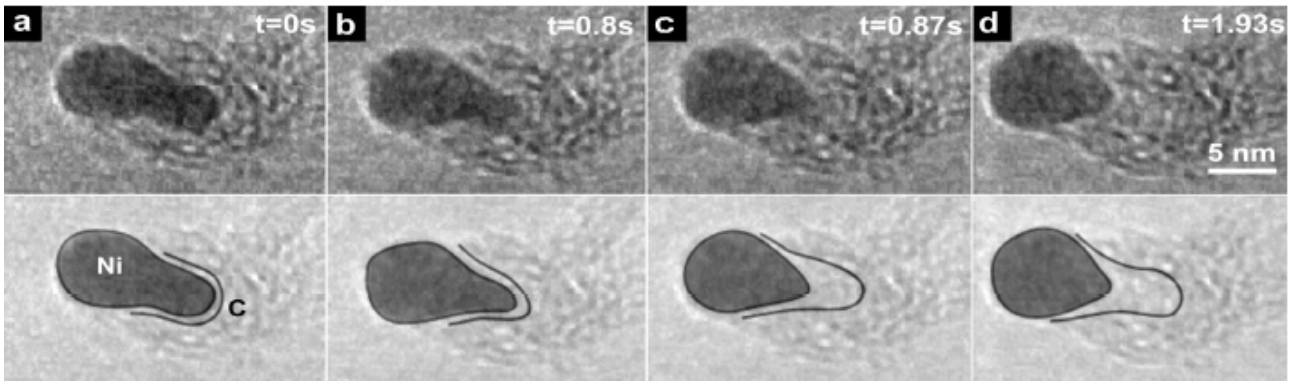

Figure 6.7 *(a-d) ETEM image sequence showing a growing CNF in 3:1 NH_3: C_2H_2 at 1.3 mbar and 480°C. The video was recorded at 30 frames/s, and the time of the respective stills is indicated. Drawings (lower row) indicate schematically the Ni catalyst deformation and C-Ni interface.*

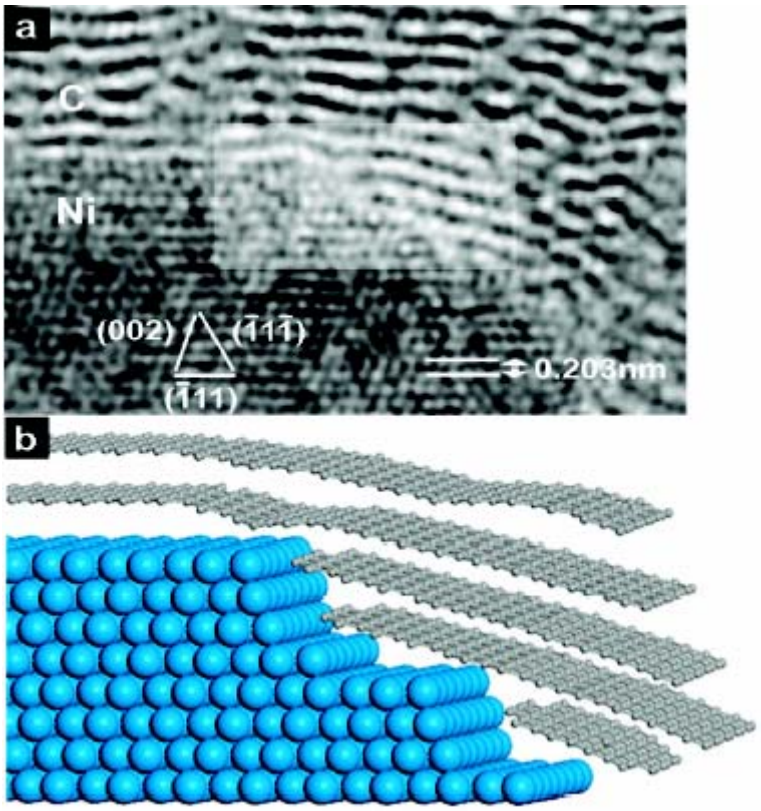

Figure 6.8 *(a) HRTEM image of Ni-C interface at the tip of a CNF grown ex situ at 700°C in 2.7:1 NH_3: C_2H_2 at 5.2 mbar total pressure. The principal planes of the Ni crystal in the [110] projection are indicated. (b) Schematic ball-and-stick model of area highlighted in (a).*

Electron energy loss spectroscopy (EELS) shows nitrogen incorporation for CNFs grown in NH_3 (data not shown [35]). This suggests that the role of reactive CVD gases has to be discussed in terms of changes to the chemical state of the catalyst particle and its surface energy combined with the effects on feedstock dissociation, carbon diffusion, and graphitic C formation. It is obvious that most of these processes are pressure and temperature dependent. Carbon reactivity drives the dynamic restructuring of the catalyst, which determines structural selectivity. CNT growth ceases when the reciprocal Ni-C interaction is interrupted, i.e., when catalyst particle elongation is suppressed and the Ni surface becomes encapsulated by carbon. Figures 6.9 and 6.10 show ETEM and HRTEM data of various stages of SWNT growth.

In contrast to CNF nucleation conditions, we anneal the 1 nm thick Ni film in vacuum to ~ 615 °C [Figure 6.1(d)] and expose it to undiluted C_2H_2 at lower pressures. The ETEM images in Figure 6.9(a),(b) show Ni crystals for which SWNT nucleation has stopped early. A small-sized carbon cap has emerged on top of each catalyst particle. The carbon network surrounding the deactivated Ni particle forces a stronger faceting. Clear crystalline lattice

fringe contrast is visible in the Ni clusters held at ~615°C. We assign the strong reflections in the FFT of Figure 6.9(b) to {111} planes, with the fcc Ni lattice oriented close to the [110] axis. Ex situ HRTEM imaging of SWNTs at a more progressed stage of growth shows the graphitic lattice of a hemispherically capped tube oriented tangentially to the catalyst cluster [Figure 6.9(c)], which is a very common observation [8] despite larger diameter SWNTs reportedly tending to have cone shaped caps [9]

Parts a-c of Figure 6.10 show an ETEM image sequence. We believe that this sequence is representative of SWNT base growth, even though the CNT is defective and growth terminates quickly. The Ni catalyst crystal strongly reshapes on its SiO_2 support, which explains the previous static observations of the various growth stages (Figure 6.9). Initially, a carbon cap emerges with a diameter smaller than the catalyst cluster. The carbon cap appears to replicate the shape of the apex of the triangular/pyramidal metal particle. The carbon network expands by lifting off from the catalyst particle, which itself is thereby restructured. The growing CNT forces its shape onto the Ni cluster. The contact angle of the Ni particle to the SiO_2 substrate increases to approximately 90°, whereby the CNT constrains the Ni particle to a more cylindrical shape. Growth terminates when the tangential graphitic lattice encapsulates the catalyst particle down to its support interface. The highly idealized ball-and-stick models shown in Figure 6.10(d-f) summarize the different SWNT growth stages. It has been previously suggested that step sites on the catalyst surface nucleate the graphitic lattice formation [5] and that the carbon cap of a SWNT is stabilized by the fact that carbon precipitation is faster than the speed of step withdrawal [9]. Our data suggests that the "cap-finding" process of a SWNT involves the dynamic reshaping of the catalyst crystal itself. This is very important, as the initial cap uniquely determines the chirality of the CNT that will grow out of it [36]. It should be noted that this holds only for hemispherical caps; for cone-shaped caps, the SWNT chirality depends on the introduction of a further pentagon. We suggest that chiral selectivity may be related dynamically to catalyst particle-carbon network interactions.

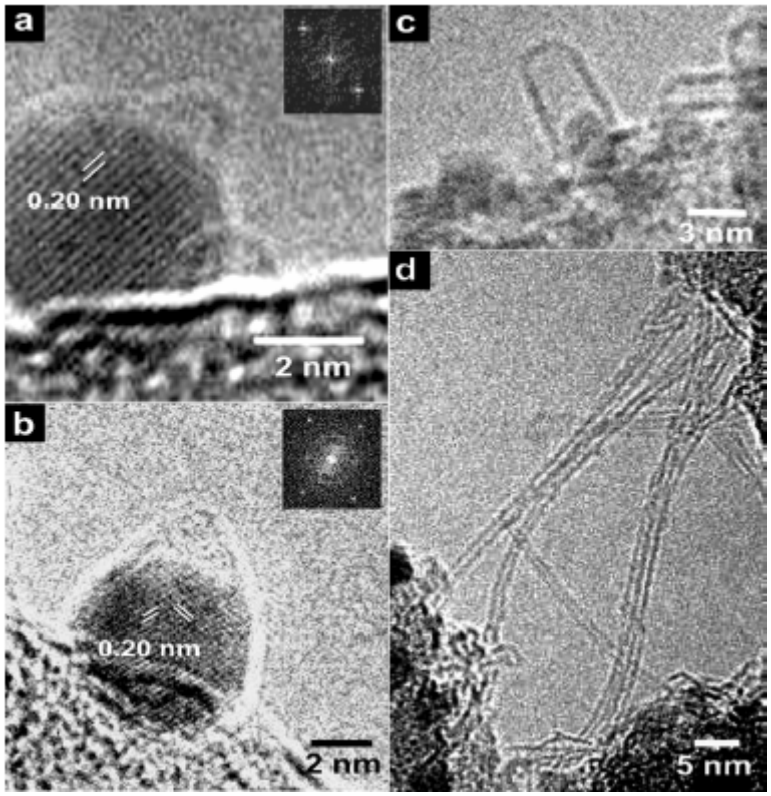

Figure 6.9 *(a,b) ETEM images of Ni nanocrystals (Figure 6.1d) recorded at 615 °C in 8 x 10^{-3} mbar C_2H_2. The insets show FFTs of the respective particles. (c,d) Ex situ HRTEM images acquired from the same samples.*

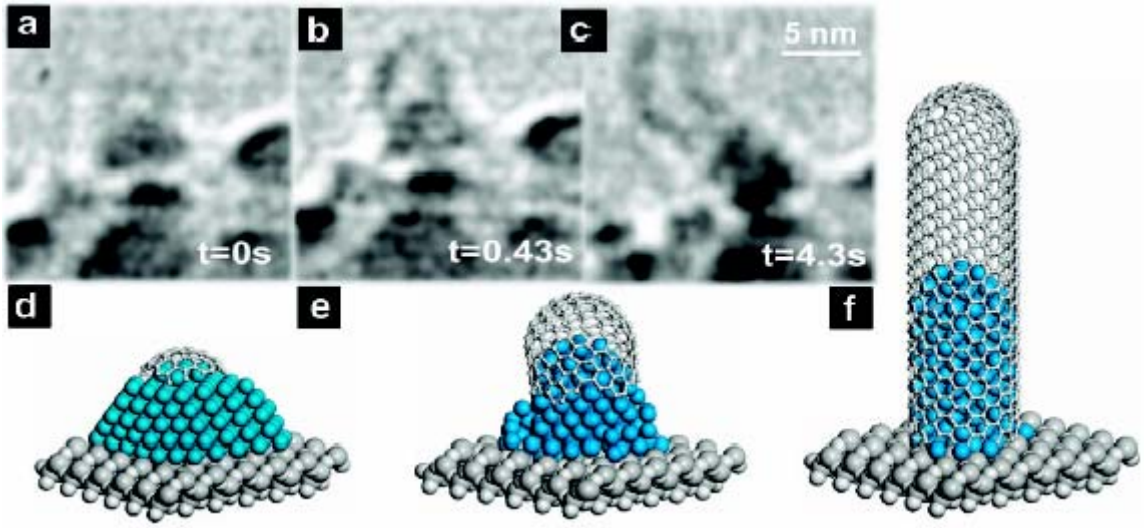

Figure 6.10 *(a-c) ETEM image sequence of Ni-catalyzed CNT root growth recorded in 8 x 10^{-3} mbar C_2H_2 at 615 °C . The time of the respective stills is indicated. (d-f) Schematic ball-and-stick model of different SWNT growth stages.*

For high-temperature arc-discharge and laser ablation techniques, gas-phase-based SWNT nucleation is often observed perpendicular to the catalyst surface, with multiple SWNTs emerging from large catalyst particles [2,37]. Figure 6.9 shows that, at our CVD conditions, a catalyst crystal only nucleates one SWNT, whereby the metal particle size and dynamics determine the SWNT diameter. Cap diameters below 0.72 nm require the formation of adjacent pentagons and have a high curvature energy [36]. Thus it is unlikely that a small, highly deformable catalyst particle can nucleate such a CNT diameter (irrespective of structural and chemical changes for such small metal clusters). Catalyst particles larger than 2 nm were observed to have predominantly cone-shaped caps [9]; we suggest the graphitic cone reshapes the catalyst particle, and the transition to CNT growth occurs when the cone opening matches the new catalyst dimensions. The nucleation of SWNT diameters over 5 nm requires the deformation of increasingly larger catalyst particles, whereby the surface curvature becomes unfavourable for a carbon cap lift-off. Large catalyst particles end up encapsulated with carbon, which is a common observation for CVD [4].

It has been shown that the SWNT chirality distribution can be influenced by careful catalyst engineering [16] The main effect of an increase in CVD temperature is typically an increase in catalyst particle size and hence larger CNT diameter [11,16,38].

The gaseous feed composition can influence the rate of carbon deposition and thus indirectly affect the SWNT diameter based on a different catalyst island agglomeration time before the carbon cap stabilizes [16]. The detailed topography of catalyst particles depends strongly on the support and gas exposure [14] (Figure 6.1), and the resulting effect on chiral selectivity for a given SWNT diameter was previously discussed in terms of a matching carbon cap [16,38].

We emphasize that chiral selectivity is related to the graphitic lattice-metal dynamics, of which the initial catalyst crystal shape is only the starting point. The support influences the induced reshaping (Figure 6.10) and hence also the kinetics of carbon cap formation. For prolonged growth, in particular if not suspended, the SWNT body exerts an increasing moment on the growth interface that can lead to defect formation and growth interruption.

6.3 Monitoring of the Carbon 1s signal *in situ* at the end of the growth

As we mentioned in the chapter 2, there is a debate whether the carbon diffuse through the catalyst NP to form the CNT or the carbon diffusion is only on the surface and subsurface of the catalyst particle. In the first case we could expect to have at the end of the growth the presence of Fe-C bonds in the catalyst NPs. Since the most stable alloy Fe-C is the carbide (Fe_3C) , we should expect to observe a carbide phase. In the second case we could expect to observe at the end of the growth the presence of pure Fe catalyst NPs. A third case could be that the carbidic state is just intermediate state during the growth and at the end the catalyst NPs albeit showing metallic phase, during the growth was allowing a bulk diffusion of the carbon forming a Fe_3C carbide. As we have shown by ETEM characterization, this point has not being clarified because during the real-time measurements it was not possible to obtain high resolution images, which are needed because metallic fcc Ni(111), Ni_2O_3(200) and Ni_3C(113) have very close lattice spacing, in the range of 0.18-0.21 nm ± 0.01 nm (see also previous paragraph discussion). Our TEM characterizations done after growth have shown that the reacted Ni NPs are all compatible with a metallic phase. However, TEM data already present in literature have shown that after the growth the Ni reacted NPs can show both, metallic as well as carbide phases [39][40]. Therefore this point is still unclear, as for what happens during the growth as well as for the remaining phase at the end of the growth.

In case of low density growth, as previously reported (Figure 6.4), the carbide peak is present until the end of the growth and it could be partially due to the Fe NPs that did not nucleate any tubes. Moreover our photoemission data does not permit to know the distribution at the nanoscale of this carbide, in particular whether carbide is present in the more superficial part of the single clusters and/or from the bulk.

To refine our understanding about this point, we have analysed in details the C 1s photoemission peak acquired in situ after the growth of a dense SWNT film on Al_2O_3, in UHV environment, whose SEM image is shown in Figure 6.11(b). The sample have been grown by depositing 0.4nm of Fe on $Al_2O_3/SiO_2/Si$, then the CVD process have been done at 580°C, with a C_2H_2 pressure of $8x10^{-5}$mbar. The C 1s photoemission peak obtained just after growth is shown in Figure 6.11(a).

The presence of different components and the estimation of their binding energies have been realized by performing a non-linear mean square fit of the data in the energy range of the

C 1s. As before (see chapter 4, section 4.1.2), we used a Shirley background, and we reproduced the photoemission intensity by using, as fit function, three Doniach-Sunjic lineshapes. We kept null asymmetry for the peaks, except for the graphitc peak, for which we fixed the same asymmetry found on the temporal serial measurements (0.13). This asymmetry parameter is close to the one reported by Goldoni et al. for a bundle of SWNT (0.19)[41]. We fixed the Lorentzian line-width at 0.25eV for all peaks, in agreement with literature [41]. From our analysis, the C 1s signal [Figure 6.11(a)] exhibits a predominant graphitic carbon component at 284.5eV and two additional weak components, one at higher binding energy (285.7 eV), and another one at 283.2eV, which is compatible with the carbidic form of carbon, as we found for the previous temporal resolved carbon measurements.

We assigned the C 1s peak at 285.7 eV to the disordered graphitic carbon in agreement with Wiltner et al. [22], who measured by XPS HOPG (highly oriented pyrolytic graphite) after Ar^+ bombardment. They show how the amount of this disordered fraction can be modified by ion bombardment as well as by annealing. Ion bombardment leads to an increase in disordered C, but this fraction can be reordered again during annealing. Thermal treatment of deposited films on Au without irradiation leads to a shift of intensity from disordered to ordered graphitic C. This disordered carbon has been observed also by A.Goldoni et al. [41] in case of bundles of SWNT/MWCNT. We found the presence of the carbidic carbon (at 283.2 eV) after the growth only on the samples where also the Fe 2p photoemission signal was detectable. The latter one disappears when the covering of CNTs carpet has thickness higher than ~ 3 nm (which is three times the mean free path of electrons at the kinetic energy of the Fe). This is a confirmation that the carbide peak comes from carbon bound with Fe. We note that the C 1s binding energy reported in the literature for the Fe-C alloyed (FeC or Fe_3C) are within the range 283.2-283.6eV [20,22], but there are no well known binding energy data in the literature referred to these particular two alloys. Hence our XPS data, as they are, strongly suggests that SWNT growth is carried on by Fe alloyed with carbon .

We need to take into account that, as mentioned above, XPS doesn't allow an unambiguous distinction between surface carbide [carbon-rich (sub)surface layer] and bulk catalyst carbide and in addition we cannot distinguish between the particles reacted and unreacted. However in this case (Figure 6.11), because of the dense SWNTs growth, the amount of Fe no reacted is quite small, if compared to the sample grown in the SuperESCA experimental apparatus (Figure 6.4). This could permit us to support the hypothesis of the growth driven by Fe-C alloy.

To achieve a nanoscale characterization of our catalyst NPs, we are going to measure by HRTEM the sample with dense CNT growth on membranes covered by Al_2O_3 to measure the lattice parameter of the Fe NPs, and thus to determine which compound (or more than one) is present on the reacted NPs and on the no-reacted ones.

Our actual observation that the carbide peak exists since the tubes nucleation up to the end of the growth is in agreement with the recent observations by Nishimura et al. They measured by XRD at low incident angle measurements the Fe/SiO_2 sample and they reported that it remains crystalline during the continuous exothermic C_2H_2 dissociation and carbon network formation at 600-700 °C. They found that the carbon atoms are incorporated into the catalyst NPs to initially form oriented Fe-C and then a mixture of Fe-C and Fe_3C which then nucleate CNTs.

In conclusion, by investigating the Carbon 1s signal collected in situ at the end of several SWNT dense growths realized on Al_2O_3 we found out that carbidic carbon is always formed. We have planed to investigate by HRTEM the samples where carbide was visible by XPS to have a nano-micro correlation of our data. In the literature the presence or not of carbidic signal is a very controversial point, therefore the solution of this consists in a huge advancing in the knowledge of the mechanism of growth of CNT.

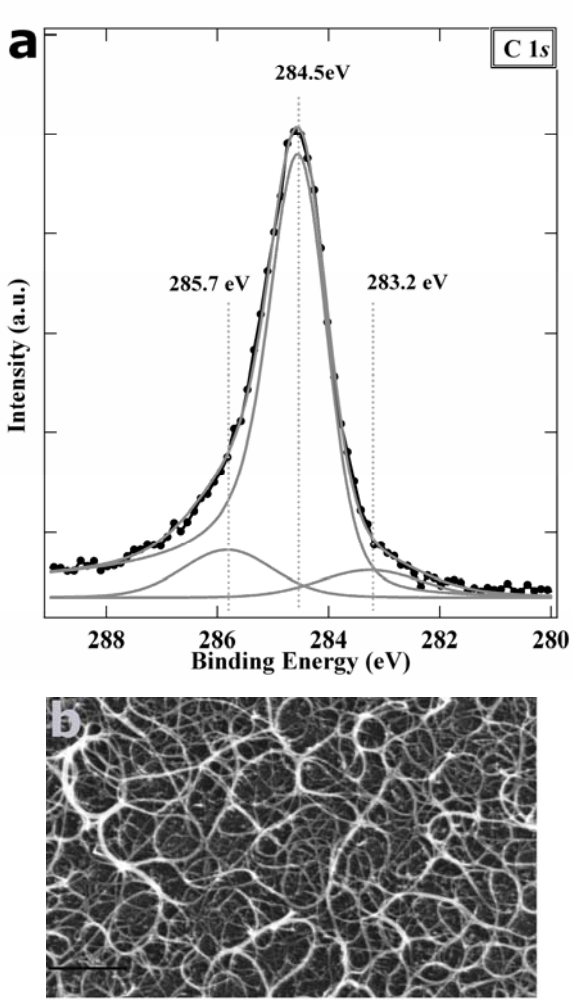

Figure 6.11 *(a) C1s photoemission spectrum (hυ=1253.6 eV) acquiredin situ at the end of SWNT bundles growth (b) , realized on Fe(0.4 nm)/Al_2O_3 by heating at 580°C for 5 min at the C_2H_2 pressure of (8x10^{-5} mbar). The fit of the spectrum is performed by a convolution of Gaussian and Lorentzian line shapes and subtracting a Shirley background; a indicatse the graphitic peak (284.5 eV)t, b indicates the disordered graphitic peak (285.7 eV), c indicates the carbidic peak (283.2 eV) . All spectra are normalized to the photon flux. (b) SEM image of the SWNT bundles, (scale bar: 200 nm).*

6.4 Conclusion

We have used *in situ* ETEM and *in situ* time-resolved XPS to reveal some of the catalyst dynamics that occur during surface-bound SWNT and CNF nucleation. The data have been acquired during the growth of low density SWNT/MWNT/CNFs on SiO_2 using C_2H_2 as precursor gas. Structural selectivity was determined by the dynamic interplay between carbon

network formation and catalyst particle deformation. Our *in situ* time-resolved XPS study shows the selective C_2H_2 chemisorption on the metallic Fe catalyst, which is rapidly followed by the formation of a carbon-rich phase (carbide), to finally the formation of a sp^2 carbon network. The carbidic carbon has been detected, even if gradually attenuated from the graphitic peak, up to the intensity saturation of the sp^2 C peak. Therefore, inside of the debate of the surface or bulk diffusion, our XPS data should indicate a continuously diffusion of C through the Fe NPs, forming, in this way an Fe- C alloy during the C_2H_2dosing which remains, as stable carbide, until the end of the growth.

Summarizing, we have observed selective C_2H_2 chemisorption at the nucleation stage and we demonstrated that the formation of a carbon-rich (sub)surface layer on crystalline transition metal NPs is an integral part of catalyst dynamics during CNT growth.

Bibliography

[1] Puretzky A. A., Schittenhelm H., Fan X. D., Lance M. J., Allard L. F., Geohegan D. B., *Phys. Rev. B* 65, 245425 (2002).

[2] Saito Y., *Carbon* 33, 979 (1995).

[3] Radushkevich L. V., Lukyanovich V. M., *Z. Fis. Chim. 26*, 88 (1952).

[4] Hata K., Futaba D. N., Mizuno K., Namai T., Yumura M., Iijima S., *Science 306*, 1362 (2004).

[5] Helveg S., Lopez-Cartes C., Sehested J., Hansen P. L., Clausen B. S., Rostrup-Nielsen J. R., Abild-Pedersen F., Norskov J. K., *Nature* 2004, *427*, 426.

[6] Lin M., Tan J. P. Y., Boothroyd C., Loh K. P., Tok E. S., FooY. L., *Nano Lett. 6*, 449 (2006).

[7] Fan S. S., Liu L., Liu M., *Nanotechnology 14*, 1118 (2003).

[8] Zhang Y., Li Y., Kim W., Wang D., Dai H., *Appl. Phys. A 74*, 325 (2002).

[9] Zhu H. W., Suenaga K., Hashimoto A., Urita K., Hata K., Iijima S., *Small 1*, 1180 (2005).

[10] Hofmann S., Csanyi G., Ferrari A. C., Payne M. C., Robertson J., *Phys. Rev. Lett. 95*, 36101 (2005).

[11] Cantoro M., Hofmann,S., Pisana S., Scardaci V., Parvez A., Ducati C., Ferrari A.C., Blackburn A. M., Wang K. Y., Robertson J., *Nano Lett. 6,* 1107 (2006).

[12] Mullins W. W., *J. Appl. Phys. 28*, 333 (1957).

[13] Anton R. *J. Mater. Res. 20*, 1837 (2005).

[14] Hansen P. L., Wagner J. B., Helveg S., Rostrup-Nielsen J. R.,Clausen B. S., Topsoe H., *Science 295*, 2053 (2002).

[15] Pisana S., Cantoro M., Parvez A., Hofmann S., Ferrari A. C., Robertson J., *Phys. E* 37, 1 (2006).

[16] Lolli G., Zhang L. A., Balzano L., Sakulchaicharoen N., Tan Y.Q., Resasco D. E., *J. Phys. Chem. B 110*, 2108 (2006).

[17] Hofmann S., Cantoro M., Kleinsorge B., Casiraghi C., Parvez A., Robertson J., Ducati C., *J. Appl. Phys. 98*, 034308 (2005).

[18] Malm J. O., O'Keefe M. A., *Ultramicroscopy 68*, 13 (1997).

[19]Panzner G., Egert B., *Surf. Sci*. 144, 651 (1984).

[20] Panzner G., DiekmannW., *Surf. Sci.160*, 253 (1985).

[21] Panaccione G., Fujii J., Vobornik I., Trimarchi G., Binggeli N., Goldoni A., Larciprete R., and Rossi G., *Phys. Rev. B* 73, 35431 (2006).

[22] Wiltner A., Linsmeier C. *Phys. Status Solidi A 201*, 881 (2004).

[23] Lascovich J. C., Giorgi R., Scaglione S., *Appl. Surf. Sci. 47*,17 (1991).

[24] Alstrup I., *J. Catal. 109*, 241 (1988).

[25] Nishimura K., Okazaki N., Pan L. J., Nakayama Y., *Jpn. J. Appl.Phys. 43*, L471 (2004).

[26] Ferrari A.C., and Robertson J., *Phil. Trans. R. Soc. London* A 362, 2477 (2004).

[27] Jorio A., Souza A. G., Dresselhaus G., Dresselhaus M. S., Swan A. K., Unlu M. S., Goldberg B. B., Pimenta M. A., Hafner J. H., Lieber C. M., and Saito R., *Phys. Rev. B* 65, 155412 (2002).

[28] Maultzsch J., Reich S., Schlecht U., and Thomsen C., *Phys. Rev. Lett*., 91, 87402 (2003).

[29] Telg H., Maultzsch J., Reich S., Hennrich F., and Thomsen C., *Phys. Rev. Lett*. 93, 177401 (2004).

[30] Lazzeri M., Piscanec S., Mauri F., Ferrari A. C., and Robertson J., *Phys. Rev. B*, 73 155426, (2006).

[31] Piscanec S., Lazzeri M., Robertson J., Ferrari A. C., and Mauri F., *Phys. Rev. B*, 75, 035427 (2007).

[32] Neubauer R., Whelan C. M., Denecke R., Steinruck H. P., *J. Chem.Phys.* 119, 1710 (2003).

[33] Jiang A., Awasthi N., Kolmogorov A. N., Setyawan W., Boerjesson A., Bolton K., Harutyunyan A. R., Curtarolo S., condmat/0612562 (2006).

[34] Niimi Y., Matsui T., Kambara H., Tagami K., Tsukada M., Fukuyama H., *Phys. Rev. B* 73, 85421 (2006).

[35] Hoffman S., private communication.

[36] Reich S., Li L., Robertson J., *Phys. Rev. B* 72, 165423 (2005).

[37] Gavillet J., Loiseau A., Journet C., Willaime F., Ducastelle F., Charlier J. C., *Phys. Rev. Lett.*, *8727*, 275504 (2001).

[38] Miyauchi Y. H., Chiashi S. H., Murakami Y., Hayashida Y., Maruyama S., *Chem. Phys. Lett.*, *387*, 198 (2004).

[39] Ducati C., Alexandrou I., Chhowalla M., Robertson J. and Amaratunga G. A. J., *J. Appl. Phys.* 95,6387 (2004).

[40] Lin M., Tan J.P.Y., Boothroyd C., Loh K. P., Tok E. S., Foo Y.L., *Nano Lett*. 7, 2234 (2007)

[41] Goldoni A., Larciprete R., Gregoratti L., Kaulich B., Kiskinova M., Zhang Y., Dai H., Sangaletti L., Parmigiani F., *Appl. Phys. Lett*. 80, 2165 (2002).

Conclusions

One major outcome of this thesis is the key role of the catalyst-substrate interaction on the growth of CNTs via CVD. We observed, in agreement with the literature, that, without any catalyst pretreatment, vertical CNT arrays ("forests") could be grown on Al_2O_3 support layers, whereas only low density of CNTs is obtainable by using the same growth conditions on SiO_2 support layer. We relate this different growth behavior to the different catalyst/substrate interaction, which influences deeply the catalyst nanoparticles mobility and size distribution.

X-ray photoemission data indicate that Fe interacts with the oxygen of the surface layer of Al_2O_3, whereas it does not form bonds with SiO_2. Consequently, the bonds between Fe and oxygen at the topmost layer of Al_2O_3 reduce the mobility of the Fe particles, preventing their coalescence into large islands upon annealing. As the vertically aligned growth depends on the size and mobility of the catalyst particle nucleating a tube, the narrower size distribution and the limited mobility of the particles lead to a more uniform growth rate of CNTs on Al_2O_3 than on SiO_2, hence allowing their vertically aligned growth.

In the second part of our work, we have used *in situ* ETEM and *in situ* time-resolved XPS to detect catalyst dynamics that occur during surface-bound SWNT and CNF nucleation. The data have been acquired during the growth of low density SWNT/MWNT/CNFs on SiO_2 using C_2H_2 as precursor gas. Structural selectivity was determined by the dynamic interplay between carbon network formation and catalyst particle deformation. Our *in situ* time-resolved XPS study shows the selective acetylene chemisorption on the metallic Fe catalyst, which is rapidly followed by the formation of a carbon-rich phase (carbide), which eventually takes to t the formation of a sp^2 carbon network. The carbidic carbon has been detected, even

if gradually attenuated from the graphitic peak, up to the intensity saturation of the sp^2 C peak.

Summarizing, we have observed selective acetylene chemisorption at the nucleation stage and we demonstrated that the formation of a carbon-rich (sub)surface layer on crystalline transition metal nanoparticles is an integral part of catalyst dynamics during CNT growth.

Future work

We have seen that the identification of the parameters which are crucial for a high level of control on nanotube growth could potentially lead to the diameter and chirality control of SWNT growth. This will have a boosting effect on the application-driven research of nanotubes as a new nanoscale building block.

In particular we observed that the low pressure ($8x10^{-6}$-$8x10^{-5}$ mbar) of the carbon precursor gases determines the growth of SWCNT only, irrespective of the catalyst diamater distribution. Whereas, the high pressure (atmosphere) can activate larger catalyst diameter, hence allowing the growth of a mix of MWCNT/SWCNT. Therefore more growth experiments by using different precursor gas pressures, different diameter distributions and subsequent HRTEM analysis will be devoted to understand this point. The selection of SWNT or MWNT only by changing the precursor pressure could be a easy and economic way to achieve well-defined CNTs .

It will also be crucial for the future studies to understand the role of iron carbide in the growth mechanisms involved in nanotube growth. Therefore more XPS experiments will be needed to clarify , whether the carbide is also an intermediate chemical phase before reaching the graphitic state or it is only related with the nanoparticles which did not work as seed for the CNT growth (called poisoned NPs).

As reported in the literature, CNTs can grown also from Au NPs, that is of interset of technology and also as model to study the growth mechanism. Actually what is more surprising about this point is that the phase diagram of Au/C does not predict any alloying. Therefore, we are planning experiments to grow CNTs by Au NPs with controlled diameter (< 5nm) on pre-patterned substrates and to perform XPS experiments to investigate the chemical state of the catalyst prior and during CNTs growth.

Appendix A

Experimental apparatus and procedures

Here we briefly describe the experimental apparatus and procedures used.for each experiment reported in this thesis.

A.1 Experimental Apparatus

A.1.1 Experimental chamber in Analytical Division at TASC Laboratory

The Analytical Division in TASC has an experimental apparatus operating in UHV(base pressure~ 10^{-10}-10^{-11}mbar, see Figure A.1)

The experimental apparatus consist of two chambers: one assigned to the sample surface preparation and the other one to its characterization. The characterization techniques are dedicated to the chemical composition and to the electronic and geometrical structure of the surface.

The surface preparation chamber is equipped with:

- PLASMA source
- Low Energy Electron Diffraction (LEED)
- Residual Gas Analyzer (RGA)
- Evaporators system
- leak valve for the gas introduction and flux meter
- ion gauge

The characterization chamber is equipped with:

- Hemispheric Analyzer of electrons (120 mm)
- X-Ray source ($h\nu$ = 1486.6 eV; $h\nu$ =1253.6 eV, ($\Delta E \approx 1.0$ eV)
- UltraViolet lamp ($h\nu$ = 21.2 eV; $h\nu$ = 40.8 eV,)
- Ion gun
- ion gauge

The configuration of the labloratory described above , permits to characterize the samples *in situ* by XPS/UPS/LEED immediately after the sample treatments. The pre-chamber is in UHV also and it is separated from the other two chambers by UHV valves. The pre- chamber is equipped with ¼" stainless-steel pipes to introduce C_2H_2 (grade 3, SIAD). The configuration of the labloratory described above, permits to characterize the samples directly *in situ* by XPS/UPS/LEED immediately after the treatments underwent.

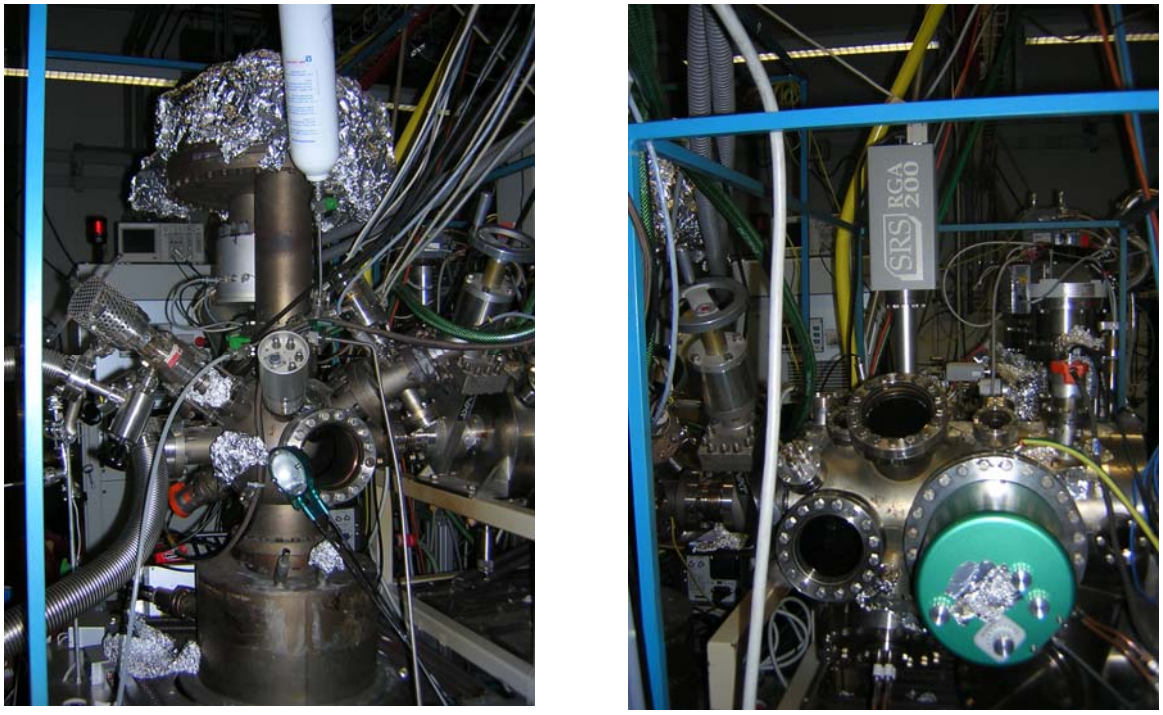

Figure A.1 *Frontal view of the characterization (left image) and preparation chambers (rightt image) at the Analytical Division in TASC .*

A.1.2 Experimental chamber at "Microstrutture e nanostrutture di Carbonio" laboratory at Elettra

This system is very similar the UHV apparatus in TASC (described above).
Also in this case the apparatus operates in UHV(~ 10^{-10}-10^{-11}mbar) and consists of two chambers: one assigned to the sample surface preparation and the other one to the characterization techniques . The characterization techniques are dedicated to the chemical composition and to the electronic structure of the surface.
The chamber dedicated to the surface preparation is equipet with:

- PLASMA source
- Low Energy Electron Diffraction (LEED)
- evaporator system
- ion gauge
-leak valve for the gas introduction

The chamber dedicated to the chemical characterization is equipet with :

- emispheric Analyzer of electrons (120 mm)
- X-Ray source (hν = 1486.6 eV; hν =1253.6 eV, (ΔE ≈ 1.0 eV
- UVlamp (hν = 21.2 eV; hν = 40.8 eV,)
- Ion gun
- Residual Gas Analyzer (RGA)
- ion gauge

This apparatus has another small chamber in between the preparation chamber and the characterization chamber which is called pre chamber where two ¼" stainless-steel pipes are located to introduce : C_2H_2 (grade 3, SIAD) , and O_2 (grade 4, Siad). Moreover it is also equipped with ion gauge.

The pre-chamber is in UHV also and it is separated from the other two chambers by UHV valves. The configuration of the labloratory described above , permit to characterize the samples directly *in situ* by XPS/UPS/LEED immediately after the treatments underwent.
This apparatus system, with respect to the TASC one above described, has a fast entry for the samples. This consist a huge advantage permitting to introduce more than one sample a day.

In fact in the TASC system it is necessary, to work in UHV condition, to perform a bake out of the manipulator any time we want to substitute the sample.

A.2 Experimental procedures

A.2.1 UHV chamber

Fe deposition on SiO_2 and Al_2O_3 and CNT growth via CVD

To study the Fe-substrate interaction (Al_2O_3 and SiO_2),we realized all the step of the CVD process *in situ*, from the loading up of the sample up to the XPS characterization after the growth.

The samples preparation steps were:

1. Sample loading.
2. Outgassing of the sample at ~580°C (up to reach the pressure of $2x10^{-10}$ mbar, and until we didn't observe any contaminant from the substrate).
3. XPS measurements of the substrate signals (O1s, Si2p, Al2p core levels, Al2p when it was present).
4. Fe deposition at room temperature in UHV.
5. XPS measurements of the substrate signals (O1s, Si2p, Al2p core levels, Al2p when it was present) and the Fe 2p signal.
6. Annealing of the sample at the growth temperature in UHV.
7. XPS analysis of the substrate signals (O1s, Si2p, Al2p core levels, Al2p when it was present) and the Fe 2p signal.
8. Dosing of the C_2H_2 with the sample heat up at the growth temperature
9. XPS analysis of the substrate signals (O1s, Si2p, Al2p core levels, Al2p when it was present), the Fe 2p signal and the C1s signal.
10. Loading out of the sample for the ex situ characterization.

To stop the outgassing of the sample,at the beginning of each Fe evaporation, and after and before every dosing of C_2H_2, we check the gasses in the chamber by using the RGA, to be sure that no contaminants were present.

The substrates, used for all the experiments, were commercial 0.01-0.02 Ωcm boron-doped Si(100) wafers as substrates, covered with thermally grown SiO_2 (200 nm). The SiO_2 layer

can prevent uncontrolled silicide formation. For the growth on Al_2O_3 (10nm)/SiO_2 (200 nm)/Si , the additional covering of $Al_2O_3$was performed by sputtering from Al_2O_3 target .

The Fe films were deposited *in-situ* at room temperature (RT) by sublimation induced by electron bombardment from heated filaments (Aldrich, 99.9% purity) at a growth rate of ~0.1 nm/h (calibrated by XPS), the evaporation pressure was ~ 5x 10^{-9} mar and the power ~ 30 mwatt.

Samples are clamped between two Ta contacts and heated by direct heating (the electron current was passing through the Si wafer) in the experimental chamber at Analytical Division in TASC and the temperature was monitored by using an optical pyrometer, whose emissivity was kept at 0.64 for all the samples (as it is reported in the literature for SiO_2).

Whereas the samples were heated up by indirect heating in the experimental chamber at "Microstrutture a nanostrutture di Carbonio" laboratory in Elettra. Also here the temperature was monitored by using an optical pyrometer, whose emissivity was kept at 0.64 (as it is reported in the literature for SiO_2).

The H_2 (grade 4, SIAD) sputtering has been performed by using Sputter gun operating at 600 eV and raster scanning the surface of the sample . We grown CNTs by using undiluted C_2H_2 (grade 3 SIAD) introduced in the preparation chamber in two different way depending on the used system.

In the experimental chamber at Analytical Division in TASC the C_2H_2 was let in through a ¼" stainless-steel pipe, whose nozzle is 1 cm away from the sample and we used flux meter at 10 sccm and C_2H_2 pressure ~8x10^{-4} mbar. While in the experimental chamber at "carbon nano and micro structure" laboratory in Elettra, we let in the C_2H_2 by opening the UHV valve, that was separating the growth chamber from a prechamber which was previously filled with C_2H_2 at a pressure slightly higher than the growth one.

A.2.2 Low vacuum chamber/ fournace (University of Cambridge, Department of Engineering)

Fe deposition on SiO_2 and Al_2O_3

The substrate used were polished, 0.01-0.02 Ωcm boron-doped Si(100) wafers as substrates, covered with thermally grown SiO_2 (200 nm). The SiO_2 layer can prevent

uncontrolled silicide formation. For the growths on Al_2O_3 (10nm)/SiO_2(200 nm)/Si , the additional covering of Al_2O_3 was performed by sputtering from Al_2O_3 target .

High-purity Fe catalyst films was deposited by thermal evaporation. The evaporation rate is <1 Å/s at $<10^{-6}$ mbar base pressure. No substrate heating is used during evaporation. The film thickness is monitored *in situ* by a quartz crystal microbalance and calibrated ex situ by atomic force microscopy (AFM, Digital Instruments Nanoscope III and Veeco Explorer) and spectroscopic ellipsometry (J. A. Woollam Co., M-2000 V).

Low vacuum chamber: Pretreatments and CNT growth via CVD

The substrates are transferred in air and loaded onto a resistively heated graphite stage (Figure A.2). The stainless steel CVD chamber is diffusion pumped (base pressure $<10^{-6}$ mbar) with massflow-controlled gas feeds. The temperature is continuously monitored by three shielded thermocouples distributed across reference Si substrates (500 μm in thickness, equivalent to samples) and the graphite heater, Figure A.2.

All temperatures indicated refer to the substrate surface temperature measured on top of the Si and not to the heater block (which has higher T for a typical poor thermal contact) and thus truly represent the catalyst temperature. It is known from general heterogeneous catalysis that significant temperature differences between an individual catalyst particle and its support will not exist under realistic conditions of rate and size. This holds for exothermic feed-gas dissociation as well as plasma heating.

The catalyst film is heated in NH_3 (grade 5, 0.6-20 mbar) or H_2 (VLSI grade, 0.6-100 mbar) for typically 15 min to equilibrate the desired growth temperature. The chamber is then evacuated and undiluted C_2H_2 (AA grade, 99.6% purity) is allowed to flow from a side gas inlet at 10^{-3}-10^{-2} mbar. After a growth period of 5 min, the samples are cooled in vacuum.

Fournace : Pretreatments and CNT growth via CVD

Prior to growth in the furnace the catalyst film was annealed at 750°C in 200:500 sccm Ar:H_2 at atmospheric pressure for 3 min. CNTs were grown at the same temperature in 200:500:10 sccm Ar:H_2:C_2H_2 for 20 min from Fe fillms (0.7 - 1.1 nm). Using the direct-heating method, the catalyst-coated substrate (15 *x* 5 mm^2) was resistive-heated to the growth temperature within a few seconds by a current (3A) fowing through the sample. The heating

was directly performed in the growth atmosphere without pretreatment. The temperature was measured with a pyrometer.

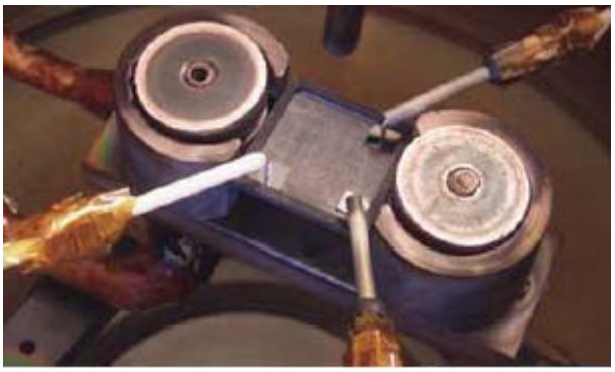

Figure A.2 *Graphite heater stage with shielded thermocouples.*

A.3 Ex situ characterizations

The other facilities used for the *ex situ* characterizations which are present in TASC laboratory are: Atomic Force Microscopy (AFM Veeco-Thermicroscope Autoprobe CP Research), Scanning Emission Microscopy (SEM, Zaiss,supra40), and Raman spectroscopy (Renishaw 1000 Raman spectrometer, 514.5 nm excitation). The other facilities used for the ex situ characterizations which are present in the Department of Engineering, University of Cambridge, are scanning electron microscopy (SEM, LEO 1530VP FEGSEM), AFM, Digital Instruments Nanoscope III and Veeco Explorer and Raman spectroscopy (Renishaw 1000 Raman spectrometer, 514.5, 633, and 785 nm excitation).

For HRTEM high-resolution (HR) TEM (JEOL JEM 4000EX, 400 kV; FEI Tecnai F20, 200 kV located at Department of Materials Science and Metallurgy, University of Cambridge).Analysis, we used thin catalyst films (99.9% purity) thermally evaporated (base pressure 10^{-6} mbar) onto perforated SiO_2 membranes (SPI supplies) or onto 2000 mesh Cu TEM grids (Agar Scientific) coated with SiO_2 nanopowder (Degussa Aerosil Ox50) and a ~ 30 nm sputtered SiO_2 layer. For some of these membranes it has been sputtered over ~ 10 nm of Al_2O_3 starting from Al_2O_3 target .

A.4 Experimental equipment dedicated to the study of Fe/ HOPG system (Dipartimento di Fisica, Università Cattolica, Brescia)

The sample preparation and characterization experiments were performed using an OMICRON STM/SEM/SAM UHV system with a base pressure $<5 \times 10^{-11}$ mbar and consisting of two (sample preparation and analysis) UHV chambers, connected each other through a sample transport system. The sample preparation chamber is equipped with e-beam evapourators and Ar^+ ion sputtering system, while the analysis chamber consists of STM/SEM/SAM system. The HOPG specimen (ZYA grade, 3×5 mm^2) has been mounted on the sample holder using Ta foil clamps employed also as electrical contacts to anneal HOPG specimens by direct current heating. The temperature of the sample has been measured by an optical pyrometer (Raytek, RayMa2S/CCF). Fe deposition on HOPG basal plane has been performed in the sample preparation chamber using a high voltage e-beam sublimator, consisting of Fe rods (purity 99.99% from Goodfellow) as target and a tungsten filament as the e-beam source. The STM tips were prepared by chemical etching of a tungsten wire in a NaOH solution, and subsequently cleaned by electron bombardment in the UHV chamber. The STM images have been obtained in constant current mode at RT.

A.5 Experimental equipment dedicated to the study in real time of the CNT growth

A.5.1 ETEM (Center for Solid State Science, Arizona State University)

For ETEM characterizations in real time we used a modified Tecnai F20 ETEM, operated at 200 kV, equipped with a differential pumping system and a Gatan imaging filter [1]. The microscope permits pressures of up to10 mbar, with a specified information limit of 0.14 nm. Video sequences can be recorded with 30 frames/s time resolution. The electron dose was representative of that typically implemented for high-resolution imaging,[2] and the electron beam was never focused onto the specimen in order to minimize the effects of

electron-beam-induced damage and modification of the specimen. Thin catalyst films (99.9% purity) were thermally evaporated (base pressure ~ 10^{-6}mbar) onto perforated SiO*x* membranes (SPI supplies) or onto 2000 mesh Cu TEM grids (Agar Scientific) coated with SiO*x* nanopowder (Degussa Aerosil Ox50) and a ~ 30 nm sputtered SiO*x* layer. The samples were transferred in air to the ETEM.

A.5.2 Superesca beamline at Elettra Syncrothron

In situ time-resolved XPS was carried out in UHV end-station of the SuperESCA beamline (base pressure <1 x10^{-10} mbar) at the Elettra Synchrotron. We stress that in-situ, *fast* time-resolved XPS measurements can only be carried out using a high-brilliance photon source, such as a synchrotron light beam. The probe size was 30 μm - 200 μm. For all the experiments, we utilize commercial, polished n-type Si(100) substrates, topped with a 150 nm thermally grown SiO_2 film. Fe and Ni catalyst films are deposited in-situ by sublimation from heated filaments (Aldrich, 99.9% purity) at a growth rate of ~0.6 nm/h (calibrated by XPS). Samples are clamped between two Ta contacts and heated by direct heating .Here we followed exactly the experimental procedure reported in A.2. The core levels of Fe 3s, Ni 3s, Si 2p, O1s, we acquired with high resolution conditions. Moreover here a high flux of 100-400 eV photons allowed core-level spectra to be acquired within ~15 s with an energy resolution below 80 meV during the growth. For CNT growth, undiluted C_2H_2 (grade3, SIAD) is let into the SuperESCA chamber using a gas-doser with a micro-channel plate head, 15 mm away from the sample. The H_2 (grade 4, SIAD) sputtering has been performed by using Sputter gun operating at 600 eV and raster scanning the surface of the sample. This setup allows direct measurements in gas background pressures up to 10^{-6} mbar.

Bibliography

[1] Sharma, R. *J. Mater. Res. 20*, 1695 (2005).

[2] Yokota, T.; Murayama, M.; Howe, J. M. *Phys. Rev. Lett. 91*,265504 (2003).

The data of the present thesis have been partially published in the following journals or are in preparation:

[1] **"The influence of the substrate-catalyst interaction on the carbon nanotube growth: Chemical and morphological studies"**
C. Mattevi, C. T. Wirth, S. Hofmann, J. Robertson, M. Cantoro, C. Cepek, C. Castellarin-Cudia, A. Goldoni *in preparation*

[2] **"Surface-bound chemical vapour deposition of carbon nanotubes: in-situ study of catalyst activation"**
C. Mattevi, S. Hofmann, M. Cantoro, A. C. Ferrari, J. Robertson, C. Castellarin-Cudia,S. Dolafi, A. Goldoni, and C. Cepek , *Physica E*, in press

[3] **"In situ Observations of Catalyst Dynamics during Surface-Bound Carbon Nanotube Nucleation"**
S. Hofmann, R. Sharma, C. Ducati, G. Du, C. Mattevi, C. Cepek, M. Cantoro, S. Pisana, A. Parvez, F. Cervantes-Sodi, A. C. Ferrari, R. Dunin-Borkowski, S. Lizzit, L. Petaccia, A. Goldoni, and J. Robertson, *Nano Lett*. 7 (2007), p. 602

[4] **"Effect of substrate surface defects on the morphology of Fe film deposited on graphite"**
I.N.Kholmanov,L.Gavioli,M.Fanetti,M.Casella,C.Cepek,C.Mattevi,M.Sancrotti, Surface Science,601 (2006),188